

# Kinematic dynamo onset and magnetic field saturation in rotating spherical Couette and periodic box simulations

Dissertation

zur Erlangung des mathematisch-naturwissenschaftlichen Doktorgrades

“Doctor rerum naturalium”

der Georg-August-Universität Göttingen

-

im Promotionsprogramm ProPhys

der Georg-August University School of Science (GAUSS)

vorgelegt von  
Konstantin Finke  
aus Delmenhorst  
Göttingen, 2013

### Betreuungsausschuss

Prof. Dr. Andreas Tilgner, Institut für Geophysik, Fakultät für Physik

Prof. Dr. Ulrich Christensen, Max Planck Institute for Solar System Research

### Mitglieder der Prüfungskommission

Referent: Prof. Dr. Andreas Tilgner, Institut für Geophysik, Fakultät für Physik

Korreferent: Prof. Dr. Ulrich Christensen, Max Planck Institute for Solar System Research

Weitere Mitglieder der Prüfungskommission:

Prof. Dr. Ansgar Reiners, Institut für Astrophysik, Fakultät für Physik

Prof. Dr. Hardi Peter, Max Planck Institute for Solar System Research

Prof. Dr. Martin Rein, Institut für Strömungsmechanik, DLR

Prof. Dr. Wolfgang Glatzel, Institut für Astrophysik, Fakultät für Physik

Tag der mündlichen Prüfung: 19.06.2013

# Contents

<b>1</b>	<b>Introduction</b>	<b>5</b>
<b>2</b>	<b>Kinematic dynamo onset of spherical Couette flows</b>	<b>11</b>
2.1	Dynamo model . . . . .	14
2.1.1	Differential equation . . . . .	14
2.1.2	Numerical realisation . . . . .	20
2.2	Smooth surface . . . . .	23
2.2.1	Hydrodynamic properties . . . . .	24
2.2.2	Kinematic dynamo threshold . . . . .	30
2.2.3	Stationary regime . . . . .	32
2.2.4	Dynamo mechanism in the turbulent regime . . . . .	39
2.3	Rough surface . . . . .	46
2.3.1	Hydrodynamic properties . . . . .	47
2.3.2	Kinematic dynamo threshold . . . . .	52
2.4	Conclusion . . . . .	58
<b>3</b>	<b>Magnetic field saturation in a rotating G. O. Roberts like driven flow</b>	<b>61</b>
3.1	Weakly non-linear theory . . . . .	65
3.2	Results of the numerical model . . . . .	75
3.2.1	Non-linear Navier-Stokes equation . . . . .	75
3.2.2	Linearised Navier-Stokes equation . . . . .	87
3.2.3	Outlook . . . . .	91
3.3	Conclusion . . . . .	96
	<b>Bibliography</b>	<b>99</b>
<b>A</b>	<b>List of Figures</b>	<b>105</b>



# **1 Introduction**

Magnetic fields are ubiquitous in the universe and can be found in celestial bodies, galaxies, stars including our Sun and planets like the Earth or Jupiter. Due to the fact that at least in the Earth's interior, temperatures are well above the Curie temperature, its magnetic field cannot result from permanent magnetisation. Moreover, its time dependence gives rise to the assumption, that the generation of the magnetic field must be the result of a very complex dynamical process (Moffatt and Proctor 1982). This is supported by the fact that the diffusive time scale of most of the generated magnetic fields is much shorter than the life time of the respective objects. Today, it is generally accepted that the magnetohydrodynamic (MHD) dynamo effect is responsible for the magnetic field generation in most stellar objects (Weiss 2002). The idea is that the magnetic fields can be sustained by self-inductive processes of a moving electrically conducting fluid or plasma.

Most of the plasma flows are convection-driven by temperature gradients in rotating objects. Busse (1975) developed a model of the geodynamo as a convection-driven fast rotating spherical system. According to the conditions deduced from the Taylor-Proudman theorem and based on the Rayleigh-Bénard convection (Greenspan 1968, Chandrasekhar 1961), the flow forms vortex tubes aligned with the axis of rotation, in so-called Busse columns (Busse 1975). This type of helical velocity field is assumed to be predominant in many convection-driven rotating bodies.

It has been known for a long time that the Earth has a dominant magnetic dipole field (Merrill et al. 1996). Since the 1950s it is also known that the Sun has a detectable dipole field, although it is much weaker than the magnetic field of the quiet Sun. In fact, most of the celestial objects have detectable magnetic fields that are sustained on large spatial scales, which stands in contrast to the small scale of the energy carrying-vortices of the underlying flow. One possibility to deal with this scale separation is the mean field approach (Steenbeck et al. 1966, Krause and Rädler 1980), in which large-scale magnetic fields are generated by the averaged induction result of small-scale velocity and magnetic field perturbations. This effect is known as the  $\alpha$ -effect (Moffatt 1978). Especially with regard to the Sun, another effect is crucial for the magnetic field generation. As a result of the differential rotation within the Sun, the plasma flow exhibits large shear, where magnetic energy is gained by magnetic field line stretching. This is called the  $\Omega$ -effect; therefore, the dynamo of the Sun is known as an  $\alpha - \Omega$  dynamo (Moffatt 1978).

The first numerical attempts to investigate the dynamo effect were carried out by Gilman and Miller (1981) and Glatzmaier (1984), who modeled the solar dynamo. Based on this pioneering work, computer simulations became increasingly important for the investigation of planetary or Sun-like objects. As computer power and resolution advanced, two types of direct numerical simulations were developed. On one hand, convection-driven dynamo simulations in rotating spherical shells have been established, which intend to simulate planet or star like objects. Here, the implementation of gravitational, buoyancy and Coriolis forces

usually causes the generation of Busse-column like flow structures. These models were able to reproduce the main features of the geodynamo (Glatzmaier and Roberts 1995, Christensen et al. 1999) and dynamos of other planets and stellar dynamos (Christensen et al. 2009) but are not adaptive to, e.g., galactic dynamos.

Galactic objects are of an enormous extent and thus, have a scale separation from the large-scale magnetic field down to the smallest diffusive scales that cannot be resolved. Therefore, on the other hand, corresponding models were performed in periodic boxes where each one only represents a small part of the whole object. The focus is on the dynamo generation at the smallest turbulent scales. In these simulations, the flow is usually driven by helical volume forces that inject energy into large scales of the velocity field. Due to inertial processes, the kinetic energy is distributed over a large range of spatial scales down to the smallest diffusive ones. Attempts have been made to understand to what extent flows, evolving turbulence, are able to sustain a dynamo (Schekochihin et al. 2004b, Brandenburg and Subramanian 2005). Even though such turbulent helical flows have been able to generate large-scale magnetic fields (Brandenburg 2009, Ponty and Plunian 2011, Graham et al. 2012), a fundamental understanding of the underlying processes is still lacking.

In the advent of this research field, three types of simply-shaped helical velocity fields and their capability to dynamo action has been investigated. The Ponomarenko dynamo, the G. O. Roberts dynamo and the Dudley-James dynamo. The Ponomarenko dynamo is a single vortex tube, embedded in an isolating environment. Additional to the circular motion, the velocity field has a component parallel to the vorticity field such that the flow exhibits helicity (Ponomarenko 1973). The G.O. Roberts dynamo consists of a periodic array of vortex tubes with an alternating up and down streaming flow. The sense of rotation is so that the helicity does not change sign (Roberts 1972). The third type of flows has a spherical geometry and has been investigated by (Dudley and James 1989), e.g. the s2t1-flow<sup>1</sup>. This flow creates helicity with opposite sign in each hemisphere. All of these flows are basically able to sustain a dynamo, whereas the helical character of the flow is a crucial property.

Aforementioned basic flows have been taken as prototypes for experimental setups in order to generate a dynamo in the lab. Based on the Ponomarenko dynamo and the G.O. Roberts flow, two experiments have already been successful in generating a dynamo: the Riga (Gailitis et al. 2000) and the Karlsruhe experiment (Muller and Stieglitz 2002), which were named after the cities where they were built. In these experiments, liquid sodium was taken as working fluid. It is of high conductivity, melts at comparably low temperatures ( $\sim 110$  °C) and has a similar viscosity as water. It was pumped through

---

<sup>1</sup>In radial direction it is quadrupolar (s2) and in azimuthal direction the velocity does not change the sign over latitude (t1).

cylindrical pipes and thereby forced into helical shape. The Riga experiment used only one pipe and the Karlsruhe experiment a lattice of pipes with alternating up- and down-flows.

After the success of the first dynamo experiments to create a dynamo, a follow-up generation of experiments based on the Dudley-James dynamos has been designed in spherical geometry, which were built in Madison (Nornberg et al. 2006), Grenoble (Nataf et al. 2008) and Maryland (Rieutord et al. 2012). Another experiment was designed in cylindrical geometry (Monchaux et al. 2007) and is located in Carderache. The latter one generates a Van-Karman like flow and is therefore called the VKS experiment. In these experiments the flows are less constrained than in the previous ones in Karlsruhe or Riga. The liquid sodium was driven by rotating impellers or spheres which generate a large-scale mean flow of the same topology as those of Dudley and James (1989). Due to a strong impellent which is necessary to create the conditions for dynamo generation, the fluid becomes highly turbulent. The dynamo efficiency of the flow thereby decreases in such a way that so far, no experiment succeeded in creating a dynamo until today with the exception of the VKS experiment. In that case, the use of soft iron impellers significantly changes the magnetic boundary properties (Berhanu et al. 2010). The insights that have been gained in relation to MHD turbulence and small-scale dynamo theory are helpful for the understanding. Because of the driving, small-scale structures can evolve and create a competing or disturbing effect to the large-scale dynamo generation of the mean flow.

The performance of experiments is somewhat complex and provide insight which are limited by the measurement techniques. Flow structures are made visible using dye in water experiments or by pulsed Doppler velocimetry. Most importantly, magnetic fields can only be measured at the surface. In order to achieve a better understanding of these complex processes and their interrelations, numerical codes have been designed for in-situ analysis, which is not possible by surface measurements. The experimental results, in turn, are the only way to confirm these numerical models. However, the computational abilities are not sufficient to resolve the fields in the parameter range of the real objects they are adapted to. The transfer of respective results to real objects is only possible by exponential powerlaws Christensen and Aubert (2006), Christensen et al. (2009).

Computationally based work has been performed related to the Karlsruhe dynamo. Tilgner (1997) could predict the onset of magnetic field amplification and the saturation level of the field by numerical simulations. This dynamo experiment, however, uses a constrained flow, where turbulence plays a minor role. Thus, the simulation could be performed in the laminar regime, which, in contrast to turbulence simulations, is not computationally demanding. Close to the dynamo onset the Lorentz force is small compared to other forces so that it can be treated as a weakly non-linear effect in the mean field picture and solved analytically up to the first perturbation order (Tilgner and Busse 2001).

Bayliss et al. (2007) and Reuter et al. (2009, 2011) studied the dynamo mechanisms in flows related to the Madison experiment based on laminar wave-like motion and in highly turbulent flows. The parameter for the onset of magnetic field amplification could be determined, which was shown to be independent of the degree of turbulence. Since the accessible parameter regime of the simulations is far to low, the results had to be extrapolated to those parameters relevant for the experiment. Although the mean flow should be able to sustain a dynamo, it is still unclear why the flow in the experiment is that inefficient. With respect to the VKS experiment, the dynamo threshold has also been investigated and magnetic field topologies of existing dynamos could be reproduced by Giesecke et al. (2010a) and Pinter et al. (2010). Especially the effect of soft-iron impellers on the dynamo efficiency was reproduced by numerical simulations (Giesecke et al. 2010b). In order to reach higher magnetic Reynolds numbers, another experiment in spherical geometry was built in Maryland (Zimmerman 2010), which is larger and more powerful than previous experiments. It has a diameter of 3 meters and stronger motors in order to create higher rotation rates, which are necessary for dynamo action. Even though the topology of the mean flow of spherical Couette experiments <sup>2</sup> is similar in the experiments in Carderache and Madison, the respective numerical analysis of Guervilly and Cardin (2010) showed that the dynamo onset is increasing with the rotation rate of the inner sphere, contrary to the respective numerical analysis of the other experiments. For the spherical Couette flow, this means that an increasing degree of turbulence lowers the dynamo efficiency. According to the results of Guervilly and Cardin (2010), this experiment will fail to create a dynamo as well. Therefore, it is worth investigating how this experiment needs to be modified in order to get a flow that is more efficient to generate a dynamo.

This PhD thesis consists of two parts which treat two fundamental aspects in dynamo theory. The first part focuses on the kinematic dynamo threshold of the spherical Couette flow. Since previous work on this system failed to come up with promising results for spherical Couette experiments to succeed in creating a dynamo, the simulations are going to be repeated in order to compare the results with a different driving mechanism. The spherical Couette system is driven by the moving boundaries (in this case, only the inner sphere is rotating), which are coupled to the fluid by viscous drag. Compared to the Maryland experiment this is represented by smooth boundaries. Since the boundary layer is dependent on the rotation of the inner sphere, the efficiency of the flow could be increased by a driving force that drives the flow in a constant distance from the inner boundary so that it becomes independent from the rotation rate and increases the mo-

---

<sup>2</sup>The spherical Couette is a system of two concentric spheres with two different radii. The spherical gap is filled with a viscous (electrically conducting) fluid. In this context the spherical Couette flow is generated by a single rotation of the inner sphere, whereas the outer sphere is stationary.

momentum transfer. Accordingly, the Maryland experiment can be modified by rough inner boundaries or blades attached to the inner sphere. In this part the characteristics of both flows and their efficiency to dynamo action is compared. Thereby the mechanism of the dynamo plays a crucial role and on which scales the magnetic field is generated. The results are partly published in Finke and Tilgner (2012).

The second part deals with the saturation mechanism of a magnetic field in a rotating system. The relation of rotation, convection and magnetic field has been investigated by Mangeney and Praderie (1984), Noyes et al. (1984), Pizzolato et al. (2003) for main sequence stars. Especially Reiners et al. (2009) found that in slow rotating low-mass stars (M-type dwarfs) the surface magnetic field increases with the rotation rate of the respective object. In fast rotating M-stars, however, the surface magnetic field becomes rotationally independent at a certain rotation rate. The dependence of the magnetic energy's saturation level on the rotation rate has been investigated in several numerical models (Christensen and Aubert 2006, Schrunner et al. 2012, Tilgner 2012). Neither the exponent for the increase of the magnetic field with the rotation rate nor the saturation mechanism could be consistently reproduced. Therefore, the saturation of the magnetic field within a G. O. Roberts like driven flow in a rotating frame of reference is investigated, since the flow structure in such celestial bodies is believed to have a similar shape. Once a small magnetic field rises within a flow, at a certain point its Lorentz force reaches a strength comparable to the driving force and reorganises the flow, so that the magnetic field saturates.

This part focuses on the effect of the rotation rate on the saturation mechanism of the dynamo and the reorganisation of the velocity field by the Lorentz force. As long as the parameters are close to the kinematic dynamo onset, the Lorentz force is small and can be treated as a weakly non-linear perturbation in the mean field picture. The approximated MHD equations are solved analytically in a rotating periodic box, where the flow is driven by a force field corresponding to the G.O. Roberts flow similar to Tilgner and Busse (2001). In order to test whether these analytical assumptions are reliable, numerical simulations of the full MHD equation are performed.

Since the mean flows of many rotating celestial objects are assumed to have the similar basic properties as the G.O. Roberts flow and their magnetic fields are usually generated on large scales, it is a promising approach to achieve basic understanding from such a simple and analytically treatable model.

## **2 Kinematic dynamo onset of spherical Couette flows**

The spherical Couette consists of two concentric spheres of radii  $r_i$  of the inner and  $r_o$  of the outer sphere with an aspect ratio of  $\eta = r_i/r_o = 1/3$ , which is shown in Figure 2.1. The gap between the spheres is filled with a fluid, which is driven by the rotation of the inner sphere at a fixed rotation rate, while the outer boundary is stationary. Due to the viscous coupling of the fluid and the spheres, a shear layer develops at the inner boundary, in which the fluid is accelerated and centrifuged outward in an equatorial jet and finally recirculates within the entire rest of the volume to the inner sphere. The axisymmetric streamlines of the flow are shown in a meridional cut in Figure 2.1 on the left side. The velocity field in direction of the rotation is indicated in a contour plot on the right hand side. The highest values are near the inner sphere.

The general geometry of the mean flow is quadrupolar due to the meridional circulation with opposite helicity in each hemisphere. It is topological similar to the s2t1-flow, which has already been investigated by Dudley and James (1989) and is basically able to create a dynamo. This kind of flow is called the non-rotating spherical Couette flow. Considering an electrically conducting fluid, the focus of this work is on how a magnetic seed field evolves therein and how the onset of magnetic field amplification changes with respect to the rotation rate. The dynamo onset is denoted by the critical magnetic Reynolds number  $Rm_c$ , which thereby serves as a measure for the dynamo quality. These questions are closely linked to the dynamo mechanism of the flow.

The spherical Couette flow in this sense has already been deeply investigated with respect to purely hydrodynamic aspects by Hollerbach et al. (2006) and magnetohydrodynamic

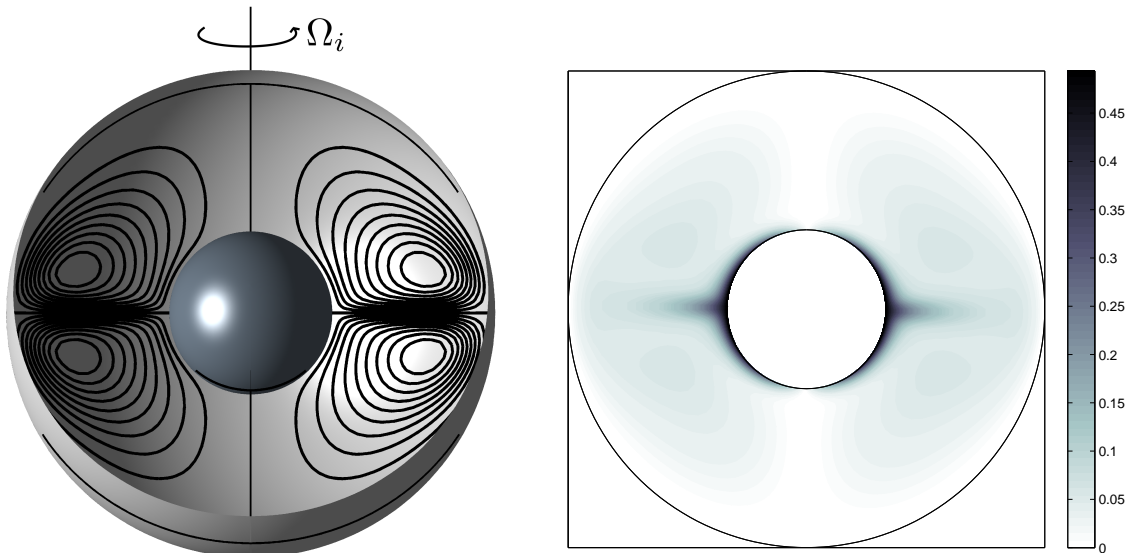


Figure 2.1: Scheme of the spherical Couette system with streamlines of the axisymmetric poloidal flow (left) and a contour plot of the axisymmetric toroidal flow (right) in a meridional cut.

aspects by Hollerbach (2009) and with the focus on dynamo action by Guervilly and Cardin (2010). The latter one is related with the generation of a dynamo in the spherical Couette experiment in Grenoble (Nataf et al. 2008). The results of Guervilly and Cardin (2010) are, however, discouraging, since the onset shows an increasing  $Rm_c$  with higher rotation rates of the inner core. The magnetic Prandtl number  $Pm$  remains of order one in the entire parameter range of the Reynolds number  $Re$ , so that the conditions in the experiment can not be reached by extrapolation. The aspect ratio is slightly different and the conductivity of the boundaries are the same as of the fluid. With respect to these results no dynamo can occur in this experimental setup.

Keeping this problem in mind, the spherical Couette is simulated again in order to confirm the results. These results are compared with properties of another Couette flow, which is driven by a volume force in one tenth of the gap width at the inner core and intends to simulate the spherical Couette flow with a rough inner sphere. It is assumed that the boundary layer and the equatorial jet are crucial to dynamo action due to shears in the velocity field.

In the first simulations, in which rigid walls are used to drive the fluid at the inner core, the boundary layer thickness decreases with increasing  $Re$ . At high  $Re$  the boundary layer and the equatorial jet are decreased much, but contain most parts of the kinetic energy, which might be unfavourable to dynamo action. The volume force, on the contrary, generates a much higher momentum transfer and a heavier mixing by the driving mechanism, so that the meridional circulation is increased and that the boundary layer thickness is limited by the acting range of the force to one tenth of the gap width. In this way, the dynamo efficiency of the flow might be improved and conclusions can be drawn with respect to possible improvements of experimental setups to make the generation of a dynamo more likely.

In the first section, the differential equations of the dynamo model, the parameter of the system and the numerical implementation are introduced. The results of the spherical Couette flow with smooth boundaries are presented in the second section and those with rough boundaries in the third one. Finally in the conclusion the results are compared.

## 2.1 Dynamo model

### 2.1.1 Differential equation

Because of the geometry of the spherical gap, this problem is described in spherical coordinates  $(r, \theta, \phi)$ . The axis of rotation of the inner sphere is  $(1, 0, 0)$ . The evolution of a magnetic seed field  $\mathbf{B} = (B_r, B_\theta, B_\phi)$  within a moving electrically conducting fluid of velocity  $\mathbf{v}$  can be described by the induction equation in the magnetohydrodynamic approximation (Moffatt 1978)

$$\partial_t \mathbf{B} + \nabla \times (\mathbf{B} \times \mathbf{v}) = \lambda \nabla^2 \mathbf{B} \quad \nabla \cdot \mathbf{B} = 0 \quad (2.1)$$

where  $\lambda = 1/(\sigma\mu_0)$  is the magnetic diffusivity,  $\sigma$  is the electric conductivity and  $\mu_0$  the vacuum permeability. Since there are no magnetic monopoles the magnetic field is divergence free. The time evolution of the magnetic field depends on two effects. The induction term on the left side is responsible for generating magnetic field lines by deforming and stretching processes whereas the second term on the right hand side describes diffusive processes, which let the magnetic field decay. These equations deal with a dense plasma where the collision frequency is large compared to the cyclotron frequency of the charged particles, so that the mean free path is very short and velocities are small compared to the speed of light. In that way the plasma behaves like a fluid and its velocity field  $\mathbf{v} = (v_r, v_\theta, v_\phi)$  can be described by the Navier-Stokes equation

$$\partial_t \mathbf{v} + (\mathbf{v} \cdot \nabla) \mathbf{v} = -\frac{1}{\rho} \nabla p + \nu \nabla^2 \mathbf{v} + \mathbf{F} \quad \nabla \cdot \mathbf{v} = 0. \quad (2.2)$$

$\nu$  is the kinematic viscosity,  $\rho$  is the density,  $p$  is the pressure and  $\mathbf{F}$  is a volume force which will be defined later. Near the onset of dynamo action, the magnetic field strength is low enough so that the back reaction of the magnetic field on the plasma via the Lorentz force can be neglected. In kinematic dynamo theory, the velocity field then behaves independently from the magnetic field. The induction equation is linear in  $\mathbf{B}$  and the temporal evolution of the magnetic field is given by  $\mathbf{B} \sim e^{st}$  with growth rates  $s$  as Eigenvalues, which indicates whether the magnetic field strength grows or decays. The kinematic dynamo onset is defined by  $s = 0$ . In addition, in these studies, we assume the plasma as incompressible, which is a good assumption for the conditions, e.g., in the earth's core or in liquid sodium experiments. Hence  $\rho$  is constant and the continuity equation just yields a velocity field which is divergence free. In the following the reference scales of the variables are defined:

$$\begin{aligned}
 t &\rightarrow t' \frac{1}{\Omega_i} \\
 \mathbf{x} &\rightarrow \mathbf{x}' d \\
 \mathbf{v} &\rightarrow \mathbf{v}' d \Omega_i \\
 p &\rightarrow p' \rho d^2 \Omega_i^2 \\
 \mathbf{F} &\rightarrow \mathbf{F}' d \Omega_i^2
 \end{aligned} \tag{2.3}$$

Time is scaled by the reciprocal inner core's rotation rate  $\Omega_i$  and the length is scaled by the gap width  $d$ . In the dimensionless system the gap width is from now on equal to unity and with the aspect ratio of  $\eta = r_i/r_o = 1/3$  the radii are  $r_i = 0.5$  and  $r_o = 1.5$ . In the following only the dimensionless variables are considered and for simplicity the primes are omitted. All reference scales are collected into the following dimensionless Parameters

$$\begin{aligned}
 \text{Re} &= \frac{\Omega_i d^2}{\nu} \\
 \text{Rm} &= \frac{\Omega_i d^2}{\lambda} \\
 \text{Pm} &= \frac{\text{Rm}}{\text{Re}} = \frac{\nu}{\lambda}
 \end{aligned} \tag{2.4}$$

The Reynolds number  $\text{Re}$  describes the balance of inertial to viscous forces and the magnetic Reynolds number  $\text{Rm}$  is a measure for the ratio of inductive to dissipative effects of the magnetic field. By varying  $\text{Rm}$ , the growthrate  $s$  of the magnetic field strength changes and the onset of a magnetic instability at the kinematic dynamo onset at  $\text{Rm}_c$  can be found. The dimensionless MHD equations then read

$$\partial_t \mathbf{B} + \nabla \times (\mathbf{B} \times \mathbf{v}) = \frac{1}{\text{Rm}} \nabla^2 \mathbf{B} \quad \nabla \cdot \mathbf{B} = 0, \tag{2.5}$$

$$\partial_t \mathbf{v} + (\mathbf{v} \cdot \nabla) \mathbf{v} = -\nabla p + \frac{1}{\text{Re}} \nabla^2 \mathbf{v} + \mathbf{F} \quad \nabla \cdot \mathbf{v} = 0. \tag{2.6}$$

These dimensionless parameters, however, are made on the basis of the inner boundary velocity, which is taken as a measure for the characteristic velocity of the fluid. A more convenient quantity to describe the dynamical state of the system would be the temporal and spatially averaged dimensionless velocity  $\overline{v_{rms}}$  of the saturated state, which has to be

calculated a posteriori.

$$\overline{v_{rms}} = \sqrt{\frac{2E_{kin}}{V}} \quad E_{kin} = \left\langle \int \frac{1}{2} \mathbf{v}^2 dV \right\rangle \quad (2.7)$$

$E_{kin}$  is the kinetic energy integrated over the whole spherical gap and the brackets denote temporal averaging. The appropriate lapse of time has to be considered well. The advective turnover time  $\tau_a$  is the time, a fluid particle needs to complete one meridional circulation. The length of this path is  $L_a \approx 2d + \pi/2(r_i + r_o) \approx 5d$  and the time  $L_a/v_c$  with  $v_c = \Omega_i d \overline{v_{rms}}$  as the characteristic velocity along this path. Since the time in the dimensionless equations is related to the reciprocal rotation rate, like in equation 2.3 the corresponding dimensionless advective time scale is  $\tau'_a = v_c/(L_a * \Omega_i)t = \overline{v_{rms}}/5t$ . Taking  $\overline{v_{rms}} = 0.1$  the advective turnover time  $\tau_a = 1$  would be  $t = 50$  rotational time steps. An appropriate time range for averaging would be a few ten advective turnover times. Based on this characteristic velocity the dimensionless parameters look like

$$\begin{aligned} \overline{\text{Re}} &= \text{Re} \overline{v_{rms}} \\ \overline{\text{Rm}} &= \text{Rm} \overline{v_{rms}}. \end{aligned} \quad (2.8)$$

In table 2.1, the parameter limits of the simulations and the Maryland experiment are shown.

	Simulation	Experiment
Re	$1.6 \times 10^4$	$5 \times 10^7$
Rm	$10^4$	950
$\overline{\text{Re}}$	$10^3$	
$\overline{\text{Rm}}$	800	
Pm	$\sim 1$	$10^{-5}$

Table 2.1: Parameter limits of the simulations and the Maryland experiment (Zimmerman 2010).

### Boundary conditions

The two different surface types of the inner boundary are simulated by specific boundary conditions in combination with variation of the volume force  $\mathbf{F}$ . The smooth boundary

is realised by no-slip conditions, where the velocity of the fluid at the inner boundary is equal to the inner core's velocity and at the outer boundary equal to zero. The volume force  $\mathbf{F}$  in equation 2.6 is zero

$$\mathbf{v} = \boldsymbol{\Omega}_i \times \mathbf{r} \text{ at } r = r_i, \quad \mathbf{v} = 0 \text{ at } r = r_o. \quad (2.9)$$

Only the very inner layer of the fluid is forced by the boundary and the momentum transfer occurs by viscous drag. Thus, the boundary layer thickness depends on the viscosity and finally on  $\text{Re}$ .

In the rough surface simulations, the fluid is driven by a volume force which is equal to one in one tenth of the gap width near the inner sphere and zero in the rest of the volume. The volume force  $\mathbf{F}$  has the following shape

$$\mathbf{F} = (-\tanh(60/d \cdot (r - r_i - d/10))/2 + 0.5) \sin \theta \hat{e}_\phi \quad (2.10)$$

and points in  $\phi$ -direction with  $\hat{e}_\phi$ , the respective unit vector. Figure 2.2 shows the radial dependence of the force amplitude which is one at the inner boundary and decreases very steep to zero at  $r_i + d/10$ . In this way the boundary layer is supposed to remain at a constant thickness of  $d/10$  for  $\text{Re} \rightarrow \infty$ . This kind of driving force extends the boundary layer thickness to the region where the force term is equal to one. In this way the energy injection rate into the fluid motion by the driving mechanism is increased and the momentum is transferred more efficiently in the whole volume. In order to avoid jumps in the velocity profile at the inner boundary, there, the boundary condition is free slip. This means that the radial component is zero at the inner boundary so that impermeability is satisfied. The radial stresses are zero as well. The outer boundary still has no-slip conditions. The disadvantage is that the force is time integrated and the boundary velocity saturates arbitrarily so that the dimensionless inner cores rotation rate might not be one. That is quite an important point to be mentioned, because the dimensionless output of the

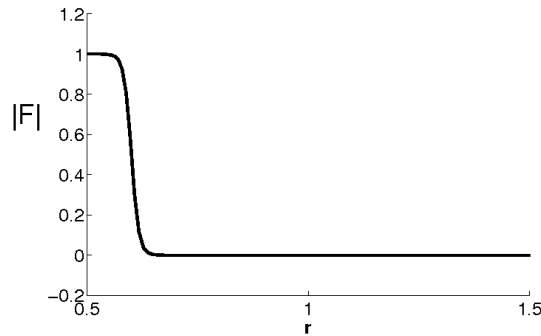


Figure 2.2: Radial dependence of the amplitude of the driving force

two simulations cannot be compared directly. In the first case the  $v_\phi$  is kept fix by the no-slip condition to  $\Omega_i r_i = 0.5$  at the inner boundary, whereas in the second case the volume force is time integrated and creates an arbitrary  $v_\phi = \omega'_i r_i$  which is not appropriate to what the dimensionless inner core's rotation rate should be, namely 1. With the introduced scalings of time and length (see eq. 2.3) the integration of the Navier-Stokes equation 2.6 gives a solution

$$\partial_t \tilde{\mathbf{v}} + (\tilde{\mathbf{v}} \cdot \nabla) \tilde{\mathbf{v}} = -\nabla \tilde{p} + \frac{1}{\tilde{\text{Re}}} \nabla^2 \tilde{\mathbf{v}} + \tilde{\mathbf{F}} \quad (2.11)$$

incorporating the following transformation

$$\begin{aligned} \mathbf{v} &= \alpha \tilde{\mathbf{v}} \\ p &= \alpha^2 \tilde{p} \\ \mathbf{F} &= \alpha^2 \tilde{\mathbf{F}} \\ t &= \tilde{t}/\alpha \\ \text{Re} &= \tilde{\text{Re}}/\alpha. \end{aligned}$$

By choosing  $\alpha = \Omega'_i$  the new solution of  $\tilde{\mathbf{v}}$  has a time averaged inner core's rotation rate of 1. On account of that another set of dimensionless parameters is necessary

$$\begin{aligned} \text{Re}' &= \text{Re} \Omega'_i \\ \text{Rm}' &= \text{Rm} \Omega'_i \end{aligned} \quad (2.12)$$

where  $\Omega'_i$  is the time averaged inner core's rotation rate in the dynamically saturated state

$$\Omega'_i = \frac{3}{8\pi r_i} \int_0^{2\pi} d\phi \int_0^\pi d\theta \sin^2 \theta \langle v_\phi(r = r_i, \theta, \phi, t) \rangle. \quad (2.13)$$

Inside the inner sphere and beyond the outer sphere the electric conductivity is zero.

### Output of physical quantities

An estimate for the energy dissipation can be deduced from the Navier-Stokes equation by multiplication with  $\mathbf{v}$  and integrating over the spherical gap:

$$\partial_t \int \frac{1}{2} \mathbf{v}^2 dV = \frac{1}{\text{Re}} \tau - \frac{1}{\text{Re}} \int (\partial_i v_j)^2 dV + \int \mathbf{F} \cdot \mathbf{v} dV \quad (2.14)$$

with

$$\tau = - \int_0^{2\pi} d\phi \int_0^\pi d\theta r^3 \sin^2 \theta \left( \partial_r v_\phi - \frac{v_\phi}{r} \right). \quad (2.15)$$

Since the non-linear term in the Navier-Stokes equation just redistributes kinetic energy to different scales it generates no energy losses. Only the energy dissipation by diffusion, boundary drag and other volume force terms remains. For the no-slip simulations the force term  $\mathbf{F}$  is zero so that in the dynamically saturated state the time averaged torque  $\tau$  is a direct measure for the energy dissipation. In the second simulation the inner boundary is free slip and the torque is equal to zero. Therefore the energy dissipation rate becomes

$$\int \tilde{\mathbf{F}} \cdot \tilde{\mathbf{v}} dV = \frac{1}{\Omega_i^3} \int \mathbf{F} \cdot \mathbf{v} dV. \quad (2.16)$$

The torque at the outer boundary is neglected because there, the velocity is much lower. In Kolmogorov's dimensional theory of turbulence, the energy dissipation  $\epsilon$  is defined by the scales of the energy carrying vortices  $\epsilon \sim v_0^3/l_0$ . The dimensions of the torque in the simulation is  $[\tau] = \text{kgm}^2/\text{s}^2 \rightarrow \rho d^5 \Omega_i^2$ . Apart from that, we get the energy dissipation rate  $\epsilon \sim \tau \Omega_i / \rho d^3$ . The torque should therefore evolve like  $\tau \sim \rho d^3 v_0^3 / \Omega_i l_0$ . Without dimensions and taking  $l_0 = d$  it simply reads  $\tau \sim (v_0 / \Omega_i d)^3$ .

Important quantities which are investigated are the kinetic energy

$$E_{kin} = \int |\mathbf{v}|^2 dV, \quad (2.17)$$

the magnetic energy

$$E_B = \int |\mathbf{B}|^2 dV, \quad (2.18)$$

and the kinetic helicity

$$H = (\nabla \times \mathbf{v}) \cdot \mathbf{v}. \quad (2.19)$$

### 2.1.2 Numerical realisation

A pseudo spectral method for incompressible flow simulations in spherical geometry has been worked out by Tilgner (1999). In this geometry it is suitable to describe the equations in spherical coordinates  $(r, \theta, \phi)$ . Since both fields, the velocity field and the magnetic field, are solenoidal, their three components can be described by two scalar functions respectively. The convenient way to do this is a toroidal-poloidal decomposition of these vector fields

$$\begin{aligned}\mathbf{v} &= \nabla \times \nabla \times (\Phi_v \hat{e}_r) + \nabla \times (\Psi_v \hat{e}_r) \\ \mathbf{B} &= \nabla \times \nabla \times (\Phi_B \hat{e}_r) + \nabla \times (\Psi_B \hat{e}_r),\end{aligned}\tag{2.20}$$

where  $\hat{e}_r$  denotes the unit vector in radial direction.  $\Phi_{B,v}$  is the poloidal field and  $\Psi_{B,v}$  the toroidal field. In this way the divergence of both fields is equal to zero. The toroidal part of the vector fields has no radial components and points tangentially to spherical surfaces. A purely radial vector field, like a dipole field, would be described by a poloidal field. The poloidal and toroidal scalar fields are expanded in spherical harmonics.

$$\begin{aligned}\Phi_v &= r \sum_{l=1}^{\infty} \sum_{m=-l}^l [\Phi_v]_l^m(r) \hat{P}_l^m(\cos \theta) e^{im\phi} \\ \Psi_v &= r^2 \sum_{l=1}^{\infty} \sum_{m=-l}^l [\Psi_v]_l^m(r) \hat{P}_l^m(\cos \theta) e^{im\phi} \\ \Phi_B &= \sum_{l=1}^{\infty} \sum_{m=-l}^l [\Phi_B]_l^m(r) \hat{P}_l^m(\cos \theta) e^{im\phi} \\ \Psi_B &= \sum_{l=1}^{\infty} \sum_{m=-l}^l [\Psi_B]_l^m(r) \hat{P}_l^m(\cos \theta) e^{im\phi},\end{aligned}\tag{2.21}$$

where  $\hat{P}_l^m(\cos \theta)$  are simply the Legendre Polynomials with the prefactors which appear in the spherical harmonics

$$\hat{P}_l^m(\cos \theta) = \sqrt{\frac{4\pi}{2l+1} \frac{(l+m)!}{(l-m)!}} P_l^m(\cos \theta).\tag{2.22}$$

By this definition, the components of the velocity field are

$$\begin{aligned}
 v_r &= \sum_{l=1}^{\infty} \sum_{m=-l}^l \frac{l(l+1)}{r} [\Phi_v]_l^m(r) \hat{P}_l^m(\cos \theta) e^{im\phi} \\
 v_\theta &= \sum_{l=1}^{\infty} \sum_{m=-l}^l \frac{\partial}{\partial r} [\Phi_v]_l^m(r) \frac{\partial}{\partial \theta} \hat{P}_l^m(\cos \theta) e^{im\phi} + \frac{imr}{\sin \theta} [\Psi_v]_l^m(r) \hat{P}_l^m(\cos \theta) e^{im\phi} \\
 v_\phi &= \sum_{l=1}^{\infty} \sum_{m=-l}^l \frac{im}{\sin \theta} \frac{\partial}{\partial r} [\Phi_v]_l^m(r) \hat{P}_l^m(\cos \theta) e^{im\phi} - r [\Psi_v]_l^m(r) \frac{\partial}{\partial \theta} \hat{P}_l^m(\cos \theta) e^{im\phi}.
 \end{aligned} \tag{2.23}$$

Except for the respective prefactor  $r$  and  $r^2$  of the poloidal and toroidal fields (see eq. 2.21), the magnetic field is obtained by the same formulars. Since the velocity and the magnetic field is real  $[\Phi]_l^{m*} = [\Phi]_l^{-m}$  and  $[\Psi]_l^{m*} = [\Psi]_l^{-m}$ , with  $*$  denoting the complex conjugated quantity, only one half of the complex Fourier components ( $m \geq 0$ ) have to be stored. In radial direction the spectral amplitudes are expanded in Chebychev polynomials  $T_n(x) = \cos(n \arccos x)$ . With  $x = 2(r - r_i) - 1$  and taking the collocation points at

$$r_j = r_i + \frac{1}{2} \left( 1 + \cos \frac{j-1}{N_r-1} \right), \quad j = 1 \dots N_r, \tag{2.24}$$

the expansion function becomes  $T_n(r_j) = \cos \left( n\pi \frac{j-1}{N_r-1} \right)$ , which is just a cosine transformation. By this method the grid point density is higher at the boundaries, which increases the resolution of boundary layers. The timestep for the fields is a Crank-Nicolson scheme of second order.

The boundary conditions in the smooth surface simulations arise from 2.9. Since in dimensionless variables  $\Omega_i$  is equal one, the toroidal field at the inner boundary is

$$[\Psi_v]_{l=1}^{m=0}(r = r_i) = \sqrt{\frac{4\pi}{3}}. \tag{2.25}$$

All other components  $[\Psi_v]_l^m(r = r_i, r_o)$  and  $[\Phi_v]_l^m(r = r_i, r_o)$  are zero.

In the rough surface simulation this boundary condition is replaced by the force term, which defines the toroidal field according to equation 2.10

$$[\Psi_v]_{l=1}^{m=0}(r) = \sqrt{\frac{4\pi}{3}} (-\tanh(60/d \cdot (r - r_i - d/10))/2 + 0.5). \tag{2.26}$$

The main difference between equation 2.25 and 2.26 is that the latter one is integrated in time, whereas the first one is just a Dirichlet boundary condition. After a number of time steps, some important quantities are stored like, e.g., the kinetic energy  $\frac{1}{2} \int \mathbf{v}^2 dV$ . Inserting 2.23, the kinetic energy can be expressed for each spectral component. In this way the different contributions of axisymmetric, non-axisymmetric toroidal and poloidal fields to the total kinetic energy can be separated and spectral distributions can be analyzed.

$$\begin{aligned}
 E_{\Phi} &= 4\pi \int \sum_l \sum_{m=1}^l \frac{l(l+1)(l+m)!}{2l+1(l-m)!} \left( l(l+1) |[\Phi_v]_l^m|^2 + \left| r \frac{\partial}{\partial r} [\Phi_v]_l^m + [\Phi_v]_l^m \right|^2 \right) \\
 E_{\Psi} &= 4\pi \int \sum_l \sum_{m=1}^l \frac{l(l+1)(l+m)!}{2l+1(l-m)!} r^4 |[\Psi_v]_l^m|^2
 \end{aligned} \tag{2.27}$$

The time step is limited by the CFL-number which is dependent on the velocity and resolution (Fletcher 1991)

$$\min \left[ \frac{r}{l_{max} \sqrt{v_{\theta}^2 + v_{\phi}^2}} \right] \tag{2.28}$$

If the time step exceeds this limit, numerical information would pass to the next but one gridpoint within one time step and the numerical solution diverges.

## 2.2 Smooth surface

In the following, the results of the smooth surface simulations are presented. A smooth surface implies that the fluid is coupled to the boundary only by viscous drag. In the simulation, this is done by so-called no-slip boundary conditions, which have exactly this effect. The fluid velocity equals the boundary velocity in  $\phi$ -direction at the inner core. All other components are zero. The momentum of the fluid is transferred outwards by viscous drag so that near the inner boundary,  $v_\phi$  decreases rapidly outward in radial direction. In this region, the fluid moves in the equatorial plane and flows outward in an equatorial jet towards the outer sphere. The recirculation takes place in the entire rest of the volume. The basic topology of the flow is similar to the  $s2t1$ -flow and has opposite helicity in the two different hemispheres.  $s2$  denotes a quadrupolar poloidal field and  $t1$  means that the toroidal velocity does not change sign over latitude. Such a flow has been studied by Dudley and James (1989) and is basically capable to create a dynamo.

In the first subsection, the purely hydrodynamic properties of the system will be described in dependence on  $Re$ . For this purpose equation 2.6 was integrated in time and only the parameter  $Re$  was changed. The main focus is on the onset of the hydrodynamic instability with a dominant wave number  $m = 2$ , a possible dominant wave number  $m = 3$  and developing turbulence at high  $Re$ . In the subsequent subsections, the evolution of a weak magnetic seed field within this moving plasma is investigated. In order to do this, the equations 2.6 and 2.5 are integrated simultaneously, where  $Re$  and  $Rm$  are the two relevant parameters. The kinematic dynamo threshold for several  $Re$  between  $10^3$  and  $1.667 \times 10^4$  is found by adapting the parameter  $Rm$  so that the growth rate  $s$  of the magnetic fieldstrength is zero. Here, the nearest values at  $s = 0$  for  $s < 0$  and  $s > 0$  are linearly interpolated. The most important issue is the dynamo mechanism of the specific flow at different  $Re$ . At low  $Re$ , it consists of a single wave propagation and evolves strong turbulence at high  $Re$ . This is relevant to answer the question, in which way these results can be extrapolated to the parameter regime of liquid sodium experiments.

In these simulations,  $Re$  will be varied from  $10^3$  up to a value of  $1.667 \times 10^4$ , which requires a resolution of 32 radial grid points. 128 in latitude and 256 in azimuthal direction with respective dealiasing at 85 and 170 up to  $Re \approx 2 \times 10^4$ . From there, the radial resolution is increased to 64 with 256 in latitude and 512 in  $\phi$ -direction and respective dealiasing at 170 and 340. An important point is that the boundary layer should be well resolved, which means that at least 5 grid points should be within the boundary layer. For the highest value of  $Re = 1.667 \times 10^4$ , it is only resolved by 4 grid points. In order to check the reliability of these results, one simulation at the kinematic dynamo onset was repeated with 128 radial gridpoints.

### 2.2.1 Hydrodynamic properties

The basic state of the spherical Couette flow is axisymmetric with respect to the axis of the inner core's rotation and symmetric with respect to the equatorial plane. By increasing  $Re$ , the hydrodynamic system undergoes two transitions.

The first occurs at a critical value of  $Re_h \approx 1500$  ( $\overline{Re}_h \approx 105$ ), where small non-axisymmetric perturbations increase and an instability develops in form of a propagating wave on the equatorial jet with a dominant azimuthal wave number  $m = 2$ . Amplitudes of higher harmonics of this wave number also increase, whereas amplitudes of odd modes decrease in time. This is shown in Figure 2.3, where the spectrum of the kinetic energy is plotted over spherical harmonic order  $m$ . The amplitude of the dominant wave number  $m = 2$  is approximately  $10^{-3}$  and the next harmonic is already about one order of magnitude lower. In the right panel, a snapshot of the isosurface of 3% of the maximal local kinetic energy at  $\overline{Re} = 133$  is plotted. The local kinetic energy is simply the absolute value of the velocity vector at each grid point. It can be seen that values of 97% of the maximal local kinetic energy are within the boundary layer near the inner core and the equatorial jet. Thus, the highest velocities are located there. The instability bends the equatorial jet on two opposite parts respectively up and down, like it is shown in the figure.

The azimuthal wave number of  $m = 2$  is in agreement with Hollerbach et al. (2006), who computed the linear onset of non-axisymmetric instabilities and their most unstable azimuthal wave number for a wide range of aspect ratios. At an aspect ratio of  $\eta = 1/3$ , the first instability develops at  $Re \approx 1500$  with the most unstable azimuthal wave number

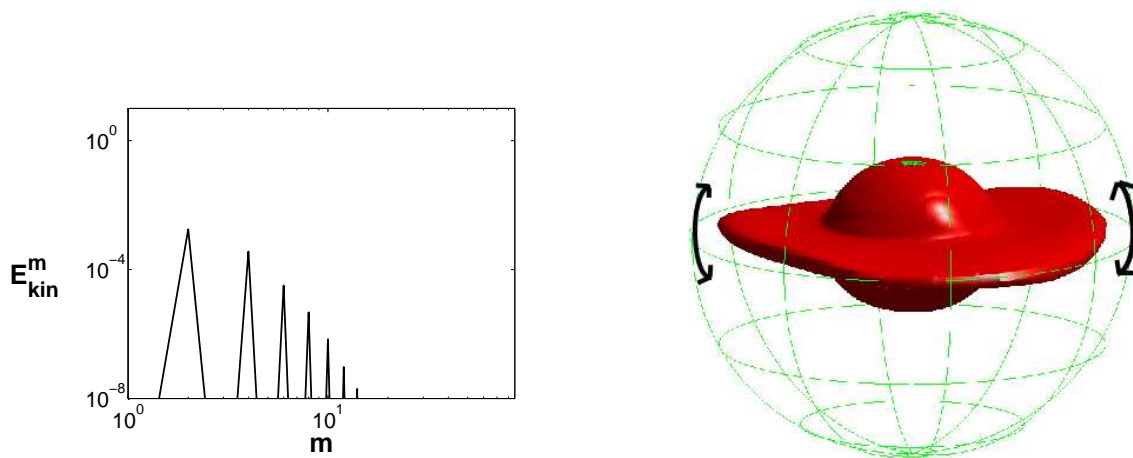


Figure 2.3: Snapshots of the kinetic energy spectrum plotted against spherical harmonic degree  $m$  (left) and isosurface of 3% of the maximum local kinetic energy (right) at  $\overline{Re} = 133$ .

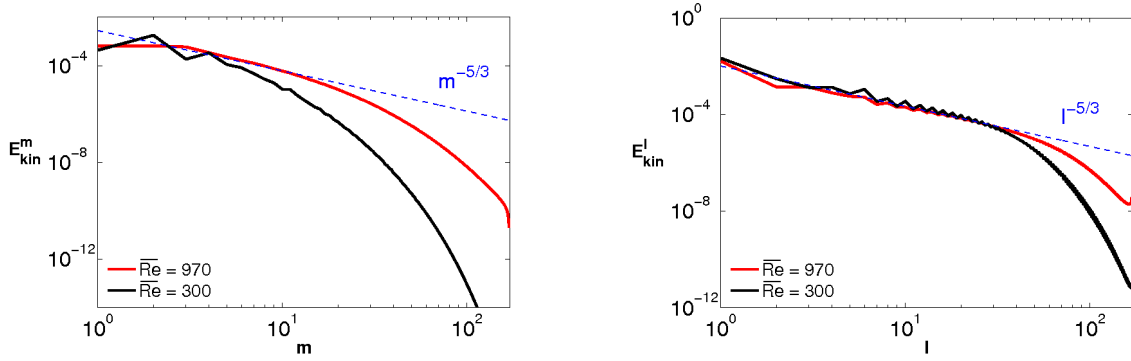


Figure 2.4: Temporally and spatially averaged spectra of  $E_{kin}$  plotted against  $m$  (left) and  $l$  (right) at  $\overline{Re} = 300$  (black) and 970 (red).

changing from  $m = 3$  to  $m = 2$ . Guervilly and Cardin (2010) performed full three-dimensional simulations with an aspect ratio of  $\eta = 0.35$ . They found a corresponding onset of the instability with the same azimuthal wave number of  $m = 2$ .

Another transition occurs at  $Re_s = 2800$  ( $\overline{Re}_s = 178$ ). Beyond this value, in addition, non-axisymmetric instabilities with odd wave numbers  $m$  occur. For further increasing  $\overline{Re}$ , the spectrum begins to flatten and approaches a power law of  $m^{-5/3}$ . This is shown in Figure 2.4, where on the left side the kinetic energy is plotted against spherical harmonic order  $m$  at  $\overline{Re} = 300$  and 970. The large scales of the velocity, however, remain on the same order of magnitude. The azimuthal wave number  $m = 2$  remains dominant at least up to  $\overline{Re} \approx 300$ . In the right panel, the kinetic energy spectrum is plotted against the spherical harmonic order  $l$ . The spectrum also approaches a powerlaw of  $l^{-5/3}$  at high  $\overline{Re}$ . The kinetic energy spectra develops the same powerlaw like in Kolmogorov's theory of turbulence (Davidson 2004), although it is plotted against spherical harmonic order and degree. Kolmogorov, on the contrary, argues on the bases of spectral properties of plane waves. The correct relation between a plane wave vector  $k$  and the spherical harmonic degree  $l$  is  $k^2 = l(l + 1)$  (Lorenzani 2001). This implies that the concept of an inertial range and a dissipation scale can be applied on the spectral properties of spherical harmonics. The scale, at which the power spectra kink and become steeper than  $l^{-5/3}$ , therefore indicates the viscous scale  $l_v$ , which shifts to higher wave numbers for increasing  $Re$ .

In Figure 2.5, the three characteristic regimes,  $Re < Re_h$  (left panel),  $Re_h < Re < Re_s$  (middle panel) and  $Re > Re_s$  (right panel), are displayed. The components of the velocity field are shown as snapshots in a meridional cut. The radial component at the top, the  $\theta$ -component in the middle and the  $\phi$ -component at the bottom. On the left side, at small  $Re < Re_h$ , the velocity is axisymmetric with respect to the axis of rotation. The radial component shows high velocities in the equatorial plane towards the outer sphere, while everywhere else it is at least one order of magnitude lower. The  $\theta$ -component has relatively large velocities at the inner boundary, where the fluid flows into the equatorial

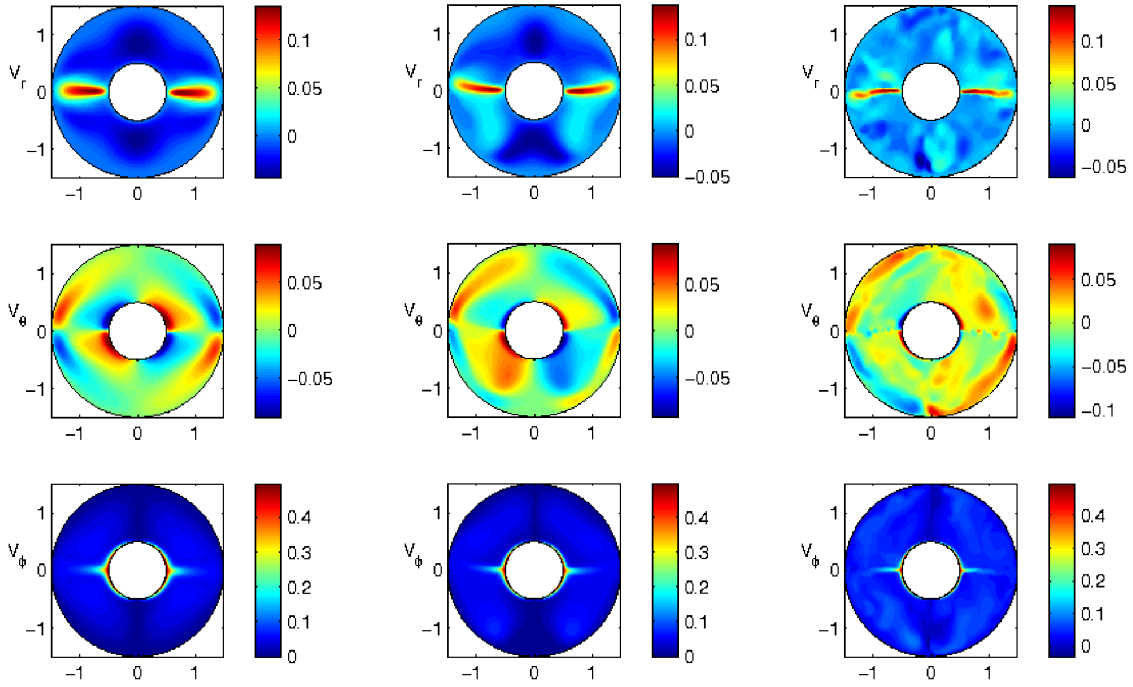


Figure 2.5: Snapshots of  $v_r$  (top),  $v_\theta$  (middle) and  $v_\phi$  (bottom) in a meridional cut at  $Re = 1.25 \times 10^3$  (left),  $2.5 \times 10^3$  (middle) and  $10^4$  (right).

plane, and at the outer boundary, where it circulates back to the poles. The  $\phi$ -component is large near the inner core within the boundary layer. Compared to the other components,  $v_\phi$  reaches the highest values, being six times larger than the radial velocity in the equatorial jet and one order of magnitude larger than the absolute maximum of  $v_\theta$ . In the central plot for  $Re_h < Re < Re_s$ , the first non-axisymmetric instability with the azimuthal wave number  $m = 2$  is shown. Accordingly, the equatorial jet is bended up- and downward and the symmetry with respect to the axis of rotation is only given by a shift of  $\phi \rightarrow \phi + \pi$  or  $\phi \rightarrow \phi + \pi/2$  and an additional reflection with respect to the equatorial plane. Due to the increase of  $Re$ , the equatorial jet as well as the boundary layer becomes thinner. Finally, on the right side, at high  $Re$ , the symmetry is entirely broken, the velocity becomes increasingly small scale structured and turbulence develops. The equatorial jet and the boundary layer further diminish.

The boundary layer is defined as the distance, within which the  $\phi$ -velocity averaged on spherical surfaces  $\hat{v}_\phi(r)$  drops below the mean of the boundary velocity  $\hat{v}_\phi(r_i)$  and the radially averaged velocity  $\bar{v}_\phi$

$$d_B = \frac{\hat{v}_\phi(r_i) + \bar{v}_\phi}{2}. \quad (2.29)$$

In Figure 2.6, on the left side, the boundary layer thickness of the  $\phi$ -velocity is plotted. It decreases proportional to  $Re^{-1/2}$  as predicted by laminar boundary layer theory Acheson (1990). On the right side,  $E_{kin}$  is plotted. Because of the weak mixing, it saturates at

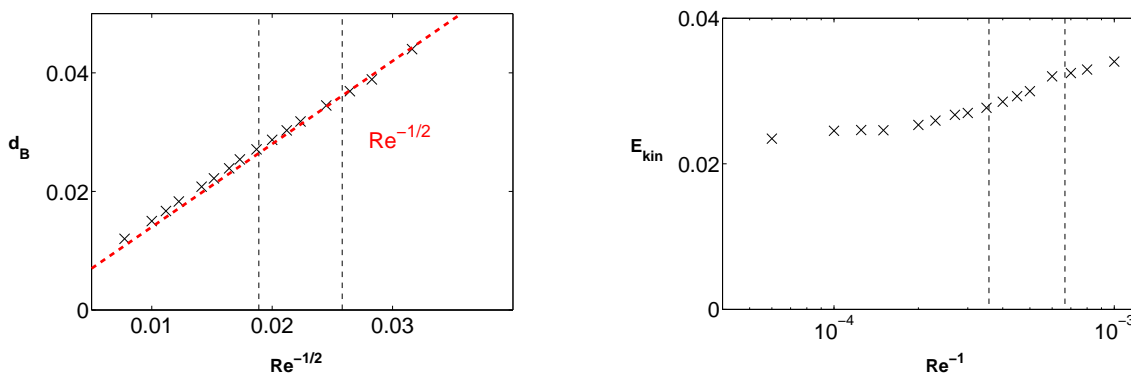


Figure 2.6: Boundary layer thickness  $d_B$  plotted against  $Re^{-1/2}$  (left) and  $E_{kin}$  plotted against  $Re^{-1}$ . The vertical dashed lines indicates the transitions at  $Re_h$  and  $Re_s$ .

quite low  $Re$  and approaches a constant value of  $E_{kin} \approx 0.023$ . In this limit, the viscosity can be neglected. The only remaining parameters, on which the kinetic energy depends, are  $\Omega_i$  and  $\rho$ . The dimensional kinetic energy is therefore proportional to  $\Omega_i^2 \rho$  and the dimensionless kinetic energy becomes constant. The vertical dashed lines in Figure 2.6 indicate the two mentioned transitions in the characteristics of the velocity field.

An important aspect for a later discussion about the efficiency of dynamo action is that the boundary layer thickness as well as the strength of the equatorial jet decrease when the inner sphere rotates faster. At all  $Re$ , the largest contributions to the kinetic energy are localised within the boundary layer and the equatorial jet. Hence, at high  $Re$ , the kinetic energy is concentrated in a small volume near the inner sphere and the equatorial plane and is not well distributed within the entire spherical gap.

Another important quantity is the torque at the inner boundary. It gives a direct measure of the energy dissipation. In dimensionless form the torque reads

$$\tau = - \int_0^{2\pi} \int_0^\pi r^3 \sin^2 \theta \left[ \frac{\partial v_\phi}{\partial r} - \frac{v_\phi}{r} \right] d\theta d\phi, \quad (2.30)$$

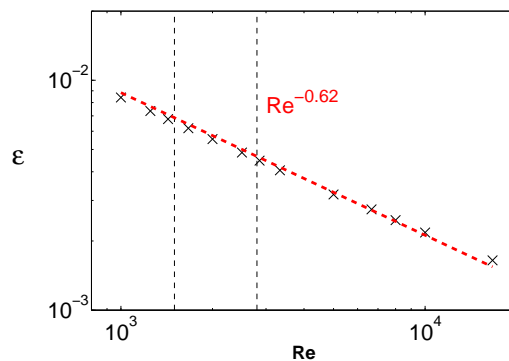


Figure 2.7: Dimensionless torque plotted against  $Re$ .

which, together with  $v_\phi$  from equation 2.23, leads to

$$\tau(\theta, \phi)|_{r_i} = \sin \theta \sum_{m,l} \left[ \frac{im}{\sin \theta} \frac{1}{r_i^2} \left( r_i^2 \frac{\partial^2}{\partial^2} [\Phi_v]_l^m - 2 [\Phi_v]_l^m \right) \hat{P}_l^m(\cos \theta) - r_i \frac{\partial}{\partial r} [\Psi_v]_l^m \frac{\partial}{\partial \theta} \hat{P}_l^m(\cos \theta) \right] e^{im\phi}. \quad (2.31)$$

Figure 2.7 shows the temporally averaged torque  $\epsilon = \langle \tau \rangle / \text{Re}$  as a function of  $\text{Re}$  and decreases with  $\text{Re}^{-0.62}$ . Giving the assumption that  $\partial_r v_\phi \sim d_B^{-1}$ , equation 2.30 would yield a proportionality of  $\text{Re}^{-1/2}$  for  $\epsilon$ . The deviation might arise from the fact that  $\partial_r v_\phi$  at  $r_i$  is not the same as it is across the boundary layer.

The dimensional torque is  $\tau \rho \Omega_i d^3 \nu$ . The three diameter experiment in Maryland measured a torque  $\tau' \rho \nu^2 r_i$  that increases with  $\text{Re}^{1.89}$ . With the same dimension, the torque in the simulations yield a proportionality of  $\tau' \sim \tau \text{Re} \sim \epsilon \text{Re}^2 \sim \text{Re}^{1.38}$ . The deviation comes most probably from the fact, that the boundary shear layer in the simulations is still laminar. The experiments exhibits strong turbulent flows, in which the shear layer destabilizes at relatively low  $\text{Re}$  compared to the possible limit (Zimmerman 2010).

It is well known that in turbulent plasma flows, the helicity plays a crucial role in generating magnetic fields, since helical flows are often favourable for dynamo action (Moffatt 1978). They can produce a large-scale dynamo via the  $\alpha$ -effect, as it was shown in the experiments in Karlsruhe (Muller and Stieglitz 2002), and in numerical simulations Brandenburg (2009), Graham et al. (2012). The spherical Couette flow is topologically related with the  $s2t1$ -flow of Dudley and James (1989), which includes a zonal flow in  $\phi$ -direction and a meridional component. That, in turn, creates helicity of opposite sign in the two hemispheres. In Figure 2.8 snapshots of the isosurfaces of the kinetic helicity are plotted for  $\overline{\text{Re}} = 130$  and 970. Red color marks positive helicity and blue color marks negative helicity surfaces of one percent of the maximal and minimal helicity, respectively. This means that helicity from 1% up to 100% of the maximal/minimal helicity amplitude is concentrated at the inner boundary and near the equatorial plane. This is reasonable, since in these simulations, the meridional circulation is quite weak compared to the boundary velocity, and the helicity is dominated by the strong  $\phi$ -rotation within the boundary layer. Enhancing the helicity in the entire volume to an equal value by increasing the meridional circulation would probably increase the dynamo quality, which could be achieved by a better coupling between the moving boundary and the fluid.

There is a surprising observation related with the dominant wave number of the non-axisymmetric instability. Usually for  $\text{Re}_h < \text{Re} < \text{Re}_s$ , small non-axisymmetric perturbations increase with the dominant mode  $m = 2$ . At  $\text{Re} > \text{Re}_s$ , all modes are unstable and the spectra of the velocity field looks like those in Figure 2.4. Starting from this state and lowering  $\text{Re}$  below  $\text{Re}_s$ , amplitudes of high wavenumbers are damped by diffusion

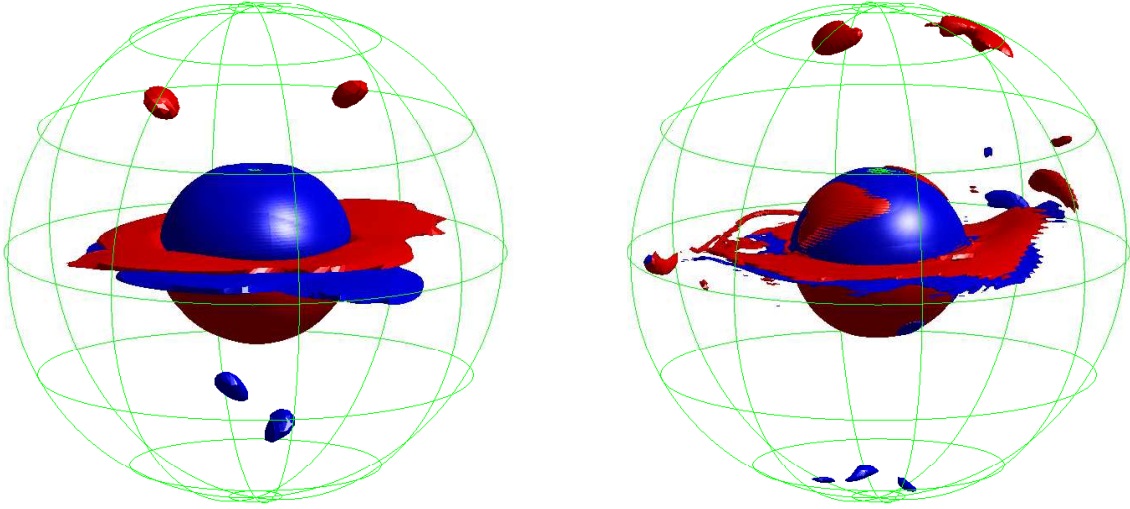


Figure 2.8: Snapshots of the isosurface of 1% of the maximum kinetic helicity at  $\overline{\text{Re}} = 132$  (left) and 970 (right). Blue indicates negative and red positive helicity. The respective maximal/minimal values are  $\pm 3.5$  and  $\pm 10.0$

and the non-axisymmetric instabilities turn again into a single wave propagation, like discussed in the first paragraphs. By this means, it is possible that the dominant wave number becomes  $m = 3$  and only every third wave number in  $m$  remains as additional stable wave number. The left panel of Figure 2.9 shows the kinetic energy spectra plotted against spherical harmonic degree  $m$ . Hollerbach et al. (2006) found the most unstable mode for this aspect ratio to be on the transition from  $m = 2$  to 3. However, in simulations with an aspect ratio of  $\eta = 0.4$ , growing non-axisymmetric instabilities still have a dominant wavenumber of  $m = 2$ , although the linear onset predicts a different one. On the right side, an snapshot of the isosurface of 3% of the maximal local kinetic energy is shown. According to the dominant wave number, the equatorial jet has three wave crests. The left panel of Figure 2.10 shows the bifurcation diagram of the kinetic energy of the two branches with different wave numbers  $m = 2$  (black) and  $m = 3$  (blue), which get separated at the onset of the first non-axisymmetric instability and slowly merge at  $\overline{\text{Re}} > \overline{\text{Re}}_s$ . The kinetic energy of the simulation, where the instability exhibits a dominant wave number of  $m = 3$  is higher than the corresponding simulation with  $m = 2$ . The right panel shows the dimensionless torque  $\epsilon$  at the inner boundary for the same simulations. These values of  $E_{kin}$  and  $\epsilon$  represent the state, where  $\partial_t E_{kin} = 0$ . From Equation 2.14, it follows that the viscous dissipation is balanced by the energy input, expressed by the torque. Thus, the energy dissipation with  $m = 2$  is slightly higher than with  $m = 3$ .

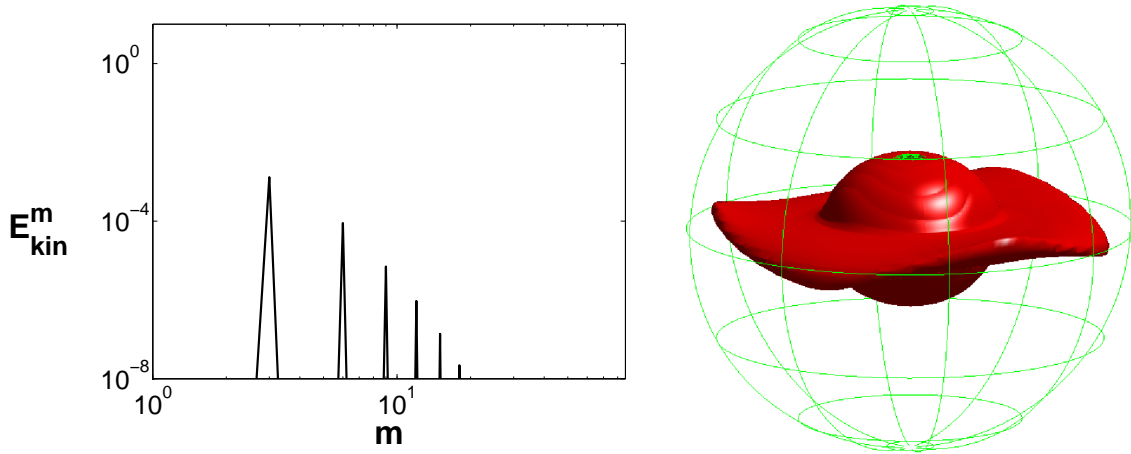


Figure 2.9: Snapshots of the kinetic energy spectrum plotted against the spherical harmonic degree  $m$  (left) and isosurface of 3% of the maximum local kinetic energy (right) at  $\overline{\text{Re}} = 130$ .

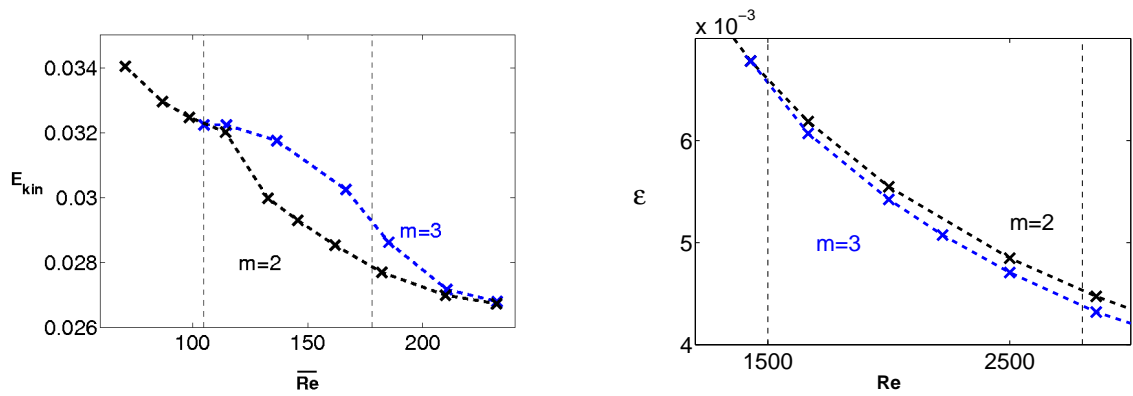


Figure 2.10: Kinetic energy bifurcation diagram (left) and the dimensionless torque at the inner boundary (right) of the  $m = 2$  and  $m = 3$  instability.

## 2.2.2 Kinematic dynamo threshold

In the following, the results of the magnetohydrodynamic simulations are presented. Additionally to the momentum equation (eq. 2.6), the induction equation (eq. 2.5) was solved numerically and intergrated in time. Thereby, the behaviour of the magnetic field within the plasma flow was investigated. Further, solutions of zero growth rate were evaluated, which denote the kinematic dynamo threshold  $\text{Rm}_c$ . The dynamo onset and the evolution of a seed magnetic field in the spherical Couette flow has already been investigated by Guervilly and Cardin (2010) incorporating the full non-linear equations<sup>1</sup>. The aspect ratio in their studies was  $\eta = 0.35$  and the magnetic boundary conditions were

<sup>1</sup>In this sense, non-linear means the MHD equations including the Lorentz force in the Navier-Stokes equation

different. They implemented boundaries, which had the same conductivity as the fluid and also investigated ferromagnetic boundaries. The conductivity of the boundary was found to be irrelevant for  $Rm_c$ , but enhanced the saturation level of the magnetic energy. The crucial result was that the dynamo onset  $Rm_c$  increases with  $Re$ , which makes this kind of flow unfavourable for dynamo experiments. The extrapolation of the results to the parameter regime relevant for the experiment yields unreachable  $Rm_c$ .

In order to find the onset of magnetic field amplification,  $Rm$  is increased for several  $Re$  until the growth rate becomes positive. The transition  $Rm_c$  is determined by linear interpolation. Figure 2.11 shows the simulations in the  $(\overline{Re}, \overline{Rm})$ -plane and in the  $(\overline{Re}, Pm)$ -plane. The vertical dashed lines denote the transitions  $Re_h$  and  $Re_s$  between the three characteristic velocity fields, which were described in the previous section. The thick black dashed line between the red dots and the blue asterisks shows the dynamo threshold. In addition lines of constant  $Pm = 1$  in the upper panel and  $\overline{Rm} = 800$  in the lower panel are plotted. To point out an interesting aspect, note that  $Pm$  is larger than one except for the simulation at the highest  $\overline{Re} \approx 970$ . Since  $Pm$  represents the ratio of kinematic viscosity and magnetic diffusivity, it also indicates the ratio of the smallest scales of the velocity field and the magnetic field and the ratio of viscous dissipation to ohmic diffusion. For  $Pm > 1$ , the dissipation scale of the magnetic field is smaller. This will turn out to be an important point at high  $Re$ , when the velocity field is highly turbulent.

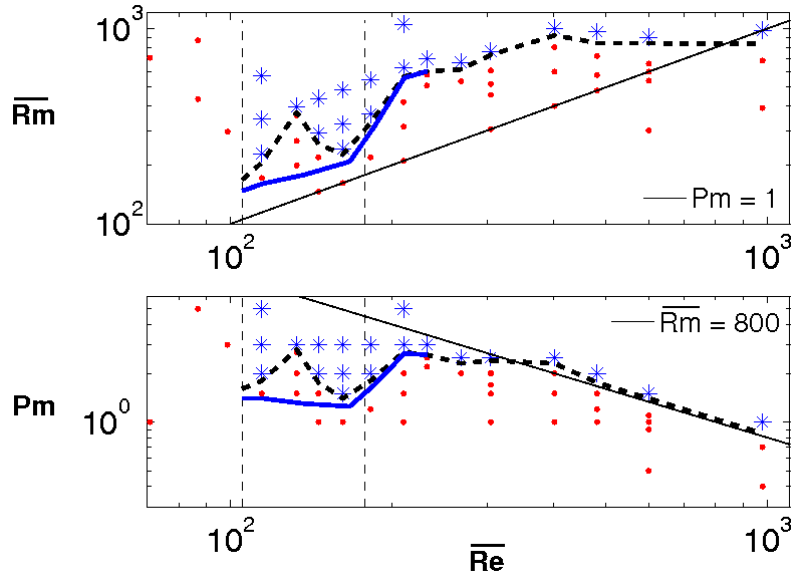


Figure 2.11: Dynamo onset in the  $(\overline{Re}, \overline{Rm})$ -plane (upper panel) and in the  $(\overline{Re}, Pm)$ -plane (lower panel). Failed dynamos are indicated by red dots and acting dynamos by blue asterisks. The thick dashed line marks  $\overline{Rm}_c$  for  $m = 2$  and the blue thick solid line for  $m = 3$ . The straight lines are  $Pm = 1$  (upper panel) and  $\overline{Rm} = 800$  (lower panel). Vertical dashed lines mark the transitions  $Re_h$  and  $Re_s$ .

In the following, the three regions- axisymmetric flow, nearly stationary instability, and turbulent regime- are investigated with respect to the behaviour of the magnetic field and the dynamo mechanism.

### 2.2.3 Stationary regime

The shape of the velocity field is axisymmetric up to  $Re_h \approx 1500$  ( $\overline{Re}_h = 105$ ). In this regime, no dynamo action could be found even at large  $Pm = 10$ . This is in agreement with Guervilly and Cardin (2010), who didn't find any dynamo action for an axisymmetric velocity field either. Since Dudley and James (1989) proved that this kind of flow is basically capable of creating a dynamo, at very high  $Rm$ , the generation of magnetic energy should occur. On account of that, the ratio of meridional circulation to toroidal kinetic energy could be crucial to improve the dynamo efficiency.

Once the flow becomes unstable at  $\overline{Re} > \overline{Re}_h$ , the flow is able to sustain a dynamo at low  $Pm$ . The development of the dynamo threshold at  $\overline{Re}_h < \overline{Re} < \overline{Re}_s$  has a characteristic peak at  $\overline{Re}_{sy} \approx 140$  (Fig. 2.11). At first,  $Rm_c$  increases with  $\overline{Re}$  for  $\overline{Re} < \overline{Re}_{sy}$ , and then decreases for  $\overline{Re} > \overline{Re}_{sy}$  up to the second transition at  $\overline{Re}_s$ . There, it increases again and remains nearly constant up to high  $\overline{Re}$ . Most striking is that the shape of the velocity does not change significantly within the range  $\overline{Re}_h < \overline{Re} < \overline{Re}_s$  but the dynamo threshold changes significantly. The main evolution of the velocity field is the decrease of boundary layer thickness and the thickness of the equatorial jet. The dominant azimuthal wave number remains  $m = 2$  within this range of  $\overline{Re}$ .

Time series of the radial velocity at a fixed point in the equatorial plane are plotted in the left panel of Figure 2.12. The focus is on the temporal variation and not on the amplitude so that the curves are just plotted on top of each other for a better comparability. It can be seen that the phase velocity of the propagating wave decreases with increasing  $\overline{Re}$ .

In the right panel in Figure 2.12, the time evolution of the torque at the inner core, obtained by equation 2.31, is displayed for different  $\overline{Re}$ . The amplitude of the oscillation is about 1% of the total mean torque. The fact that the torque at the inner core is not constant suggests a superposition of higher harmonics and the dominant propagating instability. A single wave propagation would exert a constant torque. The next higher wave number  $m = 4$  is only one order of magnitude lower than the dominant one. The frequency of the torque's oscillation decreases with  $\overline{Re}$  as well, similar to the phase velocity of propagating wave on the equatorial jet.

The dynamo onset decreases significantly with the occurrence of the non-axisymmetric hydrodynamic instability at  $\overline{Re}_h$ . Thus, the generation of the magnetic field must be closely related to the this propagating instability.

Such wave-like motion can approximately be composed of a stationary state and a time

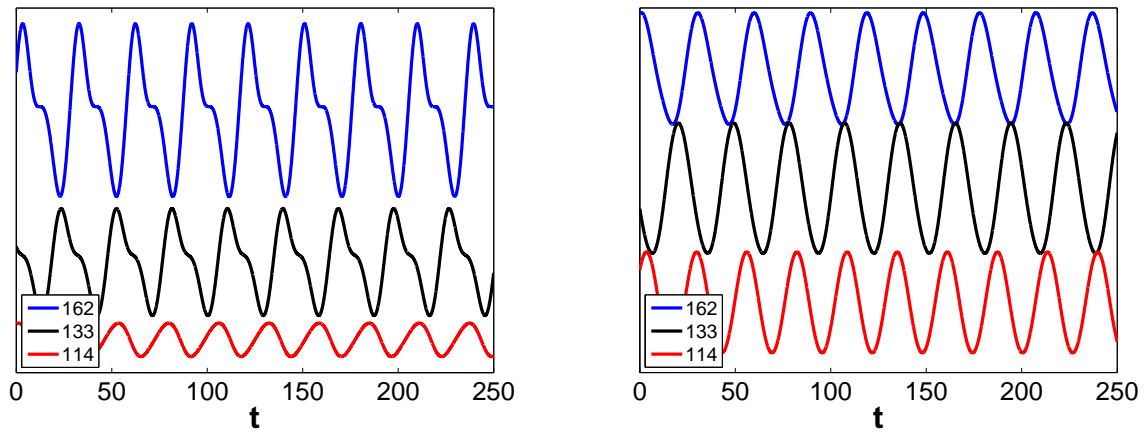


Figure 2.12: Time evolution of  $v_r$  at a fixed point in the equatorial plane (left) and the torque (right) at  $\overline{\text{Re}} = 114$  (red), 133 (black) and 162 (blue). The amplitudes are arbitrary since the focus is on the time dependence

dependent phase. This has already been done in simulations related with the Madison experiment by Reuter et al. (2009). They found that growth rates exhibit resonance effects,

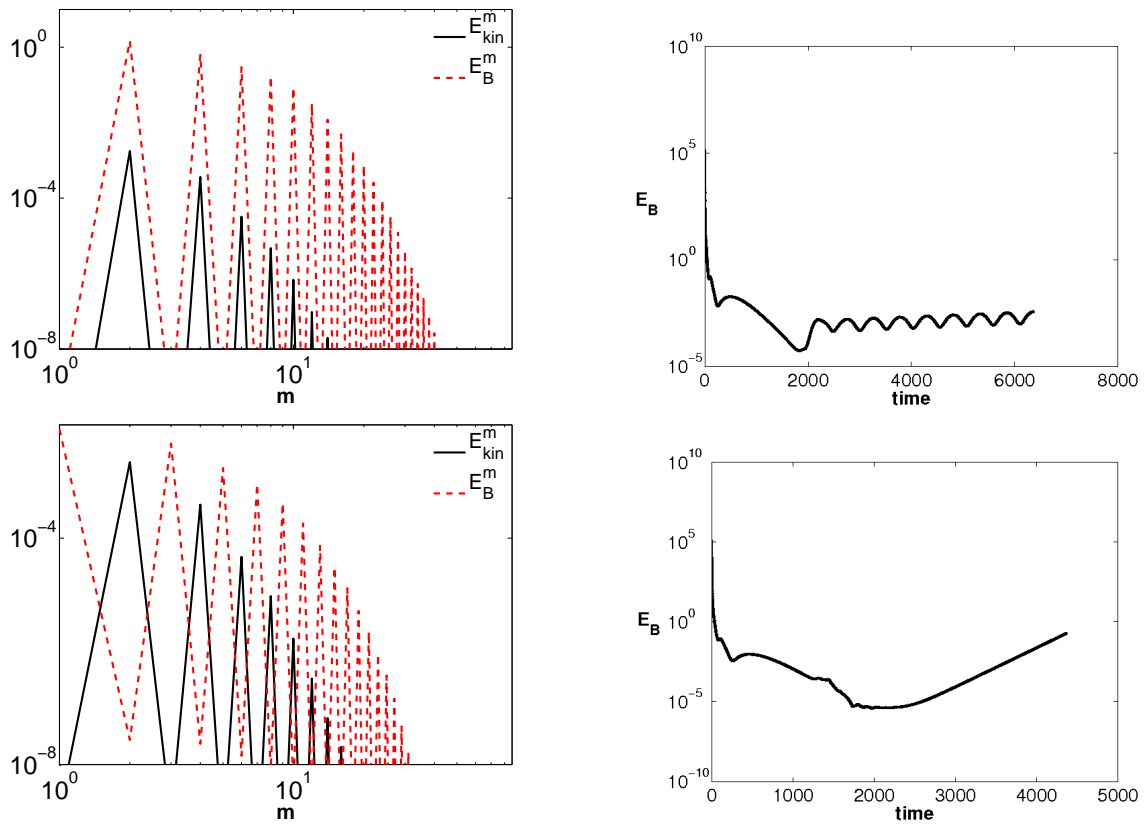


Figure 2.13: Kinetic energy spectra (black) and magnetic energy spectra (red) plotted against  $m$  (left) and according time evolution of the magnetic energy (right) at  $\text{Re} = 133$  (top) and 162 (bottom).

depending on the phase velocity of the propagating wave.

Figure 2.13 shows the spectrum of magnetic and kinetic energy plotted against spherical harmonic degree  $m$  on the left side and the respective time evolution of the magnetic energy on the right side at  $\overline{\text{Re}} = 133$  (top) and 162 (bottom). These plots contrast the evolution of the magnetic field slightly before and behind the peak at  $\overline{\text{Re}}_{\text{sy}}$  in the dynamo threshold (Fig. 2.11). The spectra show that at  $\overline{\text{Re}} < \overline{\text{Re}}_{\text{sy}}$  the same modes of the velocity field are excited in the magnetic field. As a consequence, the magnetic field and the velocity field have the same symmetry with respect to the axis of rotation with a dominant azimuthal wave number  $m = 2$ . Amplitudes of higher harmonics of this wave number are amplified as well, whereas the energy in odd wave numbers dissipates. Once the kinetic energy has saturated and the non-axisymmetric instability has fully developed, the time evolution of the magnetic energy can be represented by a superposition of an exponential increase and an oscillation.

On the contrary at  $\overline{\text{Re}} > \overline{\text{Re}}_{\text{sy}}$ , the magnetic energy in odd wave numbers increases in time and dissipates in even wave numbers. Thereby, the hemispherical symmetry of the magnetic field breaks up. The time evolution of the magnetic energy now exhibits a time independent growth rate, and an oscillation can be observed.

In order to investigate the effect of the phase velocity of the propagating instability on the dynamo threshold and on the time evolution of the magnetic energy, only the induction equation is integrated. A stationary velocity field with fully developed instability is taken for the induction term in equation 2.1. By varying the mean flow of this velocity field, the drift velocity of the propagating wave can be altered artificially:

$$[\tilde{\Psi}_v]_{l=1}^{m=0}(r) = [\Psi_v]_{l=1}^{m=0}(r) - \tilde{\omega} \sqrt{\frac{4\pi}{3}}. \quad (2.32)$$

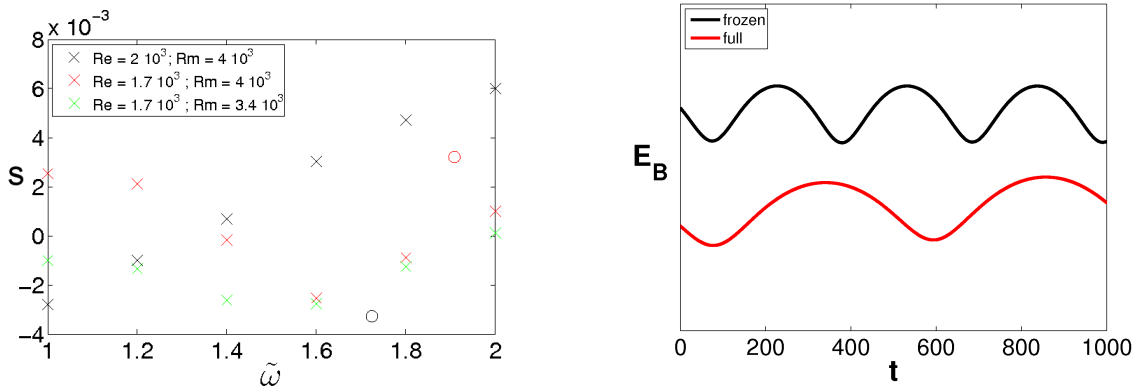


Figure 2.14: Growth rates  $s$  plotted against phase velocity  $\tilde{\omega}$  for different  $\text{Rm}$  (left). The velocity fields are generated with hydrodynamic simulations at the corresponding  $\text{Re}$ . The right panel shows the time evolution of the magnetic energy in the full simulation and in the corresponding frozen flux simulation.

The induction equation is then just a linear differential equation with a constant differential operator  $\mathfrak{J}$

$$\frac{\partial}{\partial t}\mathbf{B} = \mathfrak{J}\mathbf{B}, \quad (2.33)$$

for which temporally averaged exponential growth rates can be found in dependence of  $\text{Rm}$ . The change of the drift is given by  $\tilde{\omega}$ . Since the constant differential operator in equation 2.33 is time-independent with solutions  $\mathbf{B} \sim e^{st}$ , eigenvalues  $s$  indicate the growth rate of the respective magnetic field. The time evolution of the velocity field in Figure 2.12 shows a phase velocity of the instability of about  $\sim 1.6\% - 1.9\%$  of the inner sphere's rotation rate. Note that an azimuthal wave number of  $m = 2$  creates two wave crests, so that every second wave crest belongs to one full rotation of the instability.

In Figure 2.14, the growth rates at  $\text{Rm} = 4 \times 10^3$  are plotted against  $\tilde{\omega}$  for two different frozen velocity fields. The velocity fields were taken from hydrodynamic simulations at  $\text{Re} = 2 \times 10^3$  and  $1.7 \times 10^3$ . The simulations with  $\text{Re} = 1.7 \times 10^3$  were repeated with a different  $\text{Rm}$ . The according drift velocities and growth rates of the full simulations are plotted as circles (red for  $\text{Re} = 1.7 \times 10^3$ ;  $\text{Rm} = 4 \times 10^3$  and black  $\text{Re} = 2 \times 10^3$ ;  $\text{Rm} = 4 \times 10^3$ ). Only the evolution of  $s$  at  $\text{Re} = 2 \times 10^3$  shows a monotonous behaviour over the entire range of  $\tilde{\omega}$ . The sets of simulations with the same velocity field at  $\text{Re} = 1.7 \times 10^3$  but different  $\text{Rm}$  (red and green crosses), however, show that the variation of  $\tilde{\omega}$  significantly effects the growth rate. In the range of the dynamical simulations at  $\tilde{\omega} \approx 1.6 - 1.9\%$ , the growthrate decrease with diminishing phase velocity, as shown in Figure 2.14. This result agrees with the behaviour of the dynamo threshold up to  $\overline{\text{Re}} = 133$ .

Nevertheless, the growth rates of the frozen flux simulations are totally different from those of the full simulations. In Figure 2.14 (right), the temporal evolution of the magnetic energy of a frozen velocity field simulation is plotted together with the corresponding dynamical simulation. In both types of simulation, the frequency of the magnetic energy oscillation changes slightly with the phase velocity of the propagating wave. Also, in both cases, the superposition of an exponential growth and an oscillation can be observed.

Therefore, the conclusions drawn from these frozen flux simulations can only be seen as a qualitative result. The oscillatory behaviour of the magnetic energy, however, seems to be generated in the stationary part of the velocity field, since it is also present in the frozen velocity field simulations. On the other hand, phase velocities, for which the time evolution of the magnetic energy is pure exponential, were not found. Even at  $\text{Re} > \text{Re}_{\text{sy}}$ , where the full simulations suggests such a behaviour, the frozen flux simulations do not show it. Therefore, the symmetry breaking of the magnetic field at  $\text{Re} = \text{Re}_{\text{hy}}$  must be on account of the slight time dependence of the velocity field, due to the superposition of the dominant mode and higher harmonics.

In Figure 2.15, snapshots of the magnetic field are shown at three points in time during one maximum of the magnetic energy to another (right panel of Figure 2.14). The patches

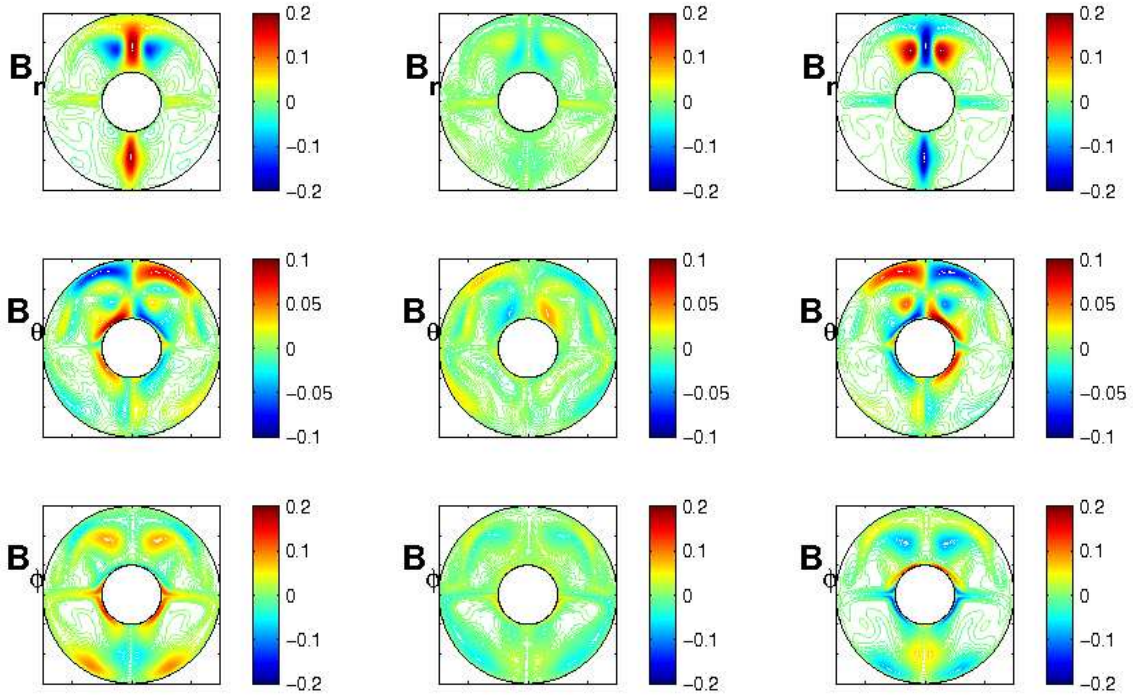


Figure 2.15: Snapshots of  $B_r$  (top),  $B_\theta$  (middle) and  $B_\phi$  (bottom) in a meridional cut during one frozen flux simulation from one maximum (left) to the minimum (middle) to the next maximum (right).

of maximal and minimal magnetic field strength vanish before they finally reappear with opposite sign. The same mechanism can also be observed in full dynamical simulations, where the patches move with the propagating instability. This can be seen as a special kind of a propagating magnetic wave in a frozen flux of plasma.

Magnetic field strength is generated due to magnetic field line stretching in the vicinity of velocity gradients at the boundary layer and the equatorial jet. In the range  $\overline{Re}_h < \overline{Re} < \overline{Re}_s$ , this occurs mainly near the wave crests, as well as above and below the equatorial plane, as seen in Figure 2.16. It shows snapshots of 10% of the total local magnetic energy and 3% of the maximum local kinetic energy at  $\overline{Re} = 114, 133$  and  $162$ . The local magnetic energy is the absolute value of the magnetic field vector at each grid point. The main contribution to the magnetic energy comes from the toroidal magnetic field. The  $m = 2$  symmetry of the magnetic field at the two lowest  $\overline{Re}$  is clearly visible. At  $\overline{Re} = 162$ , the symmetry of the magnetic field with respect to the two hemispheres breaks. The change in the symmetry of the magnetic field seems responsible for the increased dynamo efficiency. So far, it remains unclear, which small-scale characteristics of the velocity field actually trigger this change in the amplification of different modes.

As a first approach, it is assumed that the change in the symmetry of the amplified magnetic field modes is responsible for the significant change in the efficiency of the flow to

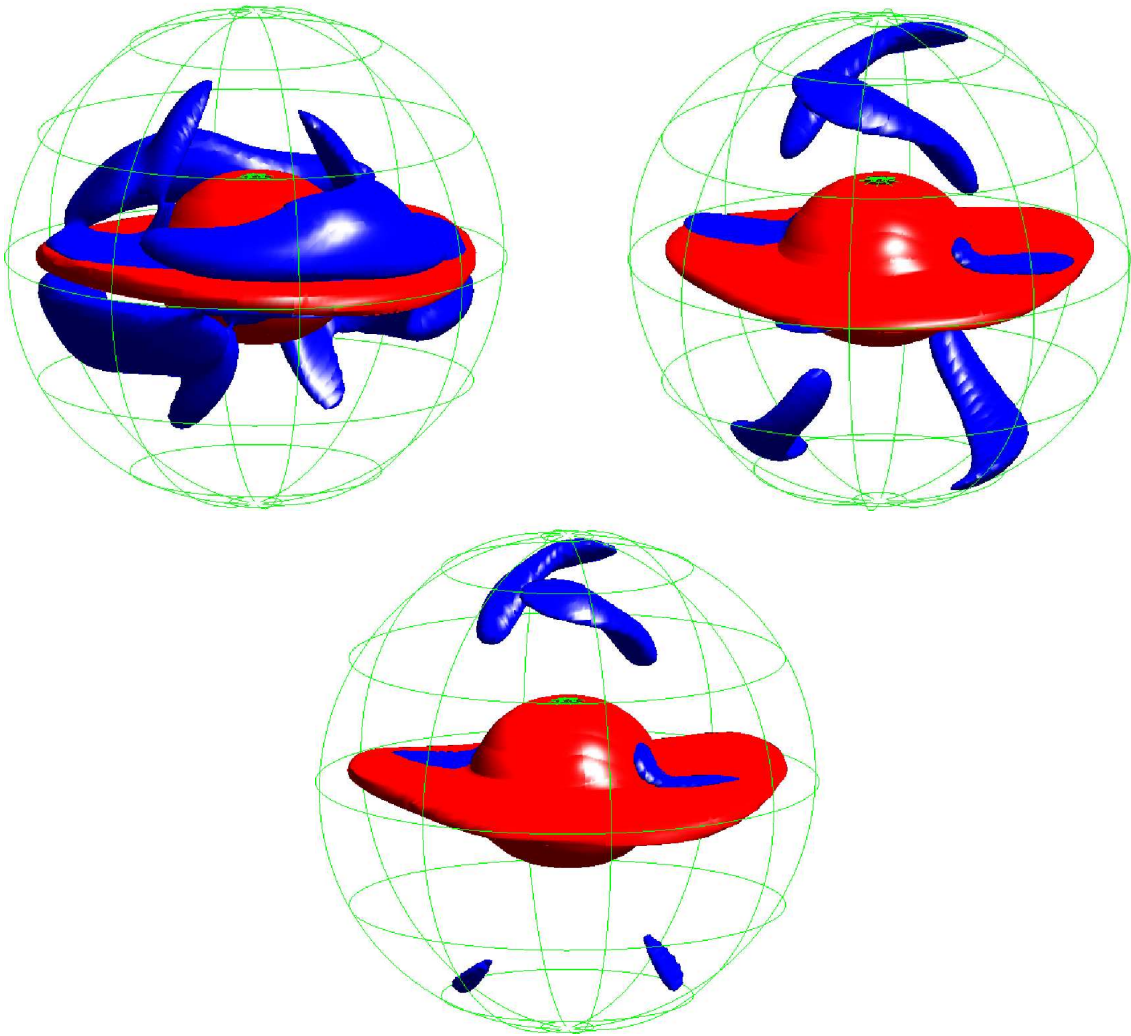


Figure 2.16: Snapshots of isosurfaces of 3% of the maximum local kinetic energy (red) and 10% of the maximum local magnetic energy (blue) at  $\overline{Re} = 114$  (left), 133 (right) and 162 (bottom).

dynamo action. In order to verify this assumption, one can consider the dynamo threshold of the  $m = 3$  instability, which is additionally plotted in Figure 2.11 for  $\overline{Re}_h < \overline{Re} < \overline{Re}_s$  (blue thick line). Two things can be seen. First, the threshold is lower for  $m = 3$  than it is for  $m = 2$ . Secondly, it increases monotonously with  $Re$ . The spectral distribution of the magnetic and kinetic energy is plotted in Figure 2.17 for  $\overline{Re} = 133$ , whereas the symmetry of the magnetic field does not undergo any change in the range  $\overline{Re}_h < \overline{Re} < \overline{Re}_s$ . At any  $\overline{Re}$ , the amplitude of every third wave number  $m$  is amplified, whereas the others decrease. The magnetic field and the velocity field have the same symmetry. The evolution of the magnetic energy is plotted in Figure 2.17 on the right hand side and shows also a similar exponential increase with a superposed oscillatory behaviour like in the top panel of Figure 2.13.

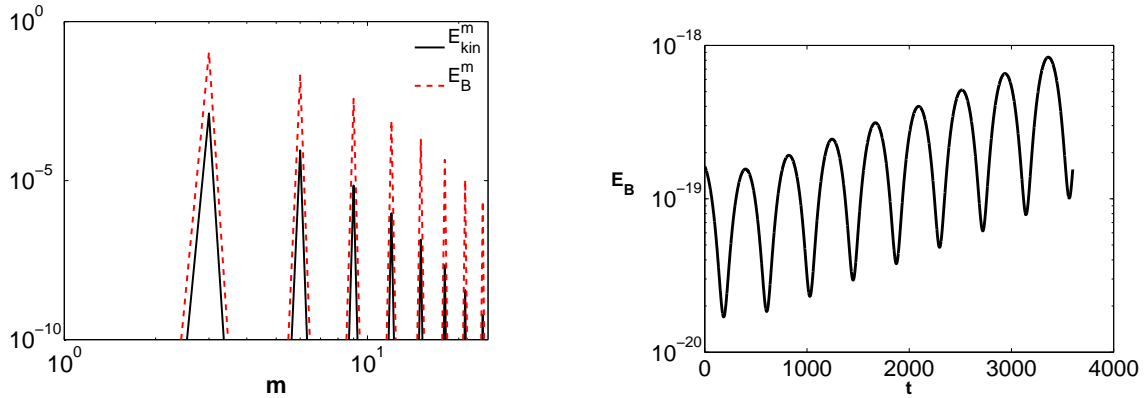


Figure 2.17: Kinetic (black) and magnetic (red) energy spectra plotted against spherical harmonic degree  $m$  at  $\text{Re} = 133$  (left) and the corresponding time evolution of the magnetic energy (right).

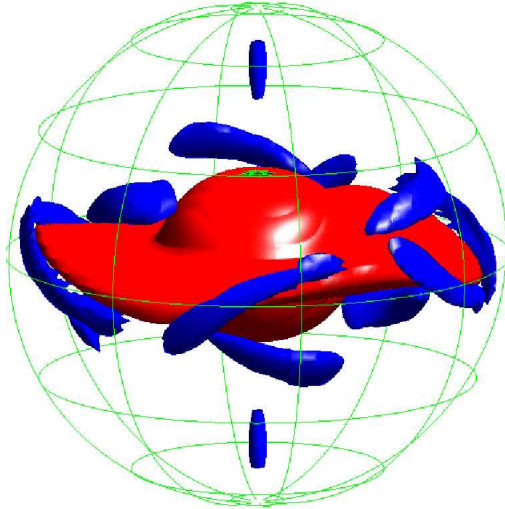


Figure 2.18: Snapshot of the isosurface of 3% of the maximum local kinetic energy (red) and 10% of the maximum local magnetic energy (blue) during a simulation with a dominant  $m = 3$  instability.

Figure 2.18 shows again isosurfaces of 3% of the maximum local kinetic energy and 10% of the maximum local magnetic energy. The generation of magnetic energy occurs in the vicinity of the propagating wave crests, where the velocity field is strongly sheared. The main contribution to the magnetic energy is given by the toroidal component of the magnetic field. Here, the symmetry of the velocity field and the magnetic field, respectively, agree as well. Since the magnetic field is generated in the vicinity of the wave crests of the equatorial jet, it is likely that the  $m = 3$ -instability is more efficient to dynamo action than with  $m = 2$ .

Remembering the two branches of the kinetic energy for  $m = 2$  and  $m = 3$ , plotted against  $\overline{\text{Re}}$  in Figure 2.10, another explanation for the increased efficiency could be that in this

range, the kinetic energy of the flow with  $m = 3$  is 10% higher than with  $m = 2$ , which increases the induction.

### 2.2.4 Dynamo mechanism in the turbulent regime

At  $Re_s \approx 2800$ , instabilities develop over the entire range of wave numbers  $m$ . The regularity of the velocity field entirely breaks up, whereas  $m = 2$  still remains the dominant mode at first. Due to the appearance of many modes, the velocity field temporally fluctuates without any periodicity anymore. The temporally fluctuations lower the dynamo quality and the dynamo threshold increases immediately. Figure 2.19 shows the evolution of the non-axisymmetric toroidal kinetic energy (left) and the magnetic energy (right) of a simulation at  $\overline{Re} = 210$ , which is close above  $Re_s$ . The plot in the left panel shows the temporal development of a small non-axisymmetric perturbation and the saturation of the corresponding toroidal kinetic energy. It remains nearly constant for a short time and finally develops a strong time dependence, which indicates the destabilisation of higher modes on the equatorial jet. The corresponding time evolution of the magnetic field shows a nearly constant growth rate as far as the dominant mode has developed. With the onset of strong time fluctuations, the growth rate becomes time dependent as well and decreases significantly. The growth rate even changes sign so that the dynamo eventually shuts down. At that point, the dynamo is still mainly driven by the dominant wave number  $m = 2$ , whereas the time dependence due to the instability of higher wave numbers decreases the efficiency of the flow to dynamo action.

Important points to discuss in this context include, first, the effect of small-scale velocity structures to dynamo action, which become increasingly dominant the higher  $Re$  gets. Secondly, the question, if the dynamo threshold remains at a constant  $Rm_c$  for  $Re \rightarrow \infty$ .

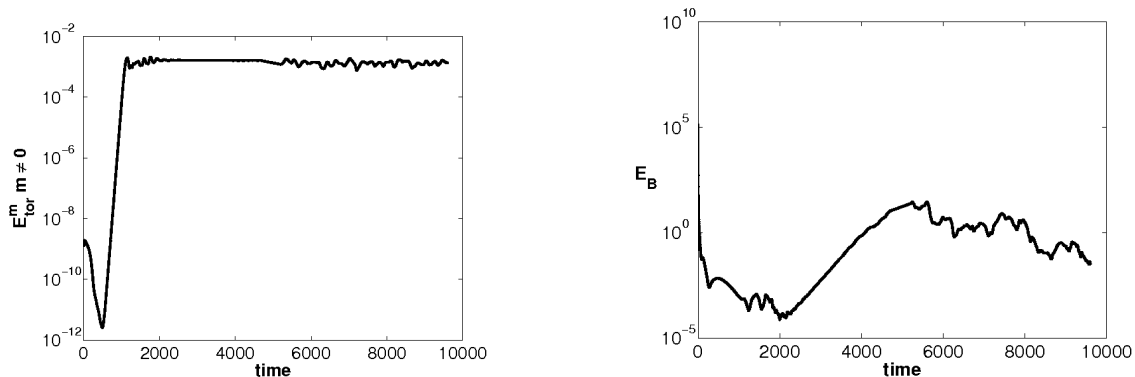


Figure 2.19: Time evolution of the non-axisymmetric toroidal kinetic energy (left) and the magnetic energy (right) at  $\overline{Re} = 210$ .

This, in turn, is related to the question, whether, thirdly, the turbulent spherical Couette flow is a small-scale dynamo (and thus driven by small-scale velocity vortices) or a large-scale dynamo, where the  $m = 2$  instability and the mean flow mainly generate the magnetic field. One crucial parameter in this discussion is  $Pm$ , which indicates the ratio of the dissipative scales of the fluid and the magnetic field. Except for simulations at the highest  $\overline{Re} = 970$ , the dynamo threshold is at  $Pm > 1$  (Fig. 2.11). Since  $Pm = 1$  denotes an important transition, where the smallest scales of both fields are on comparable length scales, the extrapolation of these results to higher  $Re$  have to be well considered.

These considerations are relevant to many astrophysical objects, where turbulent gas flows at very low  $Pm$  can create large magnetic fields, which are comparable to the size of the same objects. A lot of research has focused on the improvement of our understanding of turbulent dynamos at very low  $Pm$ . In order to get sufficient  $Rm$  so that dynamo action is achieved, the simulations require high  $Re$  and, thus, are computationally demanding. In these simulations, the scale of the generated magnetic field can be much larger than the energy carrying vortices of the flow. The dynamo is a large-scale dynamo, which can be described, for instance, with the help of the mean field theory (Moffatt 1978, Krause and Rädler 1980). In these cases, helicity plays a crucial role. Turbulent simulations at small  $Pm$  have been made using, e.g., randomly polarised helical waves (Brandenburg 2009) or helical G.O. Roberts like forced flows (Ponty and Plunian 2011), who succeeded to gain large-scale dynamos. On the other hand it is also possible that the magnetic energy is generated on scales which are comparable or smaller than the turbulent eddies (Schekochihin et al. 2004b, Iskakov et al. 2007, Schekochihin et al. 2007). This kind of fluctuative dynamo was investigated for example in homogeneous isotropic turbulence.

In the following, it will be shown that the dynamo of the spherical Couette flow is a large-scale dynamo and that this result implies that the dynamo threshold is independent on  $Re$ . Although spherical Couette flows exhibit anisotropic turbulence, the following argumen-

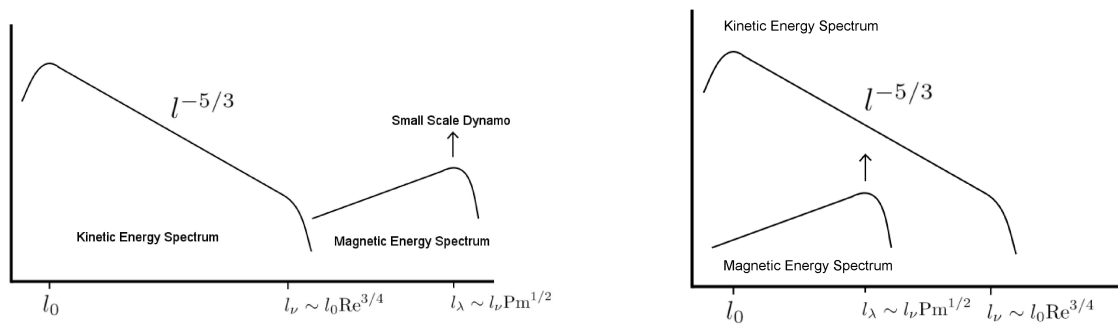


Figure 2.20: Spectral distribution of kinetic and magnetic energy in homogeneous isotropic turbulence at large (left) and low  $Pm$  (right) (Schekochihin et al. 2004b).

tation is based on homogeneous isotropic turbulence.

The usual approach to deal with homogeneous isotropic turbulence is to distinguish between different scales that exist within the system. A sketch of these scales is shown in Figure 2.20. Here, it has to be guaranteed that by identifying different length scales, a sufficient scale separation is given. The largest length scale is defined by the container size  $d$  of the specific object, which constrains the flow. In case that the fluid is driven by a large-scale motion like, e.g., the mean flows in convection cells or impeller-driven flows like in some mentioned dynamo experiments, the next smaller scale is defined by the energy injection scale  $l_0$ . In the Kolmogorov picture of turbulence, this large vortex breaks up into smaller vortices, so that the energy is transferred to smaller scales (Davidson 2004). At these scales, non-linear inertial processes are dominant. For this reason, it is called inertial range. Since energy is neither dissipated nor injected within the inertial range, but only redistributed to smaller structures, the energy flux is constant over the entire range. The spectral kinetic energy decays with powerlaw of  $l^{-5/3}$ . Finally, at the dissipative scale  $l_v$ , inertial processes become comparable to dissipation processes, where the kinetic energy is transformed into thermal energy. The kinetic energy spectrum kinks at that point and the spectrum continues steeper than the inertial range. Kolmogorov's dimensional theory of turbulence gives for the viscous scale  $l_v \sim \text{Re}^{-3/4} l_0$ . Considering a magnetic field that is stretched and twisted within these turbulent vortices, it is required to get a scale for the induction processes of the fluid at first. The generation of magnetic energy is mainly described by the induction term in the induction equation 2.1

$$\nabla \times (\mathbf{B} \times \mathbf{v}) = (\mathbf{v} \cdot \nabla) \mathbf{B} - (\mathbf{B} \cdot \nabla) \mathbf{v}. \quad (2.34)$$

The first term on the right side describes changes of the magnetic field by plasma convection. The second term describes stretching processes of the magnetic field lines by velocity gradients, which are mainly responsible for magnetic field amplification in turbulent

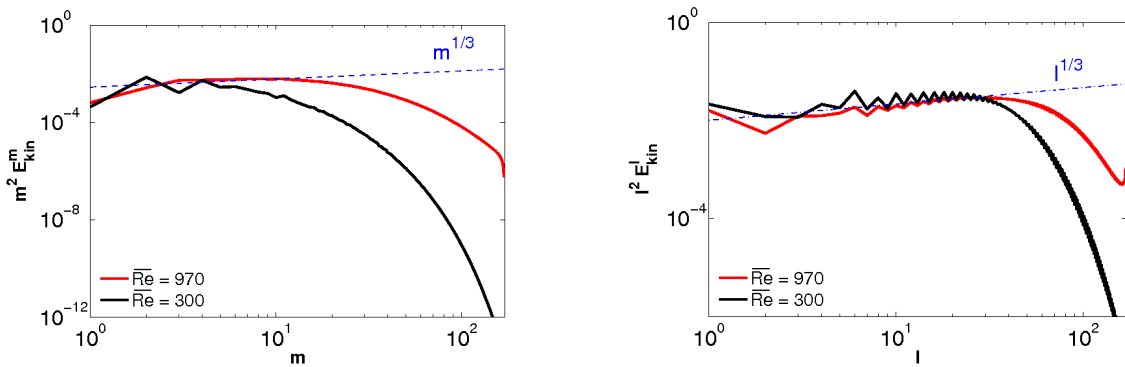


Figure 2.21: Temporally and spatially averaged turbulent rate of strain plotted against  $m$  (left) and  $l$  (right) at  $\overline{\text{Re}} = 300$  (black) and 970 (red).

flows. The square of the stretching term  $|B_i \partial_i v_j|^2 \sim E_{kin}^l l^2$  is a measure for the turbulent rate of strain and gives a powerlaw of  $\sim l^{1/3}$  in the Kolmogorov picture (Chertkov et al. 1999). It peaks at the viscous scale, where the induction process is most efficient. The temporally and spatially averaged spectra of the turbulent rate of strain are plotted in Figure 2.21 for  $\overline{Re} = 300$  and 970.

In homogeneous and isotropic turbulence, the magnetic energy is generated at the viscous scale. There, the viscous eddy turnover time equals the magnetic diffusion time, which defines an estimate for the fourth length scale, the resistive scale  $l_\lambda \sim Pm^{-1/2} l_v$  (Biskamp 2003). Two scenarios arise from this definition: low-Pm ( $Pm \ll 1$ ) and high-Pm ( $Pm \gg 1$ ) dynamos.

For  $Pm \gg 1$  (left panel in Fig. 2.20), the magnetic energy is generated by the most efficient vortices at the viscous scale and accumulated in the subviscous range at  $l_\lambda$  (Schekochihin et al. 2004b). If Re is cranked up, presumably Rm would increase as well, since the scale at which dynamo action occurs is directly affected by the viscous scales and would shift to lower scales. In this case, the behaviour of the dynamo is unpredictable concerning the extrapolation to higher parameter ranges.

For  $Pm \ll 1$  (right panel in Fig. 2.20), the dynamo is generated somewhere within the inertial range and is not affected by the smaller viscous scales. If Re is cranked up, the dynamo would not be effected by even smaller viscous scales and  $Rm_c$  would remain constant (Fauve and Petrelis 2007). This has already been worked out by some numerical works by Schekochihin et al. (2004a), Ponty et al. (2005), Iskakov et al. (2007) and Mininni (2007). In all simulations, the same phenomenon of an overshooting  $Rm_c$  as a bump in the threshold appears at  $Pm \approx 1$  before it saturates at a constant level at higher Re. In Ponty et al. (2005, 2007), this effect was found at  $0.06 \lesssim Pm \lesssim 0.2$ , which could not be reached in these simulations due to computational limitations. This effect was related to a bottleneck effect, the accumulation of kinetic energy at scales slightly larger than the viscous scale (Brandenburg and Nordlund 2011). In the kinetic energy spectra

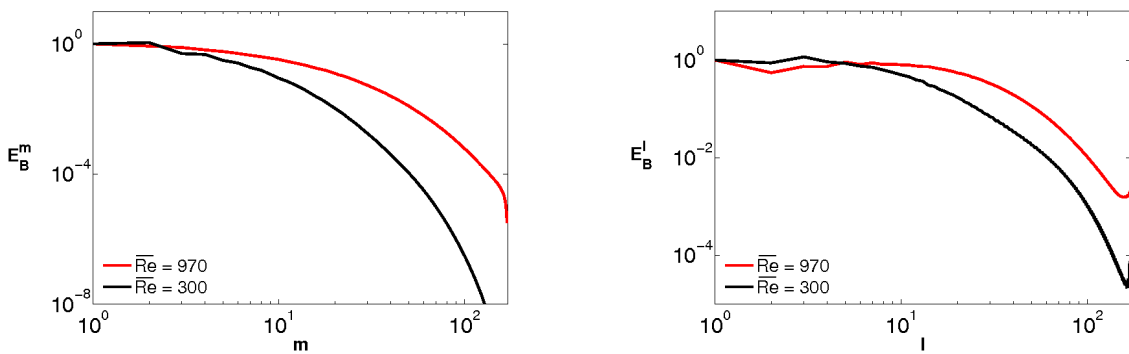


Figure 2.22: Temporally and spatially averaged Magnetic energy spectra plotted against  $m$  (left) and  $l$  (right) at  $\overline{Re} = 300$  (black) and 970 (red).

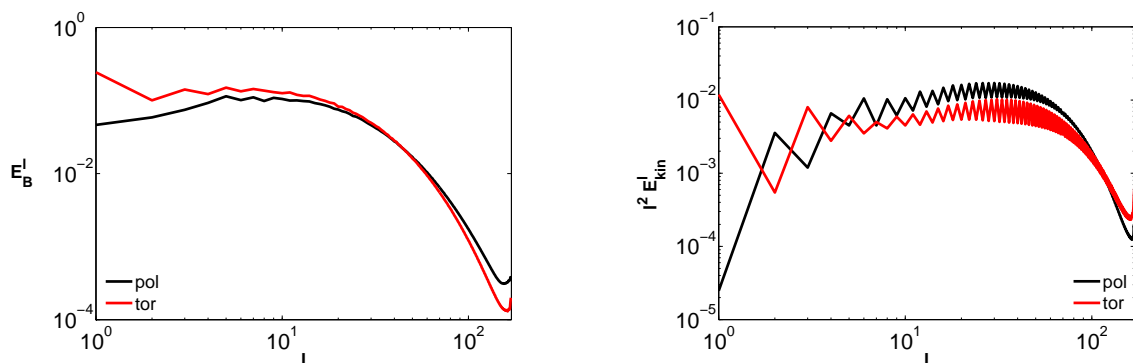


Figure 2.23: Temporally and spatially averaged toroidal (red) and poloidal (black) magnetic (left) and kinetic (right) energy spectra plotted against  $l$  at  $\text{Re} = 970$ .

(Figure 2.21), no such bottleneck can be found.

Another explanation for the bump in the threshold was given by the presence of helicity at the resistive scale by Malyshkin and Boldyrev (2010). In the end, a convincing explanation is still lacking so that this phenomenon is not well understood by now.

For  $\overline{\text{Re}} = 300$  and  $970$ , the magnetic energy spectra are plotted against  $l$  and  $m$  in Figure 2.22. At high  $\text{Re}$ , the magnetic energy is located at large scales and even at  $\overline{\text{Re}} = 970$  the  $l = 1$ -component is dominant. The results seem to be similar to those of Brandenburg (2009), where the magnetic field generation in helical turbulence simulations was investigated. This strongly suggests a large-scale dynamo that is created in the spherical Couette flow by large-scale motions. Only the simulation at the highest  $\overline{\text{Re}} = 970$  raises doubt, because a local maximum emerges at  $l \approx 10$ , which still is within the inertial range of the kinetic energy spectrum (Fig. 2.21). It seems to suggest an acting dynamo at two different scales. In Figure 2.23, the toroidal and poloidal parts of the magnetic and kinetic energy spectra are plotted separately. Apparently, the large-scale toroidal magnetic field is generated by the velocity shear of the boundary layer, which is dominant at  $l = 1$  in the toroidal kinetic energy. The generation of the poloidal magnetic energy occurs at some intermediate scale  $l \approx 10$ . The only significant intermediate scale between the scale of the boundary shear and the viscous scale is the scale of the equatorial jet, where the maximum poloidal magnetic energy is generated. In order to make sure that this dynamo is dominant at large scales, another simulation was performed at  $\overline{\text{Re}} = 970$ , where the mean part of the flow is subtracted from the velocity field before integrating the induction equation. The magnetic energy decreases significantly at  $\text{Pm} = 1$ , as well as the peak at  $l = 1$  in the magnetic energy spectrum. This implies that the large-scale dynamo is dominant and apparently generated by an  $\Omega$ -effect of the boundary layer shear. The turbulent eddies alone are not able to sustain the dynamo. Hence, increasing  $\overline{\text{Re}}$  has no effect on the dynamo threshold, since the dynamo is created within the inertial range and only a turbulent tail is added to the kinetic energy spectrum. With increasing  $\overline{\text{Re}}$ ,  $\text{Pm}$  drops below unity and the magnetic

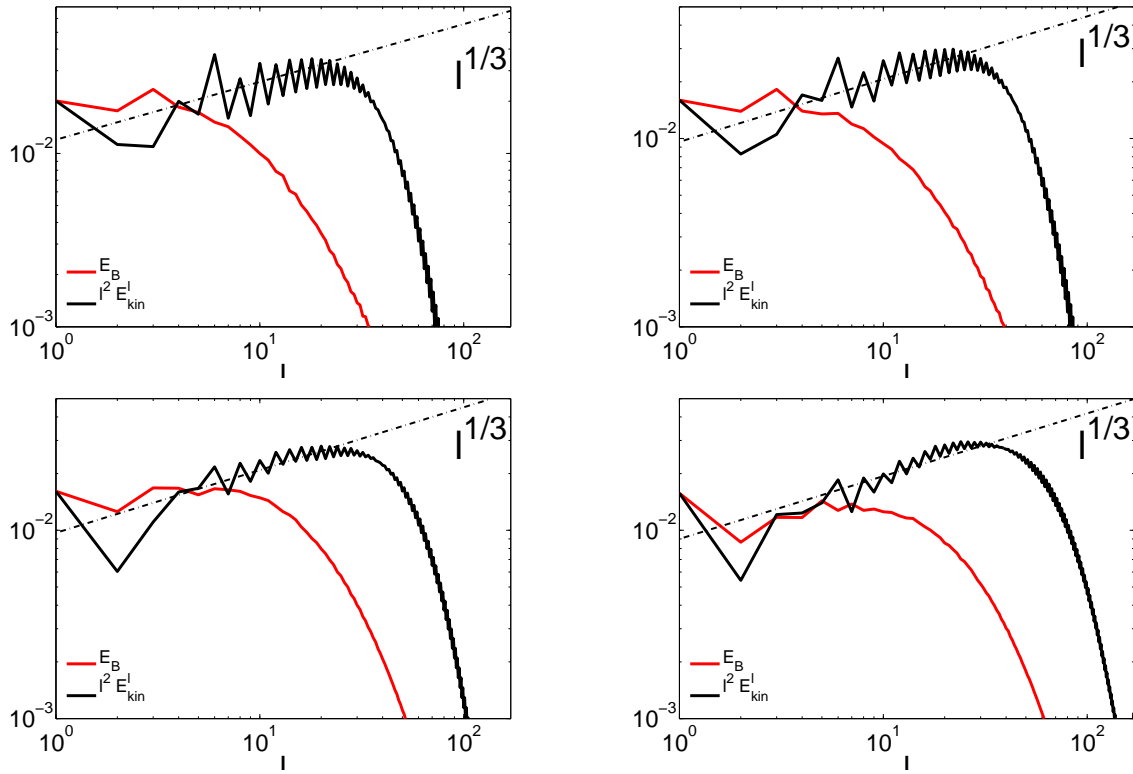


Figure 2.24: Temporally and spatially averaged magnetic energy (red) and turbulent rate of strain (black) spectra at  $\overline{\text{Re}} = 300$  (top left), 400 (top right), 600 (bottom left) and 970 (bottom right).

field is too rough to be affected by the fluid at the viscous scale. Because of the magnetic diffusion, the magnetic field is not influenced by the turbulent eddies of further decreasing scale size. That is why the dynamo threshold is seen to be constant in the limit  $\text{Re} \rightarrow \infty$ . The transition of the dynamo scale from low to high  $\text{Re}$  can be seen in Figure 2.24, where the turbulent rate of strain is plotted over  $l$  together with the magnetic energy spectrum at  $\overline{\text{Re}} = 300, 400, 600$  and 970. At low  $\overline{\text{Re}}$ , the magnetic energy is generated at large scales, where the dynamo is mainly driven by the dominant non-axisymmetric instability. At  $\overline{\text{Re}} = 970$ , finally, the magnetic energy shows these two maxima, which are far within the inertial range.

Based on this finding, the threshold can be extrapolated to the parameter range relevant for experiments. The plateau of the dynamo threshold is at  $\overline{\text{Rm}}_c = 800$ . In all dynamo experiments, the working fluid is liquid sodium with  $\text{Pm} \approx 10^{-5}$  and  $\nu \approx 10^{-6}$ . Based on these numbers, the experimental setup has to reach  $\overline{\text{Re}} = 8 \times 10^7$ . For such high  $\overline{\text{Re}}$ , the kinetic energy is already constant  $E_{kin} \approx 0.023$  and  $v_{rms} \approx 0.058$ , which finally gives  $\text{Re} = 1.4 \times 10^9$ . The corresponding rotation frequency is  $f = \text{Re} \nu / 2\pi d^2 = 223 \text{s}^{-1}$ . In order to get an estimate for the energy dissipation, the data of Figure 2.7 are also extrapolated to that  $\text{Re}$  and one yields  $\tau \approx 1.8 \times 10^{-6}$ . The energy dissipation per unit mass is

$\epsilon \sim \tau \Omega_i^3 d^2 \approx 1.8 \times 10^3 W/kg$ . Within a volume of  $Vol \approx 13m^3$  and a density of liquid sodium with  $\rho \approx 10^3 kg/m^3$ , the total energy dissipation is approximately  $\epsilon \approx 23GW$ , which is a quite unrealistic number owing to very high rotation rates.

The low efficiency of this flow to sustain a dynamo might have two crucial reasons. First, the high rotation rates are needed because the boundary layer, across which the momentum is transferred to the fluid, decreases with the rotation rate. Almost the entire kinetic energy is gained within the boundary layer and only there, large shears occur so that the dynamo is generated in a very small part of the spherical gap. Another important aspect for the efficiency is the ability to generate poloidal and toroidal magnetic field lines likewise, in order to close the dynamo circle. A toroidal magnetic field is generated mainly within the boundary layer, where the field lines are wound up around the inner sphere. The poloidal magnetic field is mainly obtained around the equatorial jet, where the field lines are pushed outwards in radial direction. Equation 2.34 shows that the induction of  $\mathbf{B}$  is proportional to the shear  $B_j \partial_j v_i$ . Assuming that the length scales of the equatorial jet and the boundary layer are of same order of magnitude, the ratio of the shear across the boundary layer to the shear across the equatorial jet is just the ratio of their maximum velocities. This ratio can be taken as a measure for the dynamo efficiency. In this flow, the ratio is approximately 5. In conclusion, the efficiency can be improved by increasing the momentum transfer in the whole volume and a lower ratio of the toroidal to poloidal velocity shear.

### 2.3 Rough surface

The obtained results for a spherical Couette flow driven by a pure viscous coupling between the inner core and the fluid leads to parameters, which cannot be reached by the corresponding experiment in Maryland. Although with smooth boundaries, the inner sphere rotates quite fast ( $f = 223s^{-1}$ ) at the kinematic dynamo onset, the momentum transfer across the boundary layer to the entire volume is very low, so that the averaged  $v_{rms}$  is only one tenth of the boundary velocity.

Therefore, a second numerical setup is investigated, where a volume force is introduced in the Navier-Stokes equation. The force intends to simulate a rough surface, which increases the coupling between the rotating inner sphere and the fluid. Thereby, the fluid is stirred more.

The outline of this section is similar to the previous one. In the first section, the purely hydrodynamic properties of the system are investigated by integrating the Navier-Stokes equation 2.6 in time. The only parameter that is changed is  $Re$ . The shape of the velocity field undergoes two transitions from an axisymmetric field to a state where the first non-axisymmetric instability develops with a dominant azimuthal wave number  $m = 2$ . At high  $Re$ , the flow becomes Kolmogorov-like turbulent. The main focus is on the evolution of the boundary layer thickness, the kinetic energy and the evolution of hydrodynamic instabilities.

In the second section, the evolution of a weak magnetic seed field in this flow is investigated. Therefore, the induction equation 2.5 is integrated additionally. The main focus is on the kinematic dynamo onset in the parameter space of  $Re$  and  $Rm$ . The results are compared with those of the smooth surface simulation with respect to the dynamo effi-

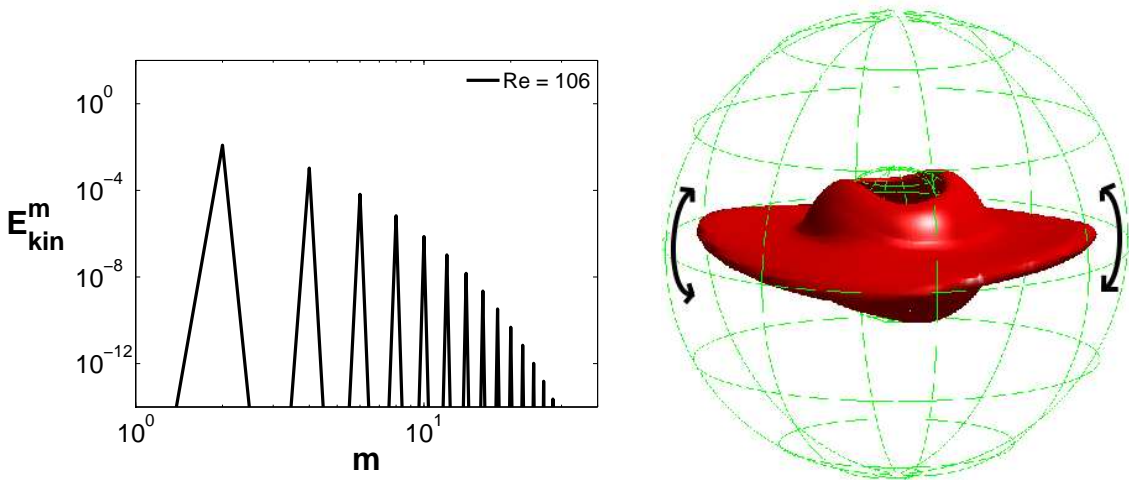


Figure 2.25: Snapshots of the kinetic energy spectrum plotted against  $m$  (left) and isosurface of 20% of the maximum local kinetic energy at  $\overline{Re} = 106$  (right).

ciency of the respective flow and the dynamo mechanism. The results are extrapolated to parameters of the liquid Sodium experiment in Maryland. Finally, a conclusion is drawn, whether a rough surface could be a reasonable improvement of the experiment and what are the reasons therefore.

The parameter  $Re$  is varied from  $10^2$  up to  $2.5 \times 10^3$ , whereas  $Pm$  is again of order unity. Since the boundary layer is expanded to one tenth of the gap width, its thickness is not crucial as a measure for the radial resolution anymore. The resolution is 32 in radial, 128 gridpoints in latitude and 256 in azimuthal direction with dealising at 85 and 170 respectively. At  $Re = 10^3$ , the driving force is already generating large averaged velocities  $\overline{v_{rms}}$ , so that the resolution has to be 64 in radial, 256 gridpoints in latitude and 512 in azimuthal direction with dealising at 170 and 340 respectively.

### 2.3.1 Hydrodynamic properties

The basic shape of the velocity field is similar to that created by no-slip boundary conditions. The driving force generates a boundary layer, in which the velocity is accelerated in  $\phi$ -direction and flows outwards in an equatorial jet to the outer sphere. Within the entire rest of the volume, it recirculates back again to the inner sphere and the equatorial jet. The main difference is a thicker boundary layer, which is independent on  $Re$ , as it was wanted. Thereby, the momentum transfer into the entire spherical shell is increased. Hence, the equatorial jet is much larger compared to the size in the first simulations. At low  $Re$ , the flow is axisymmetric and destabilizes at comparatively low values  $Re_h = 425$  ( $\overline{Re}_h = 95$ ). The stronger driving force generates higher velocities so that non-linear inertial forces become dominant.

At that point, small non-axisymmetric perturbations develop as a propagating wave on the equatorial jet with a dominant wave number  $m = 2$ . Only amplitudes of even wave

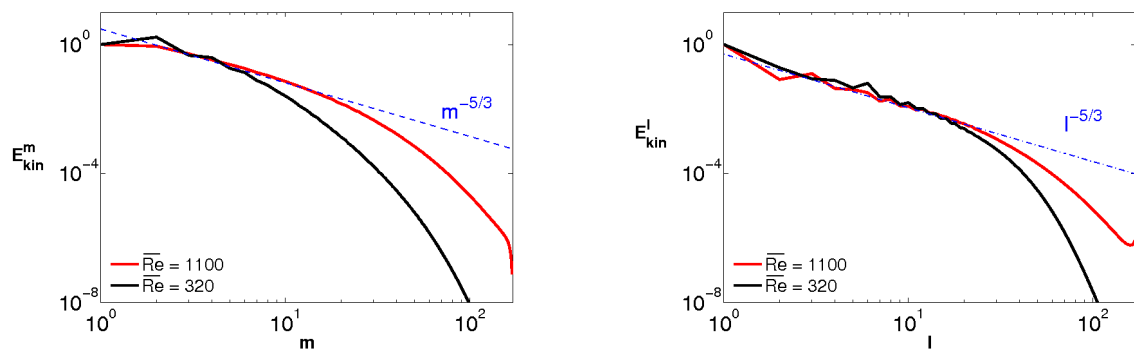


Figure 2.26: Temporally and spatially averaged kinetic energy spectrum plotted against  $m$  (left) and  $l$  (right) at  $\overline{Re} = 320$  (black) and 1100 (red).

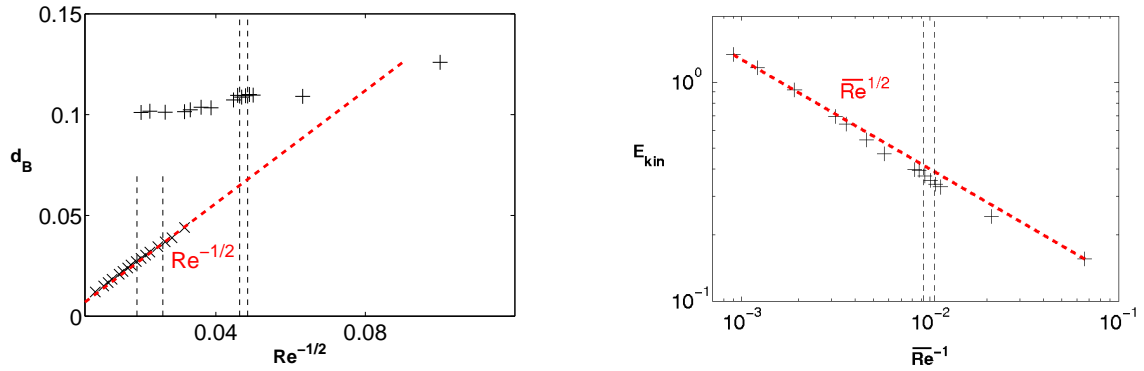


Figure 2.27: Boundary layer thickness of the volume force + and the no-slip  $\times$  simulations plotted against  $Re^{-1/2}$  (left). Kinetic energy plotted against  $\overline{Re}^{-1}$  (right). The red dashed lines represent the respective power laws of  $Re^{-1/2}$  (left) and  $\overline{Re}^{1/2}$  (right)

numbers are excited so that kinetic energy in harmonics of  $m = 2$  is gained and in odd wave numbers it dissipates. Figure 2.25 shows the kinetic energy spectrum over spherical harmonic degree  $m$  (left) and a snapshot of the isosurface of 20% of the maximum local kinetic energy (right) at  $\overline{Re} = 106$ . Compared to the no-slip simulation, the contribution of the boundary layer and the equatorial jet to the total kinetic energy is ten times less. Thus, in this case, the kinetic energy is distributed more equally within the entire volume. At  $Re_s = 465$  ( $\overline{Re}_s = 108$ ), only slightly higher than  $Re_h$ , amplitudes of odd wave numbers increase in time as well. The kinetic energy spectrum becomes increasingly smooth and approaches power laws in  $m^{-5/3}$  and  $l^{-5/3}$ , which implies Kolmogorov-like turbulence. In Figure 2.26, the kinetic energy spectra are plotted against  $m$  and  $l$  at  $\overline{Re} = 320$  and 1100. Since the inner boundary velocity increases with  $Re$ , the spectra are normalised with respect to the amplitude of the  $m = 1$ -mode. In this way the spectra can be better compared. In Figure 2.27, the evolution of the boundary layer thickness is plotted against  $Re^{-1/2}$  and

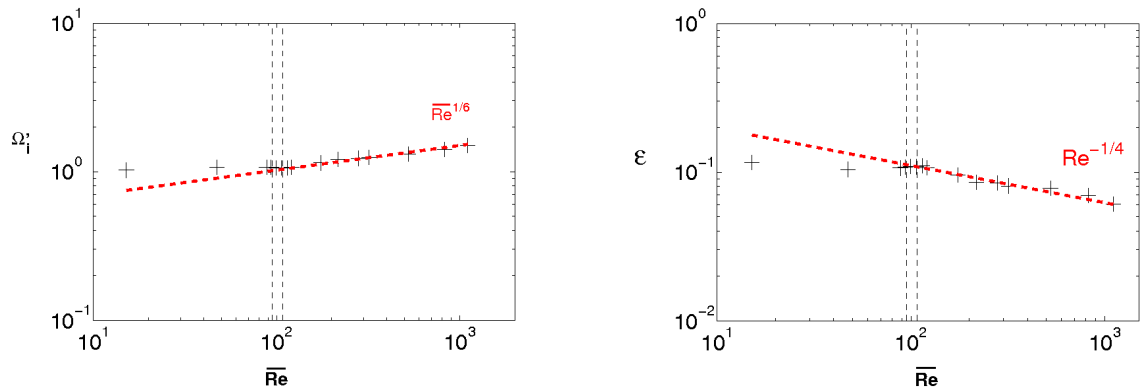


Figure 2.28: Inner sphere's rotation rate  $\Omega_i$  (left) and energy dissipation  $\epsilon$  plotted against  $\overline{Re}$ . The red dashed lines show the respective proportionalities of  $\overline{Re}^{1/6}$  and  $\overline{Re}^{-1/4}$

compared with the results of the no-slip simulations. As it is expected, the boundary layer thickness does not drop below the defined roughness size of one tenth of the gap width, which is much larger than in the other set of simulations. The consequence is that the kinetic energy, which is plotted in Figure 2.27, is about one to two orders of magnitude larger than in the smooth surface simulation (Fig. 2.6). In the simulated range, it increases with  $\text{Re}^{1/2}$  and is far away from saturating, as it should for large  $\text{Re}$ . In all figures the vertical dashed lines denote the transitions  $\text{Re}_h$  and  $\text{Re}_s$ .

In the left panel of Figure 2.28, the inner sphere's rotation rate  $\Omega'_i$  is plotted against  $\overline{\text{Re}}$ . The developing of the values is non-monotonous and shows a powerlaw only for  $\text{Re} > \text{Re}_s$  of  $\text{Re}^{1/6}$ . Although its increase is quite low, the exponent is important for the extrapolation to experimental parameter regimes. Compared to the powerlaw of the kinetic energy, it becomes clear that these two exponents are not reasonable for  $\overline{\text{Re}} \rightarrow \infty$ . In this limit the spatially averaged velocity would exceed the driving velocity. The ratio of  $v_{rms}/(r_i\Omega'_i)$  gives a measure for the validity of the extrapolated result. At  $\overline{\text{Re}} \approx 10^6$ , the ratio becomes one. Slightly below this value, the kinetic energy is supposed to reach the saturated state and become constant. The right panel shows the energy dissipation, which is computed from the integral  $\Omega'_i{}^{-3} \int \mathbf{F} \cdot \mathbf{v} dV$ , is plotted against  $\overline{\text{Re}}$ . The evolution is not quite well understood since it decreases but not that fast. The best fit is denoted by the red dashed line and shows a development proportional to  $\overline{\text{Re}}^{-1/4}$ .

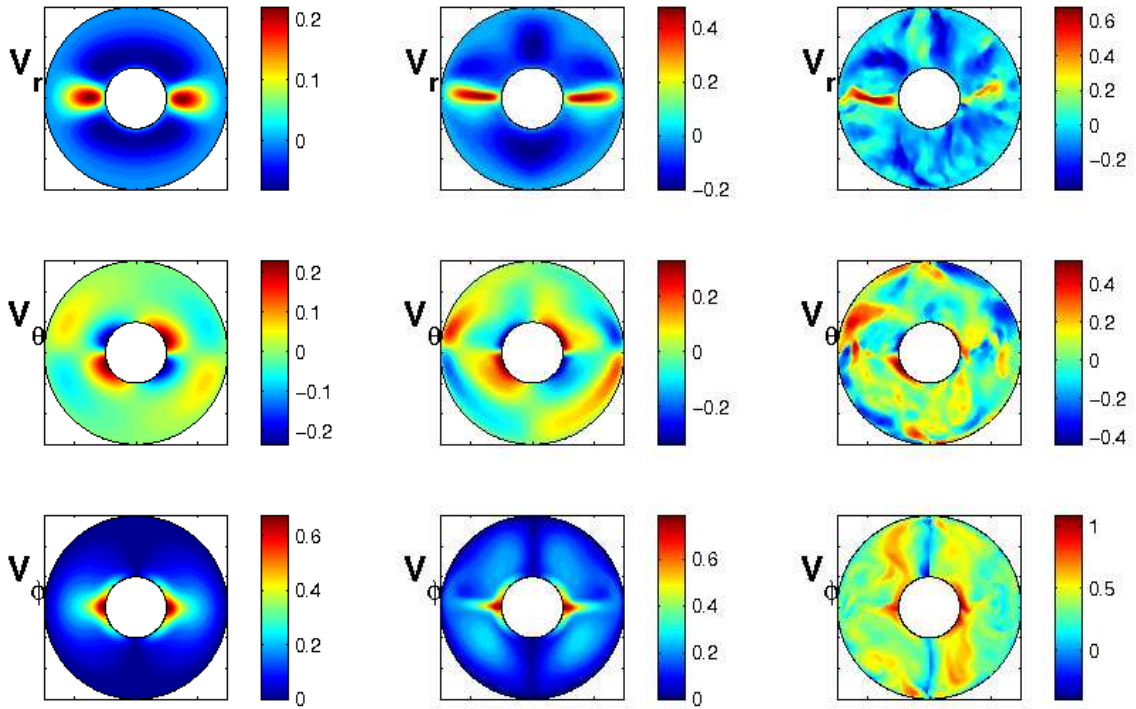


Figure 2.29: Snapshots of the three components  $r$  (top),  $\theta$  (middle) and  $\phi$  (bottom) of velocity field at  $\text{Re} = 10^2$  (left),  $4.5 \times 10^2$  (middle) and  $2.5 \times 10^3$  (right).

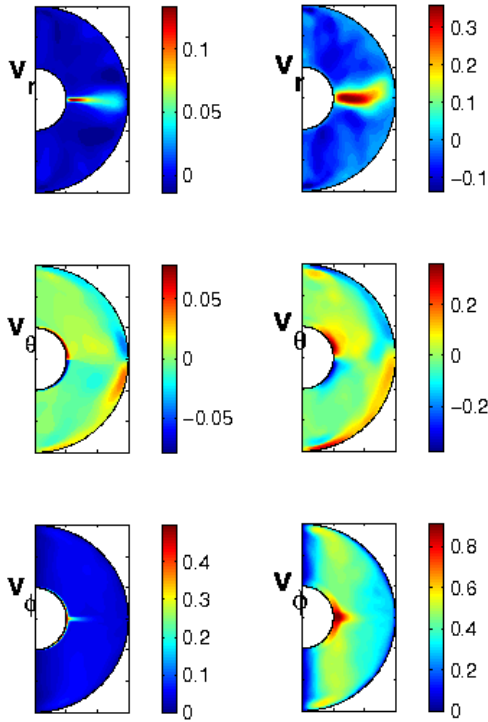


Figure 2.30: Temporally and zonally averaged components of the radial (top), meridional (middle) and azimuthal (bottom) component of the velocity field with smooth (left) and rough boundaries (right).

Acting on the assumption that turbulence has emerged so far that it is Kolmogorov-like, the energy dissipation rate should evolve like  $\epsilon \sim (v_0/\Omega_i d)$ . The velocity of the energy carrying vortex is denoted by  $v_0$  and represents the vortex of the driving force and should be proportional to  $\Omega_i d$ . Thus, the energy dissipation should be constant. The shape of the velocity field is shown as snapshots in Figure 2.29 for the three different states: Axisymmetric (left), first non-axisymmetric instability (middle), turbulent state (right). At low  $Re$ , on the left side, the shape is axisymmetric. The radial component (top panel) shows the equatorial jet, which is comparably thick to that one of the smooth surface simulations. The boundary layer, which can be seen in  $B_\theta$  (central panel) and  $B_\phi$  (bottom panel), has increased as well. As it was already mentioned, the  $\phi$ -velocity at the inner boundary is not equal to 0.5 anymore so that  $\Omega_i$  cannot be seen as the time scaling quantity anymore. Due to the change of the boundary force the ratio of toroidal to poloidal kinetic energy has changed. The maximal radial velocity is only one third of the maximum value of the  $\phi$ -component, as well as the  $\theta$ -component. In the short range of  $Re_h < Re < Re_s$  the non-axisymmetric instability can be observed as a propagating wave with azimuthal wave number  $m = 2$  (middle plot). The equatorial jet is bent up- and downward due to the instability. Compared to the snapshots of the smooth surface simulations, it can already be seen in the  $\phi$ -component that the momentum transfer due to the force term increases the velocity amplitude in the entire volume. Finally at the highest  $Re$ , the regularity of the flow is completely broken and the velocity field is getting increasingly small-scale. Compared to the smooth surface simulations,  $v_\phi$  has significant values, almost all over the entire volume.

These differences at high  $\overline{Re}$  become more obvious in Figure 2.30, where the temporally and zonally averaged components of the velocity field of a smooth surface simulation at  $\overline{Re} = 970$  and of a rough surface simulation at  $\overline{Re} = 1100$  are shown. The radial component in the latter case shows a much stronger jet, which is as already mentioned due to

the increased momentum transfer and therewith a higher mass transport. This is related to the thickness of the boundary layer of  $v_\theta$  and  $v_\phi$  at the inner core. Due to an extension of the driving force to one tenth of the gap width, the boundary layer is much thicker and the momenta are better transferred in the entire volume. The velocity component  $v_\phi$  has significant values all over the spherical gap contrary to the smooth surface simulations, where the  $\phi$ -component is large only close to the inner sphere. Apart from that, the ratio of poloidal to toroidal shear is decreased by about a factor of 2.

In Figure 2.31, isosurfaces of 10% of the maximum local helicity are plotted. Compared to the smooth surface simulations (Fig. 2.8), the helicity has also significant values apart from regions near the inner sphere. The maximum and minimum helicity is increased by a factor of 4. Thus, the efficiency of the flow to dynamo action is enhanced as well.

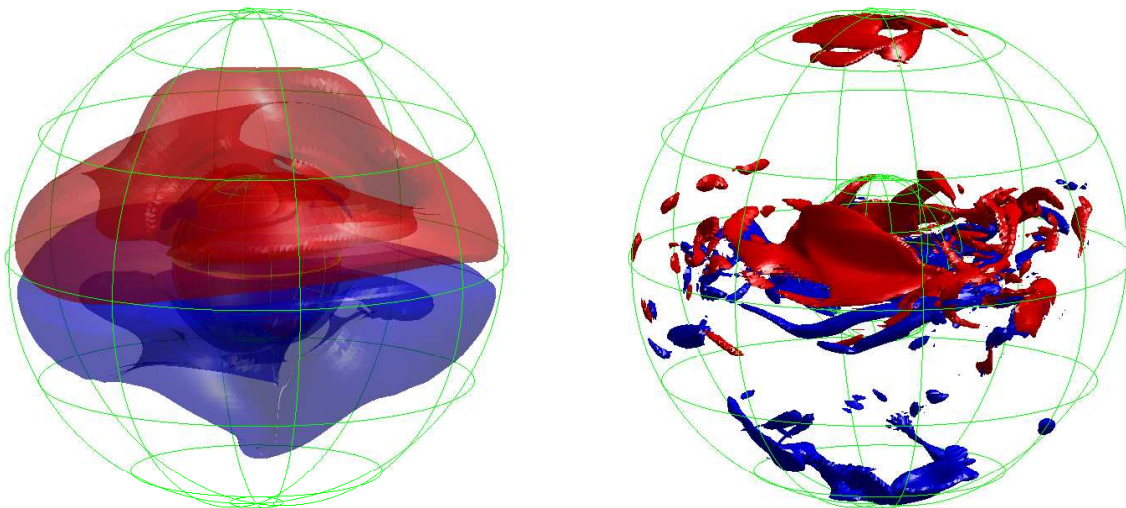


Figure 2.31: Snapshots of the isosurface of 10% of the maximum kinetic helicity at  $Re = 106$  (left) and  $1100$  (right). Blue indicates negative helicity and red positive. The respective maximum and minimum values are  $(\pm 1.58)$  and  $(-45.57/37.17)$

### 2.3.2 Kinematic dynamo threshold

In the following, the results of the simulations integrating the full MHD equations are presented. The focus is on the kinematic dynamo onset and the dynamo mechanism in comparison with the results of the previous section. Figure 2.32 shows the dynamo results of the simulations in the  $(\overline{Re}, \overline{Rm})$ -plane and in the  $(\overline{Re}, Pm)$ -plane. The dynamo onset is indicated by the dashed thick black line. The development of  $\overline{Rm}_c$  is quite similar to the no-slip simulations. In axisymmetric flows, no dynamo could be found for values of  $Pm < 10$ . This implies, that the generation of magnetic field lines at low  $Re$  is closely related to the occurrence of non-axisymmetric instabilities. Nevertheless, slightly above this onset at  $\overline{Re}_h < \overline{Re} < 100$ , no dynamo up to  $Pm = 9$  could be found either. The reason for that might be related to the phase velocity of the propagating wave on the equatorial jet. Since the focus is on the turbulent regime in this section, an according investigation with frozen flux simulations was omitted. But, as it was shown in Figure 2.14, the dependence of the growth rate on the phase velocity is not monotonous and quite unpredictable and at this particular phase velocity the dynamo might be very inefficient.

At  $\overline{Re} > 100$ , amplitudes in even wave numbers  $m$  of the magnetic energy spectrum increase and the symmetry of the magnetic field becomes similar to that of the velocity field with a dominant azimuthal  $m = 2$ -periodicity. In the left panel of Figure 2.33, the kinetic

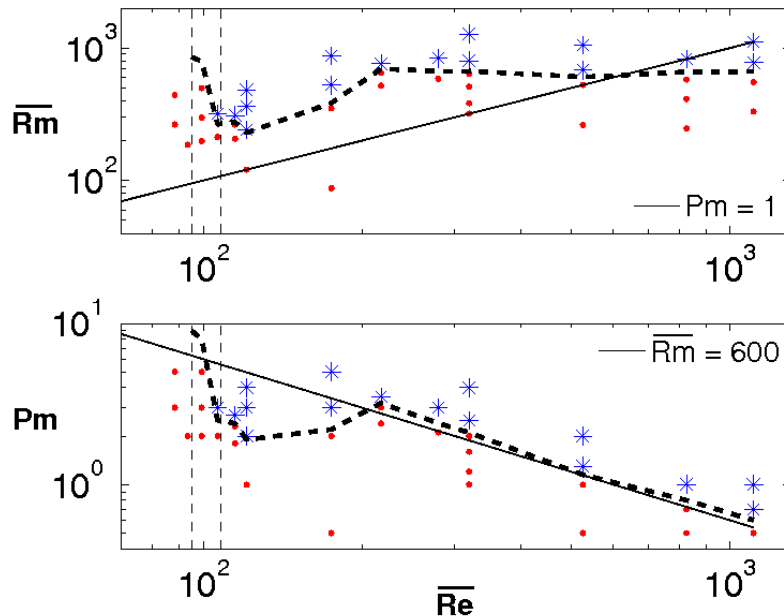


Figure 2.32: Dynamo onset in the  $(\overline{Re}, \overline{Rm})$ -plane (top) and in the  $(\overline{Re}, Pm)$ -plane (bottom). Failed dynamos are indicated red and working dynamos blue. The thick dashed line marks  $\overline{Rm}_c$  and the vertical dashed lines denote the transitions  $\overline{Re}_h$  and  $\overline{Re}_s$ . The straight lines are  $Pm = 1$  (top) and  $\overline{Rm} = 600$  (bottom).

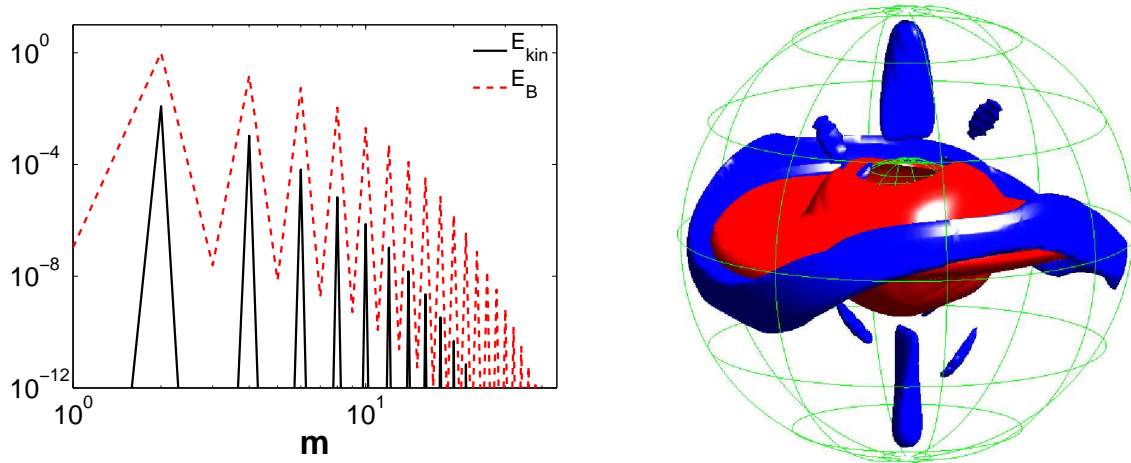


Figure 2.33: Snapshots of the magnetic (red) and kinetic (black) energy spectrum (left) and isosurfaces of 20% of the total kinetic energy (red) and 20% of the total magnetic energy (blue) (right) at  $\overline{\text{Re}} = 106$ .

and magnetic energy spectrum is plotted against  $m$ . In the right panel, isosurfaces of 20% of the maximum local kinetic energy and 20% of the maximum local magnetic energy are shown. This plot emphasizes the close relation of magnetic field generation to the propagating instability, because magnetic energy is mainly located at the equatorial jet. There, the magnetic field exhibits a strong toroidal component.

The phase velocity of the propagating wave decreases with increasing  $\overline{\text{Re}}$  like in the no-slip case. Nevertheless it is not surprising that in this case,  $\overline{\text{Rm}}_c$  decreases with increasing  $\overline{\text{Re}}$  contrary to the observations in the no-slip simulations. Since, as it was shown in Figure 2.14 (left), the growth rate behaves non-monotonously against the phase velocity. Obviously, no general conclusion can be drawn from the relation of the phase velocity to the dynamo efficiency of the flow. The case of growing amplitudes in odd modes of the magnetic energy spectrum (Fig. 2.13 does not appear. The state, where only amplitudes of even wave numbers and higher harmonics are excited, appears in a very short range of  $\text{Re}$ . The driving force creates high velocities so that inertial forces destabilize the equatorial jet already at low  $\text{Re}$ .

At  $\overline{\text{Re}} > \overline{\text{Re}}_s$ , all modes of the kinetic energy spectrum are excited. The velocity field is increasingly fluctuating in time and  $\overline{\text{Rm}}_c$  increases with  $\overline{\text{Re}}$ . According to the smooth surface simulations (Fig. 2.19), the temporal fluctuations have a destructive effect on the dynamo.

At  $\overline{\text{Re}} = 320$ , the  $m = 2$ -mode is still the dominant mode. Therefore, it is quite interesting, why the threshold suddenly kinks and remains at a constant  $\overline{\text{Rm}} = 600$  for  $\overline{\text{Re}} > 220$ . Obviously, at a certain point, the raising amplitudes of the small-scale velocity field fluctuations have no effect on the dynamo quality anymore. In Figure 2.34, four temporally and spatially averaged spectra of the turbulent rate of strain and the magnetic energy are

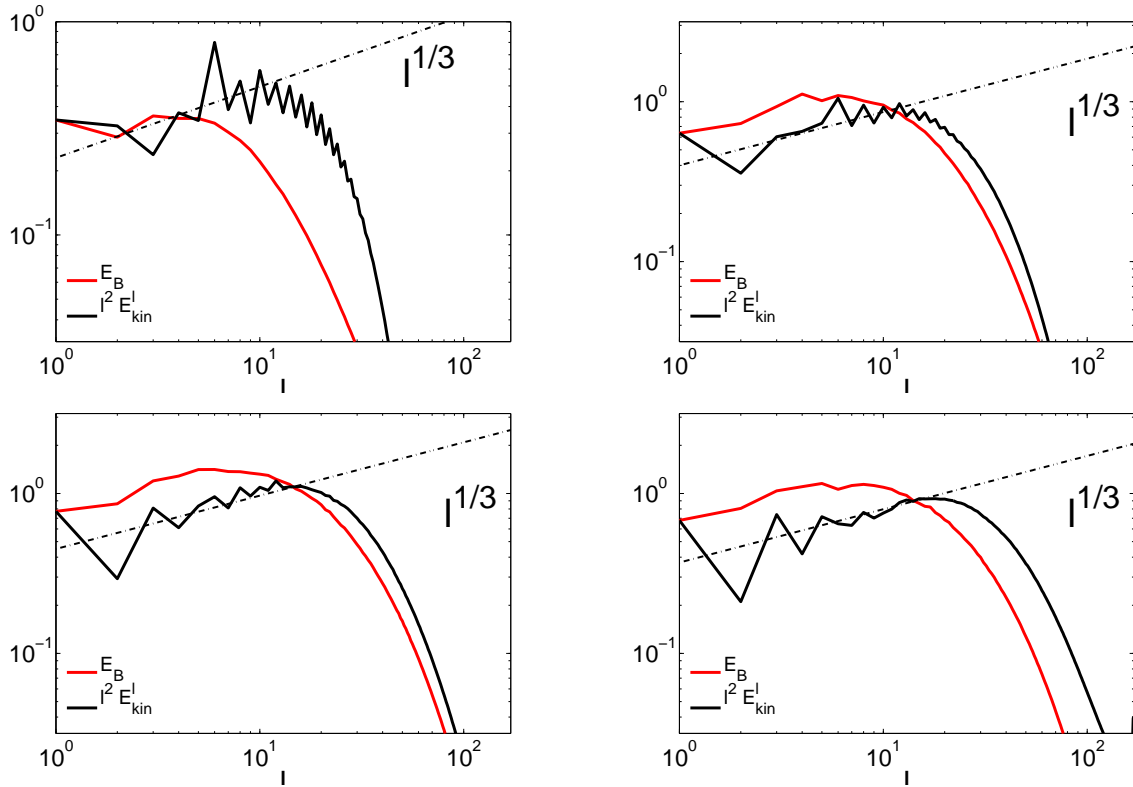


Figure 2.34: Temporally and spatially averaged turbulent rate of strain (black) and magnetic energy spectra (red) plotted against  $l$  at  $\overline{\text{Re}} = 218$  (top left), 525 (top right), 825 (bottom left) and 1100 (bottom right).

plotted against  $l$  for  $\overline{\text{Re}} = 218, 525, 825$  and 1100. The spectra show that the peak of  $l^2 E_{kin}$ , which marks the viscous dissipation scale, is shifted to smaller  $l$ , as it is expected. At  $\overline{\text{Re}} = 218$ , the generation of magnetic field lines takes places predominantly at large scales, like it is the case at smaller  $\overline{\text{Re}}$ . There, the dominant mode is still  $m = 2$  and drives the dynamo. At  $\overline{\text{Re}} = 320$ , the scales where the dynamo is mainly generated decrease and the dynamo mechanism seems to change. The peak of the magnetic energy spectrum shifts to smaller wave numbers, which suggests a small-scale dynamo. This has already been discussed in helical forced turbulence by Brandenburg (2009), Brandenburg and Nordlund (2011). There, dynamos occur somewhere between a small and large-scale dynamo but shifts to large scales as  $\text{Pm}$  decreases.

In the smooth surface simulations, the dynamo acts on large scales due to the boundary shear layer and on a second intermediate scale, which is associated with the scale of the equatorial jet. In the rough surface simulation, no such large scale in the magnetic energy spectra can be identified, since the shear at the boundary layer is not distinct anymore. Nevertheless, a scale of the equatorial jet and the boundary layer can be obtained from the temporally and zonally averaged velocity field (Fig. 2.30). This can also be seen in Figure 2.35, where the magnetic and kinetic energy spectra are splitted into toroidal and

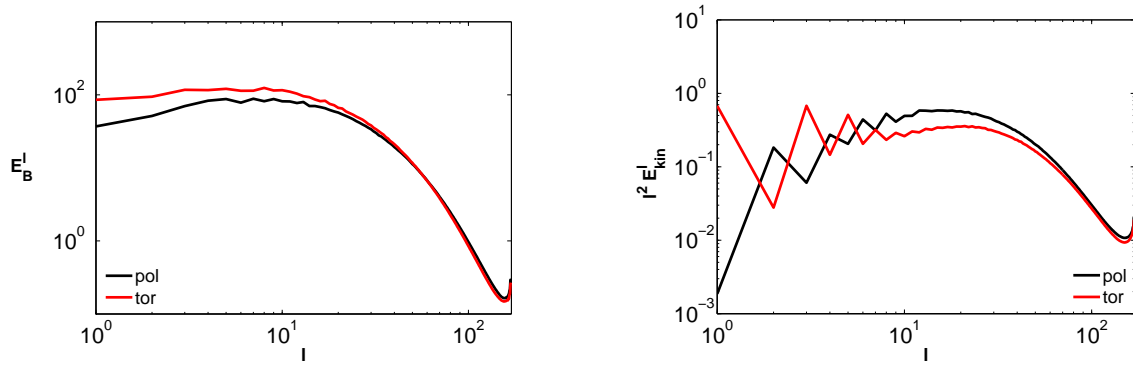


Figure 2.35: Toroidal (red) and poloidal (black) magnetic (left) and kinetic (right) energy spectra plotted against  $l$  at  $\overline{\text{Re}} = 970$ .

poloidal parts. Obviously, the magnetic energy spectra show no small-scale dynamo, so that the maximum in the spectra can be associated with an intermediate scale dynamo as well.

At  $\overline{\text{Re}} = 1100$ , the resistive scale is already within the inertial range, since  $\text{Pm} = 0.7$ . There, the intermediate scale of the equatorial jet is of similar order than the viscous scale and the small-scale dynamo becomes the dominant magnetic energy generating mechanism. Nevertheless, it has to be pointed out that a clear scale separation is not obvious in the spectra, which complicates the interpretation. Therefore, additional simulations were made in which the mean flow was subtracted from the velocity field in the induction equation. In these simulations acting dynamos suddenly shut down, which indicates that a large-scale mean flow is still necessary to generate the dynamo and that the turbulent eddies are not able to sustain it alone.

Although the shape of the boundary shear is smeared over the driving range compared to the sharply sheared boundary layer of the smooth simulation, the dynamo mechanism can be seen as similar, since the basic topology of the flow is the same. Therefore, the maximum in the spectra of the magnetic energy must be due to a scale, which is comparable to that of the equatorial jet, which is definitely larger than the viscous scale and the dynamo is not a small-scale dynamo but a dynamo at an intermediate scale. Obviously, the resistive scale and the intermediate scale are also not separated sufficiently. The dynamo threshold, therefore, is seen constant for even higher  $\overline{\text{Re}}$ . The turbulent tail of the kinetic energy spectrum just elongates and the generation of magnetic energy occurs further on within the inertial range.

In this dynamo threshold, the bump, which is supposed to appear at  $\text{Pm} \approx 1$ , cannot be observed as well as in the work of Brandenburg and Nordlund (2011). The reason for that could be, on the one hand, that there is no bottleneck visible in the kinetic energy spectra or, on the other hand, it appears at lower  $\text{Pm}$ . The region of  $0.06 \lesssim \text{Pm} \lesssim 0.2$ , where it was found by Ponty et al. (2005, 2007) in the dynamo threshold, could not be reached in

the simulations either.

In Figure 2.36, the threshold of both sets of simulations are plotted against  $Re$  and  $Rm$  together with the results of Guervilly and Cardin (2010). Comparing the two different surface types of this chapter gives a significant difference in the range of  $Re$ , where the two flows are completely destabilised. This leads to essentially different ranges of rotation rates. The results of the smooth surface simulation shows compared to the results of Guervilly and Cardin (2010) a quite similar development, accounting for the fact that, there, the non-linear equations including the Lorentz force are solved. Due to the Lorentz force the wave-like motion at  $Re_h < Re < Re_s$  cannot evolve unaffected as in the kinematic case. At high  $Re$ , where the dynamo threshold kinks to the plateau, it is not clear whether the other curve would do so as well, if  $Re$  was increased a little bit further.

The extrapolation of the numerical results to the parameter regime relevant for the liquid sodium experiment in Maryland has to be regarded carefully. First, the kinetic energy increases with  $\overline{Re}^{1/2}$ . Only a saturated state could give a certain result in the limit  $\overline{Re} \rightarrow \infty$ . It is not clear, up to which  $\overline{Re}$  this exponent would be correct. Secondly, the time scaling  $\Omega_i$  is not equal to one, as it is shown in Figure 2.29 and depends on  $Re$  (see fig. 2.28). The respective power laws for  $v_{rms}$  and  $\Omega_i$  are inconsistent for  $\overline{Re} \rightarrow \infty$ . Hence, the ratio of  $v_{rms}/(r_i\Omega_i)$  has to be seen as a measure of the saturation state and must be smaller than one.

Based on the obtained power laws, the dynamo threshold at  $\overline{Rm}_c = 600$  with  $Pm = 10^{-5}$  (liquid sodium) gives  $\overline{Re} = 6 \times 10^7$  for the experiment. The extrapolation of the kinetic energy up to this value yields  $E_{kin} \approx 300$  and  $v_{rms} \approx 6.6$ . The temporally averaged boundary

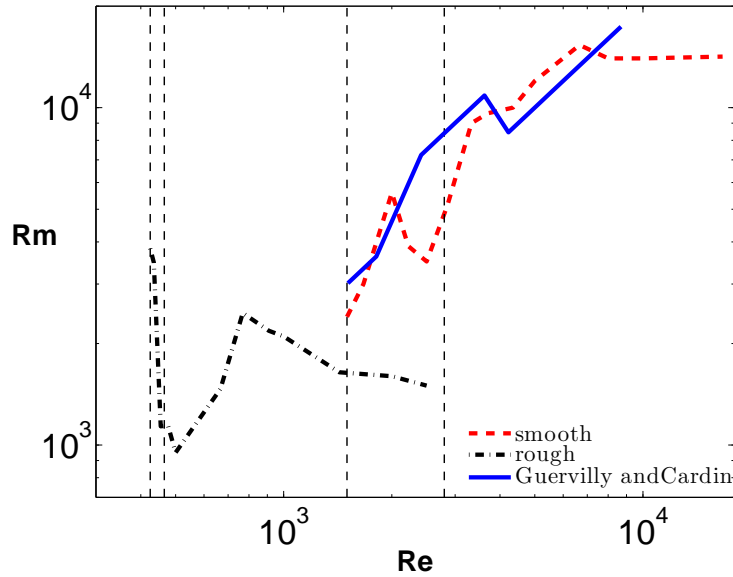


Figure 2.36: Kinematic dynamo onset with smooth and rough boundaries and the results of Guervilly and Cardin (2010). Vertical dashed lines denote the transitions  $Re_h$  and  $Re_s$

rotation rate is  $\Omega'_i \approx 9$  and  $\text{Re}' \approx 9 \times 10^7$  gives finally a frequency of about  $f \approx 14\text{s}^{-1}$ . The ratio of averaged to boundary velocity, however, yields  $v_{rms}/(r_i\Omega_i) \approx 1.4$  so that this result has no validity. With  $\Omega'_i \approx 9$ , the kinetic energy can be at least  $E_{kin} \approx 140$ . This represents the case, that except for a thin boundary layer at the outer sphere, the fluid velocity within the entire volume is almost equal to the boundary velocity. This gives  $\text{Re}' \approx 1.2 \times 10^8$  with a rotation rate of  $f \approx 19\text{s}^{-1}$  and can be seen as lower limit. The experiment is able to spin the inner sphere with a rotation frequency of  $15\text{s}^{-1}$ . Even though the obtained result is some kind of a lower limit, in this configuration no dynamo can occur.

## 2.4 Conclusion

In this part, two different surface types were applied to drive the non-rotating spherical Couette system in order to investigate the capability of their flows to generate a dynamo. So far, dynamo experiments in spherical geometry failed to sustain a dynamo and recent results of numerical simulations by Guervilly and Cardin (2010) found that the conditions to sustain a dynamo cannot be achieved by spherical Couette flow in experiments. Therefore, another driving mechanism, which intend to simulate a rough surface, was investigated. By means of this, the efficiency of the flow to dynamo action shall be increased. Based on the results, the spherical Couette experiments like that one in Maryland needs to be improved in such a way that it might be a capable to sustain a dynamo.

The parameter range of  $Re$  can be divided into three regions in which the characteristic of the velocity field changes significantly. At low  $Re$ , the flow is axisymmetric where no dynamo occurs at moderate  $Rm$ . At a critical  $Re_h$ , small perturbations develop and a non-axisymmetric instability with a dominant azimuthal wave number  $m = 2$  occurs as a propagating wave on the equatorial jet. The azimuthal wave number remains the same in this range  $\overline{Re}_h < \overline{Re} < \overline{Re}_s$  and only the boundary layer thickness and the phase velocity of the drifting wave changes slightly. Within this range of  $Re$ , the symmetry of the magnetic field changes significantly and the dynamo threshold decreases abruptly. The first increase of  $Rm_c$  could be found in the decreasing phase velocity of the propagating instability. The reason for sudden change in the symmetry of the magnetic field could only be narrowed down. It seems to be triggered by the time dependence of the velocity field, which could not be captured by the frozen flux simulations since the actual field is a superposition of the dominant mode and higher harmonics. Obviously, the change in the efficiency of the flow to create a dynamo is directly related to the breaking of the symmetry of the magnetic field. This could be confirmed by simulations where the dominant azimuthal wave number is  $m = 3$  and every third higher  $m$  are gained as well. Here the symmetry of  $\mathbf{B}$  is always the same as  $\mathbf{v}$  so that  $Rm_c$  increases monotonously. Still, the reason why the configuration with a broken symmetry of  $\mathbf{B}$  is more efficient to dynamo action, remains unclear.

In the third region, at  $Re > Re_s$ , the regularity of  $\mathbf{v}$  is entirely broken and at high  $Re$ , it becomes Kolmogorov-like turbulent. The dynamo threshold shows a plateau at  $\overline{Rm}_c \approx 800$ , which remains constant at high  $Re$ . Since the dynamo is sustained at large scales, a further increase of  $Re$  only elongates the turbulent tail of the spectra and has no effect on the dynamo. Surprisingly, these results resemble those of Guervilly and Cardin (2010), but only up to the  $Re$  where the threshold kinks to the plateau. One trivial reason could be that  $Re$  has not been increased sufficiently to see this plateau. Nevertheless, the extrapolation to relevant values of the dynamo experiment in Maryland yields rotation rates of

$f \approx 223s^{-1}$ , which is an unreachable number. Apparently, the main problem is the lack of momentum transfer from the boundary layer to the fluid. The inner sphere has to rotate very fast, since the energy is not transferred efficiently in the entire volume. Another problem is that the high ratio of toroidal to poloidal velocity shear. The magnetic field is only sheared significantly within a small layer near the inner boundary and near the equatorial jet and the dynamo circle is not closed uniformly.

Including a driving force in the Navier-Stokes equation, the system intends to simulate the spherical Couette flow with a rough surface, which limits the boundary layer of the flow to a thickness of one tenth of the gap width. In this way, the ratio of toroidal to poloidal shear of the flow is reduced and the momentum transfer from the boundary layer to the whole gap is increased. From this it follows that the kinetic helicity is increased as well and is not located near the boundary layer only. The kinematic dynamo onset of the system shows the same qualitative distinction into three regions as the result of the smooth surface simulations: An axisymmetric flow, the destabilisation of the equatorial jet at a comparatively low Re with the same dominant azimuthal wave number  $m = 2$  and finally at high Re Kolmogorov-like turbulence where  $\overline{\text{Rm}}_c \approx 600$  remains also constant. This value is lowered by one fourth so that the flow can be regarded as more efficient which is found to be due to the better ratio of toroidal to poloidal shear. The dynamo is generated at scales larger than the viscous scale and therefore independent on Re. Coming from this  $\overline{\text{Rm}}_c$ , a lower limit of the rotation rate of the experiment in Maryland is evaluated to be  $f \approx 19s^{-1}$ , which unfortunately is still beyond the experiment's possibilities (Rieutord et al. 2012). The dynamo threshold has to be lowered to  $\overline{\text{Rm}}_c \approx 320$  in order to get a lower limit of  $f \approx 15s^{-1}$ . For this purpose, the ratio of poloidal to toroidal could be improved by taking an additional poloidal forcing term in order to find the optimal efficiency of the flow to dynamo action <sup>2</sup>. With  $\overline{\text{Re}} \approx 3.4 \times 10^7$ , however, this is still far above where the kinetic energy is supposed to saturate which would be still another uncertainty.

---

<sup>2</sup>Private communications with Dr. Emmanuel Dormy



### **3 Magnetic field saturation in a rotating G. O. Roberts like driven flow**

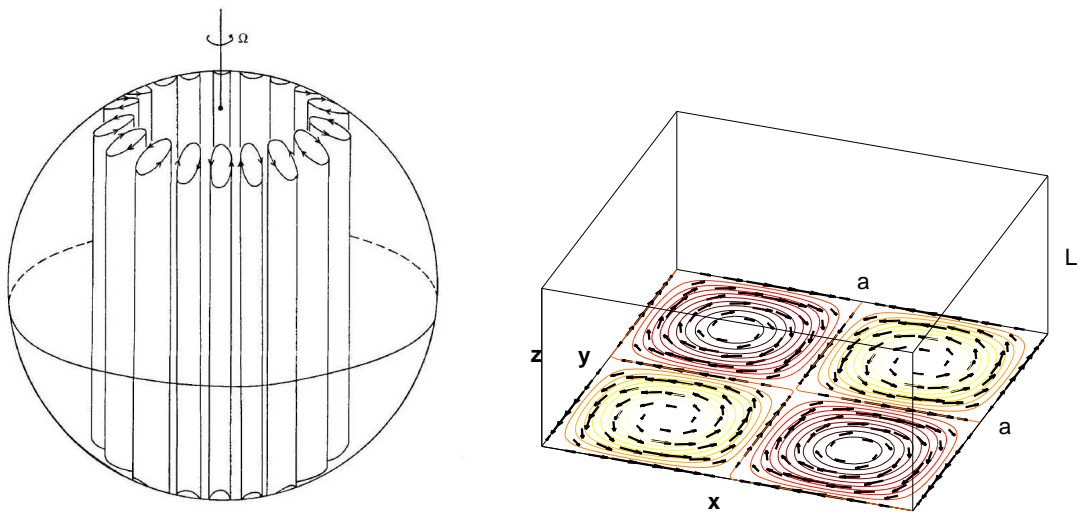


Figure 3.1: Left: Sketch of a convective driven flow structure in a fast rotating spherical shell which forms a vortex columnar structure, so-called Busse-Columns (by Busse (1975)). Right: G. O. Roberts flow in a periodic box of width  $a$  and height  $L$ . The flow in the  $x, y$ -plane is indicated by arrows and the  $z$ -component by the underlying contour plot. Red denotes up and yellow down streaming flow (Roberts 1972).

Most of the celestial bodies like stars or planets, which sustain a magnetic field by dynamo action are rotating very fast so that Coriolis forces dominates over diffusion effects. Additionally, in some objects, the flow is driven by convection due to high temperature gradients from the inner core to the outer boundary. In such systems the velocity field has a specific shape, which is nearly independent with respect to the axis of rotation due to the Taylor-Proudman theorem (Greenspan 1968) and are supposed to form a series of vortex tubes with alternating up and down flows, which are parallel aligned with respect to the axis of rotation. Those vortex tubes which are shown schematically in the left panel of Figure 3.1 are known as Busse columns (Busse 1975). and are favourable to dynamo action due to their helical structure. It is believed that the flow structure in such celestial bodies is quite similar.

The magnetic field that is generated in many stars can have a detectable dipolar component (Morin et al. 2008). The relation between magnetic fields of convection-driven stars and their rotation rate has already been investigated by Mangeney and Praderie (1984), Noyes et al. (1984), Pizzolato et al. (2003). Furthermore, it has been found that in slowly rotating low-mass stars (M-type dwarfs) the surface magnetic field increases with the rotation rate and at a certain rotation rate, the surface magnetic field becomes independent of the rotation rate (Reiners et al. 2009). The dependence of the magnetic field in rotating systems on the rotation rate has also been investigated numerically in spherical geometry by Christensen and Aubert (2006), Schrunner et al. (2012) and in rotating plane layer convection by Tilgner (2012). However, no consistent dependence of the magnetic energy on

the rotation rate could be found. The impact of the rotation of the system on the generated magnetic field in dynamos is thereby barely understood.

In order to better understand the mechanism of the dynamo generation in such flows and the saturation process of the magnetic field, the G.O. Roberts flow is taken as a simple toy model for analytical approaches (Roberts 1972). One possible expression for this flow is

$$\mathbf{v}_R = v_0 \begin{bmatrix} \sqrt{2} \sin(\frac{2\pi}{a}x) \cos(\frac{2\pi}{a}y) \\ -\sqrt{2} \cos(\frac{2\pi}{a}x) \sin(\frac{2\pi}{a}y) \\ 2 \sin(\frac{2\pi}{a}x) \sin(\frac{2\pi}{a}y) \end{bmatrix}. \quad (3.1)$$

On the right hand side in Figure 3.1, the G. O. Roberts flow is shown in a vector plot in the  $(x, y)$ -plane with an underlying contourplot showing the  $z$ -component of the flow. It is a two-dimensional periodic flow, where the  $x$ - and  $y$ -components of the velocity are arranged in vortex cells of width  $a/2$ , in which the  $z$ -component of the velocity field is pointing alternately in positive or negative direction. The height  $L$  of the box defines the periodicity length of the magnetic field. The growing mode of the magnetic field in the kinematic regime has the following shape:  $\mathbf{B} = [\cos 2\pi z/L, \sin 2\pi z/L, 0]$ . The length scale of the growing magnetic field mode is thereby much larger than the length scale  $a$  of the small-scale velocity vortices and the dynamo becomes the more efficient the larger the aspect ratio  $L/a$  is. Due to this scale separation, the evolution of a magnetic field in this velocity field can be determined with the help of mean field theory (Krause and Rädler 1980). The back reaction of the magnetic field on the flow via the Lorentz force is small compared to the driving force close to the kinematic dynamo onset. Thus, it is treated as a weakly non-linear perturbation.

This theoretical approach has already been done in non-rotating G. O. Roberts like driven flows by Tilgner (1997) and Tilgner and Busse (2001), in order to compare analytical calculations with experimental results of the Karlsruhe experiment (Muller and Stieglitz 2002), which actually was inspired by the G. O. Roberts flow. The agreement shows fundamental insight in the relevant processes of the saturation mechanism.

In this chapter, this analytical approach of weakly non-linear theory is extended to a rotation of the system about the  $z$ -axis and compared to respective numerical simulations of the full MHD equations. The influence of the rotation on the specific modes in the saturated regime are investigated in the mean field picture. The different contributions to the Lorentz force, which are based on large- and small-scale magnetic fields, are studied with respect to estimates of the magnitude of their amplitudes.

Although these calculations are performed in the laminar regime, this study can give basic insight of the interaction of the velocity and magnetic fields in a rotating system. Con-

clusions with respect to other helical driven turbulent models or even real objects are reasonable, since parts of their magnetic field are believed to extend over large length scales in both regimes and are generated by convectonal columns with a similar mean flow.

### 3.1 Weakly non-linear theory

On the basis of the Navier-Stokes equation and the continuity equation of an incompressible fluid

$$\partial_t \mathbf{v} + (\mathbf{v} \cdot \nabla) \mathbf{v} = -\frac{1}{\rho} \nabla p + \nu \nabla^2 \mathbf{v} + \mathbf{F} + \frac{1}{\mu_0 \rho} (\nabla \times \mathbf{B}) \times \mathbf{B} + 2(\mathbf{v} \times \boldsymbol{\Omega}), \quad \nabla \cdot \mathbf{v} = 0, \quad (3.2)$$

and the induction equation

$$\partial_t \mathbf{B} + \nabla \times (\mathbf{B} \times \mathbf{v}) = \lambda \nabla^2 \mathbf{B}, \quad \nabla \cdot \mathbf{B} = 0, \quad (3.3)$$

the saturation mechanism of the magnetic energy and its dependence on the rotation rate  $\Omega$  is investigated with the help of mean field theory and weakly non-linear theory.

#### The magnetic field

The length scale  $L$  of the magnetic field mode, which is generated within the G.O. Roberts flow is much larger than the size  $a$  of the vortices. Due to this scale separation the magnetic field can be split into a  $z$ -dependent mean part averaged over one periodicity cell and a fluctuating part (Krause and Rädler 1980), given by

$$\mathbf{B} = \bar{\mathbf{B}} + \mathbf{b} \quad (3.4)$$

and fulfilling the equations

$$\langle \mathbf{B} \rangle = \langle \bar{\mathbf{B}} + \mathbf{b} \rangle = \bar{\mathbf{B}}, \quad \langle \mathbf{b} \rangle = 0, \quad (3.5)$$

where the brackets mean averaging over one periodicity cell in  $x$ - and  $y$ - direction

$$\langle \dots \rangle = \frac{1}{a^2} \int_x^{x+a} dx \int_y^{y+a} dy \dots \quad (3.6)$$

The mean magnetic field  $\bar{\mathbf{B}}$  is thereby independent of  $x$  and  $y$  and varies on a lengthscale  $L$  in  $z$ -direction. Performing the averaging of the magnetic field, the induction equation (eq. 3.3) yields

$$\partial_t \bar{\mathbf{B}} + \langle \nabla \times (\mathbf{b} \times \mathbf{v}) \rangle = \lambda \nabla^2 \bar{\mathbf{B}}. \quad (3.7)$$

Subtracting the averaged induction equation (eq. 3.7) from the full induction equation (eq. 3.3) yields the induction equation for  $\mathbf{b}$  as

$$\partial_t \mathbf{b} - (\bar{\mathbf{B}} \cdot \nabla) \mathbf{v} + (\mathbf{v} \cdot \nabla) \bar{\mathbf{B}} = \lambda \nabla^2 \mathbf{b} - \{ \nabla \times (\mathbf{b} \times \mathbf{v}) - \langle \nabla \times (\mathbf{b} \times \mathbf{v}) \rangle \}. \quad (3.8)$$

Close to parameters of the dynamo onset the time derivative of  $\mathbf{b}$  is small compared to the diffusive part ( $\partial_t \mathbf{b} \ll \lambda \nabla^2 \mathbf{b}$ ). It is assumed in the following

$$\frac{v_0 a}{\lambda} \ll 1 \quad \frac{a}{L} \ll 1 \quad \implies \quad |\mathbf{b}| \ll |\bar{\mathbf{B}}| \quad (3.9)$$

with the amplitude  $v_0$  of the G.O. Roberts flow such that equation 3.8 reduces to

$$\lambda \nabla^2 \mathbf{b} = -(\bar{\mathbf{B}} \cdot \nabla) \mathbf{v} \quad (3.10)$$

and  $\mathbf{b}$  turns out to be

$$\mathbf{b} = \frac{1}{2\lambda} \left( \frac{a}{2\pi} \right)^2 (\bar{\mathbf{B}} \cdot \nabla) \mathbf{v} + O\left( \frac{a}{L} \right)^2, \quad (3.11)$$

where only terms of zeroth order in  $a/L$  are left. Inserting the approximation of  $\mathbf{b}$  into the induction equation 3.7, the evolution of the mean magnetic field is given by

$$\partial_t \bar{\mathbf{B}} + \langle \nabla \times \left\{ \frac{1}{2\lambda} \left( \frac{a}{2\pi} \right)^2 [(\bar{\mathbf{B}} \cdot \nabla) \mathbf{v}] \times \mathbf{v} \right\} \rangle = \lambda \nabla^2 \bar{\mathbf{B}}. \quad (3.12)$$

### The velocity field

The fluid motion is driven by a time independent force field  $\mathbf{F} = F \mathbf{f}_R$  within a rotating frame of reference, whereas the rotation is about the  $z$ -axis. The evolution of the velocity field  $\mathbf{v}$  is described by the Navier-Stokes equation in equation 3.2. This equation includes the Coriolis force and the Lorentz force term, which is responsible for the magnetic field saturation. In the stationary state at low  $Re$  the inertial terms as well as the time derivative can be neglected. In the following the rotation of equation 3.2 will be used so that the pressure gradient term vanishes, giving

$$0 = \nu \nabla \times \nabla^2 \mathbf{v} + F \nabla \times \mathbf{f}_R + 2 \nabla \times (\mathbf{v} \times \boldsymbol{\Omega}) + \frac{1}{\mu_0 \rho} \nabla \times [(\nabla \times \mathbf{B}) \times \mathbf{B}], \quad (3.13)$$

$$\nabla \cdot \mathbf{v} = 0.$$

Using the mean field approach for  $\mathbf{B}$ , the Lorentz force term splits up into three non-vanishing terms

$$(\nabla \times \mathbf{B}) \times \mathbf{B} = (\nabla \times \bar{\mathbf{B}}) \times \bar{\mathbf{B}} + (\nabla \times \bar{\mathbf{B}}) \times \mathbf{b} + (\nabla \times \mathbf{b}) \times \bar{\mathbf{B}}. \quad (3.14)$$

Due to the derivative of  $\bar{\mathbf{B}}$  with respect to  $z$  the first and second term is of first order in  $a/L$  and therewith small compared to the third term, which is of zeroth order in  $a/L$ , so that here it is assumed that  $(\nabla \times \mathbf{B}) \times \mathbf{B} \approx (\nabla \times \mathbf{b}) \times \bar{\mathbf{B}}$ . With equation 3.11 the Navier-Stokes equation gives

$$0 = \nu \nabla \times \nabla^2 \mathbf{v} + F \nabla \times \mathbf{f}_R + 2 \nabla \times (\mathbf{v} \times \boldsymbol{\Omega}) + \frac{1}{\mu_0 \rho} \nabla \times \left\{ \left[ \nabla \times \frac{1}{2\lambda} \left( \frac{a}{2\pi} \right)^2 (\bar{\mathbf{B}} \cdot \nabla) \mathbf{v} \right] \times \bar{\mathbf{B}} \right\}. \quad (3.15)$$

Near the kinematic onset of dynamo action the Lorentz force is small compared to the other forces and is treated as a perturbation term in the following. Since the perturbation is singular, the velocity field, the mean magnetic field and the amplitude of the force field are expanded in orders of  $\epsilon$

$$\begin{aligned} \mathbf{v} &= \mathbf{v}_R + \epsilon \mathbf{v}_1 + \epsilon^2 \mathbf{v}_2 + \epsilon^3 \mathbf{v}_3 + \dots \\ F &= F_0 + \epsilon F_1 + \epsilon^2 F_2 + \epsilon^3 F_3 + \dots \\ \bar{\mathbf{B}} &= \epsilon \bar{\mathbf{B}}_1 + \epsilon^2 \bar{\mathbf{B}}_2 + \epsilon^3 \bar{\mathbf{B}}_3 + \dots, \end{aligned} \quad (3.16)$$

whereas  $\epsilon$  is an unknown parameter at first.

## 0. Order in $\epsilon$

In zeroth order 3.15 reduces to the simple relation

$$0 = \nu \nabla \times \nabla^2 \mathbf{v}_R + F_0 \cdot \nabla \times \mathbf{f}_R + 2 \nabla \times (\mathbf{v}_R \times \boldsymbol{\Omega}). \quad (3.17)$$

The axis of rotation is aligned with the  $z$ -axis  $\boldsymbol{\Omega} = [0, 0, \Omega]$  so that the Coriolis term is equal to zero

$$\nabla \times (\mathbf{v}_R \times \boldsymbol{\Omega}) = (\boldsymbol{\Omega} \cdot \nabla) \mathbf{v}_R = 0, \quad (3.18)$$

since the derivative of the velocity field is zero in direction of the axis of rotation. The Force amplitude is in zeroth order

$$F_0 = 8\pi^2 / a^2 \nu v_0 \quad \text{with} \quad \mathbf{f}_R = \mathbf{v}_R / v_0. \quad (3.19)$$

### 1. Order in $\epsilon$

In first order of  $\epsilon$  the Navier-Stokes equation has no additional terms compared to the zeroth order, since the last term in equation 3.15, the Lorentz force, is of order  $\sim \overline{\mathbf{B}}^2$ . Hence,  $\mathbf{v}_1 = 0$  and  $F_1 = 0$ . The induction equation in zeroth order represents the growth of the dominant mode at the kinematic dynamo onset

$$-\lambda \nabla^2 \overline{\mathbf{B}}_1 + \langle \nabla \times \left\{ \frac{1}{2\lambda} \left( \frac{a}{2\pi} \right)^2 [(\overline{\mathbf{B}}_1 \cdot \nabla) \mathbf{v}_R] \times \mathbf{v}_R \right\} \rangle = 0 \quad (3.20)$$

and yields

$$\mathfrak{J}_{v_R} \overline{\mathbf{B}}_1 := \begin{bmatrix} -\partial_z^2 & -k_z \partial_z & 0 \\ k_z \partial_z & -\partial_z^2 & 0 \\ 0 & 0 & -\partial_z^2 \end{bmatrix} \overline{\mathbf{B}}_1 = 0 \quad (3.21)$$

where the differential operator is abbreviated by  $\mathfrak{J}_{v_R}$  and  $k_z$  is the wave number in the  $z$ -direction of the dominant mode of the magnetic field

$$k_z = \frac{\sqrt{2} a v_0^2}{4 \pi \lambda^2} \quad \Leftrightarrow \quad v_0^2 = 2 \sqrt{2} \frac{\pi}{a} k_z \lambda^2. \quad (3.22)$$

Considering periodic boundary conditions,  $\overline{\mathbf{B}}_1$  has the following shape

$$\bar{\mathbf{B}}_1 = \hat{\mathbf{B}}_1 \begin{bmatrix} \cos k_z z + \theta \\ \sin k_z z + \theta \\ 0 \end{bmatrix}. \quad (3.23)$$

The height  $L$  of the box is chosen such that  $k_z = 2\pi/L$  is the fastest growing mode. The dominant mode can have an arbitrary phase  $\theta$  due to the periodic boundary conditions. Since the phase has no impact on the results, it is equal to zero in the following.

## 2. Order in $\epsilon$

In second order of  $\epsilon$ , the Lorentz force term appears in the Navier-Stokes equation for the first time. Thus, it describes the modification of  $\mathbf{v}$  due to the magnetic field in first order

$$0 = \nu \nabla \times \nabla^2 \mathbf{v}_2 + 2 \nabla \times (\mathbf{v}_2 \times \boldsymbol{\Omega}) + F_2 \cdot \nabla \times \mathbf{f}_R + \frac{1}{\mu_0 \rho} \nabla \times \left\{ \left[ \nabla \times \frac{1}{2\lambda} \left( \frac{a}{2\pi} \right)^2 (\bar{\mathbf{B}}_1 \cdot \nabla) \mathbf{v}_R \right] \times \bar{\mathbf{B}}_1 \right\}. \quad (3.24)$$

The derivative of  $\bar{\mathbf{B}}_1$  in  $z$ -direction is of order  $1/L$ , whereas  $\mathbf{b}$  and  $\mathbf{v}$  vary on scales  $1/a$ , so that in the following derivatives in  $z$  are neglected ( $\partial_z \ll \partial_x, \partial_y$ ) as far as terms with  $\boldsymbol{\Omega}$  are not involved, because  $\boldsymbol{\Omega}$  can indeed become large. The Lorentz force term  $\mathbf{F}_L$  is in this approximation

$$\mathbf{F}_L = \frac{\sqrt{2}}{2} \frac{v_0}{\nu \rho \mu_0 \lambda} \frac{\pi}{a} \left\{ \hat{\mathbf{B}}_1^2 \sin(2k_z z) \begin{bmatrix} -\sqrt{2} & \sin \frac{2\pi y}{a} \cos \frac{2\pi x}{a} \\ \sqrt{2} & \sin \frac{2\pi x}{a} \cos \frac{2\pi y}{a} \\ 2 & \cos \frac{2\pi x}{a} \cos \frac{2\pi y}{a} \end{bmatrix} - \hat{\mathbf{B}}_1^2 \frac{\mathbf{v}_R}{v_0} \right\}. \quad (3.25)$$

The  $x, y$ -dependence only appears in certain combinations of sin and cos which leads to the following Ansatz for  $\mathbf{v}_2 = (v_1, v_2, v_3)$ :

$$\begin{aligned} v_1 &= a_1 \cos \frac{2\pi y}{a} \sin \frac{2\pi x}{a} + a_2 \sin \frac{2\pi y}{a} \cos \frac{2\pi x}{a} \\ v_2 &= a_3 \sin \frac{2\pi y}{a} \cos \frac{2\pi x}{a} + a_4 \cos \frac{2\pi y}{a} \sin \frac{2\pi x}{a} \\ v_3 &= a_5 \sin \frac{2\pi y}{a} \sin \frac{2\pi x}{a} + a_6 \cos \frac{2\pi y}{a} \cos \frac{2\pi x}{a}. \end{aligned} \quad (3.26)$$

This leads to a coupled set of 6 linear equations for the coefficients  $\mathbf{a} = [a_1 \dots a_6]$

$$\begin{aligned}
 & \begin{bmatrix} \frac{4\pi\Omega}{av} & 16\left(\frac{\pi}{a}\right)^3 & -16\left(\frac{\pi}{a}\right)^3 & \frac{4\pi\Omega}{av} & 0 & 0 \\ -16\left(\frac{\pi}{a}\right)^3 & -\frac{4\pi\Omega}{av} & -\frac{4\pi\Omega}{av} & 16\left(\frac{\pi}{a}\right)^3 & 0 & 0 \\ 0 & -\frac{2\Omega}{\nu}\partial_z & 0 & 0 & 0 & 16\left(\frac{\pi}{a}\right)^3 \\ -\frac{2\Omega}{\nu}\partial_z & 0 & 0 & 0 & -16\left(\frac{\pi}{a}\right)^3 & 0 \\ 0 & 0 & 0 & -\frac{2\Omega}{\nu}\partial_z & 16\left(\frac{\pi}{a}\right)^3 & 0 \\ 0 & 0 & -\frac{2\Omega}{\nu}\partial_z & 0 & 0 & -16\left(\frac{\pi}{a}\right)^3 \end{bmatrix} \cdot \mathbf{a} \\
 & = \begin{bmatrix} \frac{\sqrt{2}2\pi\nu_0\hat{B}^2}{\nu\mu_0\lambda\rho a} \sin(2k_z z) \\ -\frac{\sqrt{2}2\pi\nu_0\hat{B}_1^2}{\nu\mu_0\lambda\rho a} \sin(2k_z z) \\ -\frac{\nu\mu_0\lambda\rho a}{2\pi\nu_0\hat{B}_1^2} \sin(2k_z z) \\ -\frac{\nu\mu_0\lambda\rho a}{2\pi\nu_0\hat{B}_1^2} \sin(2k_z z) \\ \frac{\nu\mu_0\lambda\rho a}{2\pi\nu_0\hat{B}_1^2} \sin(2k_z z) \\ \frac{\nu\mu_0\lambda\rho a}{2\pi\nu_0\hat{B}_1^2} \sin(2k_z z) \end{bmatrix}.
 \end{aligned} \tag{3.27}$$

The last four equations are satisfied for  $\partial_z a_2 = -\partial_z a_3$  and  $\partial_z a_1 = -\partial_z a_4$  and the first and second equations for  $a_2 = -a_3$  and  $a_1 = -a_4$ . Not considering the continuity equation, the velocity field of second order in  $\epsilon$ ,  $\mathbf{v}_2$ , reads after straight forward calculations

$$\begin{aligned}
 \mathbf{v}_2 &= \frac{\hat{B}_1^2}{4} \left(\frac{a}{2\pi}\right)^2 \zeta \sin(2k_z z) \tilde{\mathbf{v}}_0 - \left(\frac{\hat{B}_1^2}{4}\zeta - \frac{F_2}{2\nu\nu_0}\right) \left(\frac{a}{2\pi}\right)^2 \mathbf{v}_R \\
 &+ \frac{\sqrt{2}}{4} \left(\frac{a}{2\pi}\right)^5 \zeta \frac{\Omega k}{\nu} \hat{B}_1^2 \cos(2k_z z) \tilde{\mathbf{v}}_{0z},
 \end{aligned} \tag{3.28}$$

with  $\zeta = 1/\nu\rho\mu_0\lambda$  and

$$\tilde{\mathbf{v}}_0 = v_0 \begin{bmatrix} -\sqrt{2} \sin \frac{2\pi y}{a} \cos \frac{2\pi x}{a} \\ \sqrt{2} \sin \frac{2\pi x}{a} \cos \frac{2\pi y}{a} \\ 2 \cos \frac{2\pi x}{a} \cos \frac{2\pi y}{a} \end{bmatrix}. \tag{3.29}$$

In order to fulfill the continuity equation, it is exploited that a gradient field  $\nabla\Phi$  can be added without restrictions because  $\nabla \times (\nabla\Phi) = 0$ . The scalar field  $\Phi$  is chosen in that way that in the continuity equation no term including  $\Omega$  or others of order  $O(a/L)$  remains, i.e.

$$\Phi = \frac{-1}{2\left(\frac{a}{\pi}\right)^2 + k^2} \frac{\sqrt{2}}{128} \left(\frac{a}{\pi}\right)^5 \frac{v_0 \Omega k_z^2 \hat{\mathbf{B}}_1^2}{v^2 \lambda \mu_0 \rho} \sin(2k_z z) \cos \frac{2\pi}{a} y \cos \frac{2\pi}{a} x. \quad (3.30)$$

In summary the velocity is given by

$$\begin{aligned} \mathbf{v} = & \left( 1 - \epsilon^2 \gamma \left[ 1 - \frac{2F_2}{\zeta \hat{\mathbf{B}}_1^2 v_0 \nu} \right] \right) \mathbf{v}_R \\ & + \epsilon^2 \gamma \left( \sin(2k_z z) \tilde{\mathbf{v}}_0 + \frac{\sqrt{2}}{8} \left(\frac{a}{\pi}\right)^3 \frac{k_z \Omega}{v} \cos(2k_z z) \tilde{\mathbf{v}}_{0z} + \frac{\nabla \Phi}{\gamma} \right) + O(\epsilon^4) \end{aligned} \quad (3.31)$$

with  $\gamma = \frac{1}{16} \left(\frac{a}{\pi}\right)^2 \zeta \hat{\mathbf{B}}_1^2$ . Compared to the first order, the induction equation has no additional term in second order in  $\epsilon$  and thus  $\bar{\mathbf{B}}_2 = 0$ .

### 3. Order in $\epsilon$

In third order  $\mathbf{v}_3$  is zero because of the linear independence to the lower orders. The induction equation in third order is not homogeneous any more. The differential equation for the magnetic field  $\bar{\mathbf{B}}_3$  reads

$$\begin{aligned} -\lambda \nabla^2 \bar{\mathbf{B}}_3 + \frac{1}{2\lambda} \left(\frac{a}{2\pi}\right)^2 \langle \nabla \times \{[(\bar{\mathbf{B}}_3 \cdot \nabla) \mathbf{v}_R] \times \mathbf{v}_R\} \rangle = \\ - \frac{1}{2\lambda} \left(\frac{a}{2\pi}\right)^2 \langle \nabla \times \{[(\bar{\mathbf{B}}_1 \cdot \nabla) \mathbf{v}_R] \times \mathbf{v}_2 + [(\bar{\mathbf{B}}_1 \cdot \nabla) \mathbf{v}_2] \times \mathbf{v}_R\} \rangle \end{aligned} \quad (3.32)$$

and in a simpler form

$$\mathfrak{J}_{v_R} \bar{\mathbf{B}}_3 = I_R \quad (3.33)$$

with  $\mathfrak{J}_{v_R}$  as the linear differential operator of equation 3.21 and  $I_R$  as the sum of the righthand side of equation 3.32. The condition for solvability of equation 3.32 can be found by the projection of an arbitrary function  $y$

$$\langle y | \mathfrak{J}_{v_R} \bar{\mathbf{B}}_3 \rangle = \langle \mathfrak{J}_{v_R}^\dagger y | \bar{\mathbf{B}}_3 \rangle = \langle y | I_R \rangle, \quad (3.34)$$

where bra-kets denote the integration over one periodicity cell in z-direction and  $\mathfrak{J}_{v_R}^\dagger$  is

the adjoint matrix of  $\mathfrak{Y}_{v_R}$ . If  $y$  is the kernel of  $\mathfrak{Y}_{v_R}^\dagger$ , it has to be  $\langle y | I_R \rangle = 0$  so that the differential equation is solvable. Since  $\mathfrak{Y}_{v_R}$  is hermitian the adjoint matrix is equal to the original one

$$\mathfrak{Y}_{v_R}^\dagger = \mathfrak{Y}_{v_R} = \begin{bmatrix} -\partial_z^2 & -k_z \partial_z & 0 \\ k_z \partial_z & -\partial_z^2 & 0 \\ 0 & 0 & -\partial_z^2 \end{bmatrix}. \quad (3.35)$$

The kernel  $y$  of  $\mathfrak{Y}_{v_R}$  is

$$y = \begin{bmatrix} \cos(kz + \varphi) \\ \sin(kz + \varphi) \\ 0 \end{bmatrix} \quad (3.36)$$

an therefore equal to  $\overline{B}_1$  or phase shifted to it by an angle  $\varphi$ . The righthand side of equation 3.32,  $I_R$ , is

$$\begin{aligned} I_R = & \frac{8 \sqrt{2} k_z a^3 v_0 \hat{B}_1 (3v_0 \hat{B}_1^2 - 4\lambda \rho \mu_0 F_2)}{512 \lambda^2 \nu \mu_0 \rho \pi^3} \begin{bmatrix} \cos k_z z \\ \sin k_z z \\ 0 \end{bmatrix} \\ & - \frac{\sqrt{2} \hat{B}_1^3 \Omega k_z^2 a^6 v_0}{512 \pi^6 \lambda^2 \nu^2 \mu_0 \rho} \frac{\sqrt{2} a k_z + \pi}{2\pi^2 + k_z^2 a^2} \begin{bmatrix} -\sin k_z z \\ \cos k_z z \\ 0 \end{bmatrix} \\ & + \frac{3 \sqrt{2}}{16} \frac{\hat{B}_1^3 a^3 v_0^2}{\pi^3 \lambda^2 \nu \mu_0 \rho} \begin{bmatrix} -\cos 3k_z z \\ \sin 3k_z z \\ 0 \end{bmatrix} \\ & - \frac{3 \sqrt{2}}{512} \frac{k_z^2 a^6 v_0^2}{\pi^6 \lambda^2 \nu^2 \mu_0 \rho} \frac{\sqrt{2} k_z a + 2\pi}{2\pi^2 + k_z^2 a^2} \begin{bmatrix} \sin 3k_z z \\ \cos 3k_z z \\ 0 \end{bmatrix}. \end{aligned} \quad (3.37)$$

For  $\langle y | I_R \rangle = 0 |_{\varphi=0}$  the first term in equation 3.37 yield the condition for the free parameter, which is undetermined,

$$F_2 = \frac{3}{4} \frac{v_0}{\lambda \rho \mu_0} \hat{B}_1^2. \quad (3.38)$$

But obviously  $\langle y | I_R \rangle = 0$  is not solvable for all  $\varphi$ , such that equation 3.32 has the trivial

solution  $\bar{\mathbf{B}}_3 = 0$  for a stationary magnetic field.

### Time dependent magnetic field

The result of the mean magnetic field in third order hypothesizes that the time dependence of  $\bar{\mathbf{B}}$  in the mean induction equation cannot be neglected. The solution to this problem can be a time dependent phase of the mean magnetic field  $\bar{\mathbf{B}}(z - v_{ph}t)$ , where the phase velocity  $v_{ph}$  is another perturbation term and also expanded in  $\epsilon$ . The time derivative of  $\bar{\mathbf{B}}$  gives

$$\frac{\partial \bar{\mathbf{B}}}{\partial t} = -v_{ph} \frac{\partial \bar{\mathbf{B}}}{\partial z} = -(v_{ph,0} + \epsilon v_{ph,1} + \epsilon^2 v_{ph,2}) \frac{\partial}{\partial z} (\epsilon \bar{\mathbf{B}}_1 + \epsilon^3 \bar{\mathbf{B}}_3). \quad (3.39)$$

The mode  $\bar{\mathbf{B}}_1$  is stationary in the kinematic dynamo regime, therefore  $v_{ph,0} = v_{ph,1} = 0$  and only  $-\epsilon^3 v_{ph,2} \partial_z \bar{\mathbf{B}}_1$  finally appears in  $I_R$  with

$$-v_{ph,2} \partial_z \bar{\mathbf{B}}_1 = -v_{ph,2} k_z \begin{bmatrix} -\sin k_z z \\ \cos k_z z \\ 0 \end{bmatrix}. \quad (3.40)$$

On account of this the second term in equation 3.37 becomes a function of  $v_{ph,2}$  and  $\langle y | I_R \rangle = 0 |_{\varphi=\pi/2}$  gives

$$v_{ph,2} = \frac{1}{512} \frac{\hat{\mathbf{B}}_1^2 k_z v_0^2 a^6 \Omega}{\pi^5 \lambda^2 \nu^2 \mu_0 \rho} \frac{(2\pi - \sqrt{2}ak)}{(2\pi^2 + k^2 a^2)}. \quad (3.41)$$

This demonstrates that in third order of  $\epsilon$ , there is a time dependent solution. Using this dynamic approach, the velocity field becomes

$$\mathbf{v} = \left(1 + \frac{1}{2} \epsilon^2 \gamma\right) \mathbf{v}_R + \epsilon^2 \gamma \left( \sin 2k_z z \tilde{\mathbf{v}}_0 + \frac{\sqrt{2}}{8} \left(\frac{a}{\pi}\right)^3 \frac{k_z \Omega}{\nu} \cos 2k_z z \tilde{\mathbf{v}}_{0z} + \frac{\nabla \Phi}{\gamma} \right) + O(\epsilon^4). \quad (3.42)$$

The factor  $\epsilon^2 \gamma$  indicates the ratio of Lorentz to driving force and , thus, gives a measure for the accuracy of the approximation. The magnetic field of third order in  $\epsilon$  has the following shape:

$$\begin{aligned} \bar{\mathbf{B}}_3 = & \frac{1}{64\pi^2} \frac{a^2 \hat{\mathbf{B}}_1^3}{\mu_0 \rho \lambda \nu} \begin{bmatrix} -\cos 3kz \\ \sin 3kz \\ 0 \end{bmatrix} \\ & + \frac{1}{512\pi^5} \frac{a^5 \hat{\mathbf{B}}_1^3 \Omega k (\sqrt{2}\pi^2 + \sqrt{2}k^2 a^2 - a\pi k)}{\lambda \mu_0 \nu^2 \rho} \frac{1}{2\pi^2 + a^2 k^2} \begin{bmatrix} \sin 3kz \\ \cos 3kz \\ 0. \end{bmatrix} \end{aligned} \quad (3.43)$$

According to that the magnetic energy is

$$\begin{aligned} E_B &= \frac{1}{L} \int \frac{1}{2} |\bar{\mathbf{B}}|^2 dz = \frac{1}{2} \epsilon^2 \hat{\mathbf{B}}_1^2 + \frac{1}{2L} \epsilon^6 \int |\bar{\mathbf{B}}_3|^2 dz + O(\epsilon^8) \\ &= E_{B,1} + \left( \frac{\sqrt{2}}{128\pi^2} \frac{\epsilon^3 \hat{\mathbf{B}}_1^3 a^2}{\mu_0 \rho \lambda \nu} \right)^2 + \left( \frac{\sqrt{2}}{1024\pi^5} \frac{\epsilon^3 \hat{\mathbf{B}}_1^3 \Omega a^5 k_z (\sqrt{2}\pi^2 + \sqrt{2}k^2 a^2 - a\pi k)}{\lambda \mu_0 \nu^2 \rho} \frac{1}{2\pi^2 + a^2 k^2} \right)^2 + O(\epsilon^8). \end{aligned} \quad (3.44)$$

The force field is given by

$$F = 8 \left( \frac{\pi}{a} \right)^2 \nu v_0 + \epsilon^2 \frac{3}{4} \frac{v_0}{\lambda \mu_0 \rho} \hat{\mathbf{B}}_1^2. \quad (3.45)$$

### Summary

The perturbation expansion was extended up to third order in  $\epsilon$  and the respective velocity and magnetic field were determined. The divergence of the velocity field is zero, neglecting terms of orders in  $a/L$  or higher order. The magnetic energy is dependent on  $Ek^{-2}$  but surprisingly, it appears first in third order of  $\epsilon$ . The equation for the mean magnetic field in third order of  $\epsilon$  only becomes solvable incorporating a time dependence of the respective field and predicts a drift of the dominant mode  $\bar{\mathbf{B}}_1$ . The phase velocity is proportional to  $Ek^{-1}$  and therewith a new phenomenon which does not occur in the non-rotating case.

## 3.2 Results of the numerical model

In the following, the full equations 3.2 and 3.3 are investigated numerically in a periodic box model. The box has a quadratic base area of width  $a$  and a height  $d$ . The entire system rotates about the z-axis, which is defined as perpendicular to the quadratic base area and rotates with a rotation rate  $\Omega$ . The flow is driven by a volume force, which generates the G. O. Roberts flow in the laminar purely hydrodynamic regime. Both equations are integrated simultaneously in a pseudo spectral code, where the velocity and the magnetic field are expanded in Fourier modes. The transformation from real to spectral space and backwards is realized by the fast Fourier transformation routine `rlft3` from the Numerical Recipes (Press et al. 1986):

$$\mathbf{v} = \sum_{ijl} \mathbf{a}_{ijl} e^{-i(kx_i x + ky_j y + kz_l z)} + \mathbf{a}_{ijl}^* e^{i(kx_i x + ky_j y + kz_l z)} \quad (3.46)$$

$\mathbf{a}_{ijl}$  contains the three Fourier amplitudes of the corresponding mode for  $v_x$ ,  $v_y$  and  $v_z$  and  $\mathbf{a}_{ijl}^*$  is the complex conjugated. A second triple of arrays stores the respective amplitudes for the magnetic field, which is expanded in the same way. Since the magnetic and velocity fields are real, only half of the amplitudes have to be stored. The time step is a combination of an Eulerstep for the diffusion part and a second order Crank-Nicolson for the non-linear terms and the Coriolis force.

### 3.2.1 Non-linear Navier-Stokes equation

The evolution of the velocity field is described by the full Navier-Stokes equation, including the Coriolis force, with  $\mathbf{\Omega} = \Omega \hat{e}_z$ , and  $\hat{e}_z$  the unit vector in z-direction and the Lorentz force

$$\partial_t \mathbf{v} + (\mathbf{v} \cdot \nabla) \mathbf{v} = -\frac{1}{\rho} \nabla p + \nu \nabla^2 \mathbf{v} + \mathbf{F} + \frac{1}{\mu_0 \rho} (\nabla \times \mathbf{B}) \times \mathbf{B} - 2(\mathbf{\Omega} \times \mathbf{v}). \quad (3.47)$$

The force field  $\mathbf{F}$  is chosen such that with  $\mathbf{B} = 0$  and  $\partial_t \mathbf{v} = 0$  a solution of  $\mathbf{v}$  is

$$\mathbf{v} = v_a \begin{bmatrix} \sqrt{2} \sin(\frac{2\pi}{a} x) & \cos(\frac{2\pi}{a} y) \\ -\sqrt{2} \cos(\frac{2\pi}{a} x) & \sin(\frac{2\pi}{a} y) \\ 2 & \sin(\frac{2\pi}{a} x) & \sin(\frac{2\pi}{a} y) \end{bmatrix}. \quad (3.48)$$

According to the result for  $\mathbf{F}$  in the analytical calculation (eq. 3.19), the force field is the same except for a gradient field  $L$ , which depends on the rotation rate and does not appear in the vorticity equation, because of  $\nabla \times (\nabla L) = 0$ .

$$\mathbf{F} = 8 \left( \frac{\pi}{a} \right)^2 \nu v_a \mathbf{v}_R + \nabla \cdot L(\Omega) \quad (3.49)$$

In this case, the gradient field is balanced by the pressure gradient, so that in fact it doesn't contribute to the force term. The pressure is solved in spectral space by taking the divergence of equation 3.2.1. By this, it is guaranteed that the velocity field is solenoidal. The dimensionless momentum equation is obtained by the scaling of the variables as follows:

$$\begin{aligned} \mathbf{x} &\rightarrow \mathbf{x}' a \\ \mathbf{v} &\rightarrow \mathbf{v}' v_a \\ t &\rightarrow t' \frac{a}{v_a} \\ \mathbf{B} &\rightarrow \mathbf{B}' \sqrt{\mu_0 \rho} v_a \\ p &\rightarrow p' \rho v_a^2. \end{aligned} \quad (3.50)$$

For simplicity the primes are omitted in the following and the dimensionless Navier-Stokes equation reads

$$\partial_t \mathbf{v} + (\mathbf{v} \cdot \nabla) \mathbf{v} = -\nabla p + \frac{1}{\text{Re}} \nabla^2 \mathbf{v} + \mathbf{F} + (\nabla \times \mathbf{B}) \times \mathbf{B} - 2 \frac{1}{\text{Re Ek}} (\hat{e}_z \times \mathbf{v}) \quad (3.51)$$

with the Reynolds number  $\text{Re} = v_a a / \nu$  and Ekman number  $\text{Ek} = \nu / \Omega a^2$ . The evolution of the magnetic field is described by the induction equation 3.3, which in dimensionless form reads

$$\partial_t \mathbf{B} + \nabla \times (\mathbf{B} \times \mathbf{v}) = \frac{1}{\text{Rm}} \nabla^2 \mathbf{B} \quad (3.52)$$

with the magnetic Reynolds number  $\text{Rm} = v_a a / \lambda$ .

## Dimensionless analytical results

The force terms in the analytical calculations and the numerical simulations are not the same (compare eq. 3.49 and 3.45). The definition of  $Rm$  with the different amplitudes  $v_0$  and  $v_a$  of the G. O. Roberts flows are not comparable by implication. That's why the amplitudes of the force terms themselves have to be compared. The magnetic Reynolds number  $Rm = v_a a / \lambda$  is defined by the velocity amplitude  $v_a$ , which is generated by the force amplitude (eq. 3.49) in the absence of any magnetic field  $\mathbf{B} = 0$  and time derivatives  $\partial_t \mathbf{v} = 0$ . Accordingly, the force amplitude 3.45 generates a G. O. Roberts flow with the velocity amplitude  $v_g$

$$v_g = v_0 + \frac{3}{32\nu} \left(\frac{a}{\pi}\right)^2 \epsilon^2 \hat{B}_1^2 \frac{v_0}{\lambda \rho \mu_0}. \quad (3.53)$$

The force terms and thus the velocity amplitudes  $v_g$  and  $v_a$  have to be the same  $v_g = v_a$ , so that with 3.22 the definition of  $Rm$  is given by

$$Rm = \sqrt{2 \sqrt{2} a \pi k_z} + \frac{2^{1/4} 3 a^2 \epsilon^2 \hat{B}_1^2}{16 \pi \lambda \rho \mu_0 \nu} \sqrt{\frac{a}{L}}. \quad (3.54)$$

In order to point out that  $v_g$  is the amplitude of the driving force in equation 3.45, it seems to be useful to label it differently in the following. The magnetic energy in dimensional form is

$$\frac{\epsilon^2 \hat{B}_1^2}{\rho \mu_0} = \frac{\nu \lambda}{a^2} (Rm - Rm_c) \frac{16 \pi 2^{-1/4}}{3} \sqrt{\frac{L}{a}}, \quad (3.55)$$

with  $Rm_c$ , the kinematic dynamo onset

$$Rm_c = \frac{v_0 a}{\lambda} = \sqrt{2 \sqrt{2} a \pi k_z} = \sqrt{4 \sqrt{2} \frac{a}{L} \pi^2}. \quad (3.56)$$

Apart from that, the parameters of the numerical simulation must obey the assumptions, made for the analytical approach (see eq. 3.9). The kinematic dynamo onset is given by the aspect ratio of the periodic box. In order to get  $Rm \ll 1$  (e.g. with  $Rm_c = 0.1$ ), a large aspect ratio  $a/L = Rm_c^2 / (4 \sqrt{2} \pi^2) \approx 1.8 \times 10^{-4}$  has to be taken. The saturated state is reached when induction and diffusive processes are balanced. Since the dynamo is sustained by the  $\alpha$ -effect, the induction of magnetic energy takes place on time scales  $a/v_a$ , while diffusion occurs on time scales  $L^2/\lambda$ . Finally, the time, the system needs to saturate, is dominated by the slower process, to which the other adapts immediately. The

dimensionless diffusion time is  $\tau_\lambda \sim \text{Rm}(L/a)^2$  and in this case  $\sim 10^6$ . The aspect ratio has to be chosen in the way that  $\text{Rm} \ll 1$  is reasonably satisfied and that the saturation time is not too high. In the simulations that are presented in the following the aspect ratio is taken as  $L/a = 650$  and thus  $\text{Rm}_c \approx 0.2931$ . The spatial resolution in all direction is  $\text{dim} = 8$ , which includes the first four Fourier modes and the mean field. The parameters are varied from  $\text{Rm} = 0.295 \dots 1$  and  $\text{Ek} = \infty \dots 10^{-3}$  with  $\text{Re} = 10$ . The most interesting outputs are the kinetic energy

$$E_{K,num} = \frac{1}{2} \int |\mathbf{v}|^2 dV \quad (3.57)$$

and the magnetic energy

$$E_{B,num} = \frac{1}{2} \int |\mathbf{B}|^2 dV \quad (3.58)$$

with the dimension  $\rho\mu_0 v_a^2$ . Taking this dimension, the analytical result deduced from equation 3.55 becomes

$$E_{B,1} = \frac{1}{2} \frac{\epsilon^2 \hat{\mathbf{B}}_1^2}{\rho\mu_0 v_g^2} = \frac{(\text{Rm} - \text{Rm}_c) 8 \pi 2^{-1/4}}{\text{Rm Re}} \sqrt{\frac{L}{a}}. \quad (3.59)$$

Equation 3.44 represents the magnetic energy in third order and becomes with the same dimensions

$$E_{B,3} = \left( \frac{\sqrt{2}}{128\pi^2} \right)^2 E_{B,1}^3 \text{Rm}^2 \text{Re}^2 + E_{B,1}^3 \text{Ek}^{-2} \text{Re}^2 \text{Rm}^2 (ak_z)^2 \left( \frac{\sqrt{2}}{1024\pi^5} \frac{(\sqrt{2}\pi^2 + \sqrt{2}k^2 a^2 - a\pi k)}{2\pi^2 + a^2 k^2} \right)^2. \quad (3.60)$$

Hence, the amplitude of the total magnetic energy depends on  $\text{Ek}$  and  $\text{Rm}$  and can be split into different parts with different dependencies

$$E_B = A \frac{(\text{Rm} - \text{Rm}_c)}{\text{Rm}} + B f(\text{Rm}) + C f(\text{Rm}) \text{Ek}^{-2}, \quad (3.61)$$

where  $f(\text{Rm}) = \frac{(\text{Rm} - \text{Rm}_c)^3}{\text{Rm}}$  and

$$\begin{aligned}
A &= \frac{8 \pi 2^{-1/4}}{3} \sqrt{\frac{L}{a}} \frac{1}{\text{Re}} \\
B &= \left( \frac{\sqrt{2}}{128\pi^2} \right)^2 \frac{8 \pi 2^{-1/4}}{3} \sqrt{\frac{L}{a}} \text{Re} \\
C &= \frac{8 \pi 2^{-1/4}}{3} \sqrt{\frac{L}{a}} \text{Re} (ak_z)^2 \left( \frac{1}{2^{16}\pi^7} \frac{(\sqrt{2}\pi^2 + \sqrt{2}k^2a^2 - a\pi k)^2}{2\pi^2 + a^2k^2} \right)^2.
\end{aligned} \tag{3.62}$$

## Comparison of numerical and analytical results

The magnetic energy obtained from equation 3.61 and the respective numerical results are shown in Figure 3.2. Lines denote the results of the analytical calculation. The symbols are data points of the numerical simulations. The first Figure on the left side shows the total magnetic energy  $E_{B,num}$  in the non-rotating case and the contributions of different orders of  $E_B$  plotted against  $Rm$ . In the non-rotating case, the approximation matches quite well with the numerical results up to  $Rm \approx 0.4$ , which is about one third overcritical.

The right upper plot shows the absolute deviation of the magnetic energy of the rotating system from the non-rotating one  $|E_B(Ek = \infty) - E_B(Ek)|$  for each  $Rm$ . This is represented by the analytical expression  $C f(Rm) Ek^{-2}$  in equation 3.61. At  $Rm < 0.32$ , the magnetic energy increases with the rotation rate as confirmed by the analytical results.

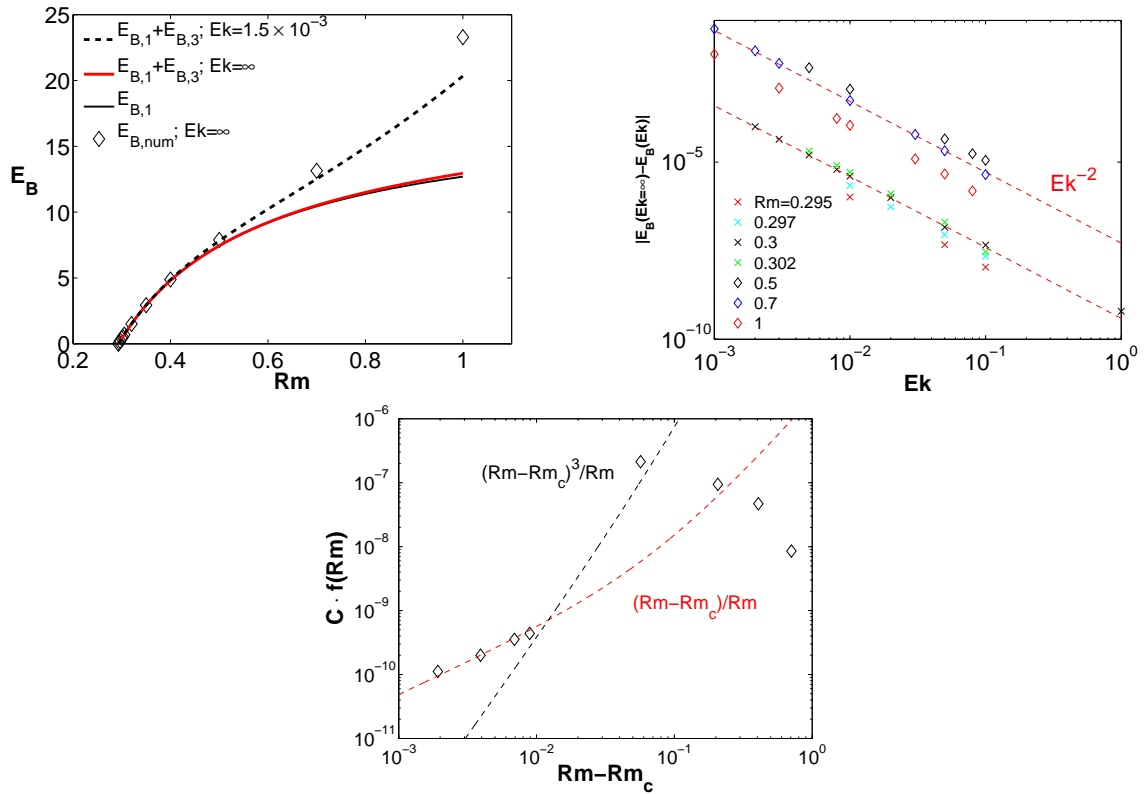


Figure 3.2: In the left panel  $E_{B,num}$  is plotted over  $Rm$  together with the analytical results of the magnetic energy of first order  $E_{B,1}$  (black), the total magnetic energy  $E_B$  without rotation (red) and at  $Ek = 1.5 \times 10^{-3}$ . In the middle figure the absolute amplitude of the rotationally dependent part of the magnetic energy  $|E_B(Ek = \infty) - E_B(Ek)|$  is plotted over  $Ek$ . The red dashed lines indicate a proportionality to  $Ek^{-2}$ . The amplitude of each fit in the middle Figure is plotted over  $Rm$  on the right hand side and shows a proportionality to  $Rm - Rm_c / Rm$  (red dashed). The corresponding analytical expression gives  $\sim (Rm - Rm_c)^3 / Rm$  (black dashed).

For  $Rm > 0.32$  the magnetic energy decreases with the rotation rate. Surprisingly, the dependency on  $Ek^{-2}$  is very robust even for  $Rm > 1$ , which is not shown in this plot. The red dashed lines denote powerlaws of  $Ek^{-2}$ .

In the lower panel, the fitted amplitudes to each set of simulations at a certain  $Rm$  in the upper right figure is plotted against  $Rm$ . It shows the development of the amplitude of the rotationally dependent part of  $E_B$  over  $Rm$ . Related to equation 3.61, this plot represents the function  $C f(Rm)$ . Contrary to the analytical results, where the  $\Omega$ -dependency appears in the third order of the perturbation expansion, the amplitudes show a  $(Rm - Rm_c)/Rm$  development up to  $Rm \approx 0.303$ , which is only 3% overcritical. The black dashed line denotes the third order dependency of  $(Rm - Rm_c)^3/Rm$  of the analytical equation, whereas the amplitude is adapted to fit within the plot. In fact, it is 5 orders of magnitude lower, which is already close to the numerical accuracy. Besides, the numerical results exhibits a decreasing trend of the amplitude of the rotationally dependent part of the magnetic energy for higher  $Rm > 0.303$ .

In order to find the reason for this inconsistency, the magnetic and the velocity field are decomposed into their Fourier components. Therefore, the respective amplitudes of the modes of equation 3.46 are compared with the corresponding analytical amplitudes. The amplitudes of the velocity field modes of the G. O. Roberts flow are up to a certain accuracy

$$\begin{aligned}
 a_{x,221} &= ia_R \\
 a_{x,281} &= ia_R \\
 a_{y,221} &= -ia_R \\
 a_{y,281} &= ia_R \\
 a_{z,221} &= \sqrt{2}a_R \\
 a_{z,281} &= \sqrt{2}a_R
 \end{aligned} \tag{3.63}$$

and additional modes with a higher wave vector  $kz$  in z-direction

$$\begin{aligned}
 a_{x,223} &= a_1 + ib \\
 a_{x,283} &= -a_2 - ic \\
 a_{x,227} &= -a_1 + ib \\
 a_{x,287} &= a_2 - ic \\
 a_{y,223} &= -a_2 - ic \\
 a_{y,283} &= -a_1 - ib \\
 a_{y,227} &= a_2 - ic \\
 a_{y,287} &= a_1 - ib
 \end{aligned} \tag{3.64}$$

$$\begin{aligned}
 a_{z,223} &= \frac{\sqrt{2}}{2}(b+c) + i\frac{\sqrt{2}}{2}(a_1+a_2) \\
 a_{z,283} &= -\frac{\sqrt{2}}{2}(b+c) - i\frac{\sqrt{2}}{2}(a_1+a_2) \\
 a_{z,227} &= -\frac{\sqrt{2}}{2}(b+c) + i\frac{\sqrt{2}}{2}(a_1+a_2) \\
 a_{z,287} &= \frac{\sqrt{2}}{2}(b+c) - i\frac{\sqrt{2}}{2}(a_1+a_2)
 \end{aligned}$$

with

$$kx_2 = \frac{2\pi}{a} \quad ky_2 = \frac{2\pi}{a} \quad kz_1 = 0 \tag{3.65}$$

$$ky_8 = -\frac{2\pi}{a} \quad kz_3 = \frac{4\pi}{L} \tag{3.66}$$

$$kz_7 = -\frac{4\pi}{L} \tag{3.67}$$

and give the following velocity field taking  $\tilde{x} = 2\pi x/a$  and  $\tilde{y} = 2\pi y/a$

$$\begin{aligned}
 \mathbf{v}_{num} &= A_R \begin{bmatrix} \sin \tilde{x} \cos \tilde{y} \\ -\cos \tilde{x} \sin \tilde{y} \\ \sqrt{2} \sin \tilde{x} \sin \tilde{y} \end{bmatrix} \\
 &+ A_1 \sin 2k_z z \begin{bmatrix} -\cos \tilde{x} \sin \tilde{y} \\ \sin \tilde{x} \cos \tilde{y} \\ \sqrt{2} \cos \tilde{x} \cos \tilde{y} \end{bmatrix} + A_2 \cos 2k_z z \begin{bmatrix} -\sin \tilde{x} \cos \tilde{y} \\ \cos \tilde{x} \sin \tilde{y} \\ 0 \end{bmatrix} \\
 &+ A_3 \cos 2k_z z \begin{bmatrix} \cos \tilde{x} \sin \tilde{y} \\ \sin \tilde{x} \cos \tilde{y} \\ -\sqrt{2} \cos \tilde{x} \cos \tilde{y} \end{bmatrix} + A_4 \sin 2k_z z \begin{bmatrix} -\sin \tilde{x} \cos \tilde{y} \\ -\cos \tilde{x} \sin \tilde{y} \\ 0 \end{bmatrix}
 \end{aligned} \tag{3.68}$$

with  $\tilde{A}_R = 2a_R$ ,  $\tilde{A}_1 = 2(a_1 + a_2)$ ,  $\tilde{A}_2 = 2(c - b)$ ,  $\tilde{A}_3 = 2(c + b)$  and  $\tilde{A}_4 = 2(a_1 - a_2)$ . The dimension of the velocity field is  $v_a$ , and therefore the dimension of the analytical velocity field in equation 3.42 is  $v_g$  and gives

$$\begin{aligned} \frac{\mathbf{v}}{v_g} &= \left(1 + \frac{1}{2}\Xi\right) \frac{\mathbf{v}_R}{v_0} \\ &+ \Xi \left( \sin 2k_z z \frac{\tilde{\mathbf{v}}_0}{v_0} + \frac{\sqrt{2}}{8} a k_z \text{Ek}^{-1} \cos 2k_z z \frac{\tilde{\mathbf{v}}_{0z}}{v_0} + \frac{(a k_z)^2 \text{Ek}^{-1}}{8\pi^4 - 4a^2 k_z^2 \pi^2} \frac{\mathbf{v}_\Phi}{v_0} \right) \end{aligned} \quad (3.69)$$

with  $\Xi = E_B \frac{\sqrt{2} 2^{1/4}}{4\pi} \text{Re} \sqrt{\frac{a}{L}}$  and  $\mathbf{v}_\Phi$  as the gradient of  $\Phi$  in  $x$  and  $y$  direction. Here, the derivative in  $z$ -direction is neglected since this term is of higher order in  $a/L$ .  $\Xi$  indicates the ratio of the Lorentz force to the driving force. It gives a measure for the validity of the approximations in the analytical calculation. In the left panel of Figure 3.2, the numerical results agree with the analytical results up to  $\text{Rm} \approx 0.4$  where the ratio of Lorentz to driving force is  $\Xi \approx 1/5$ . The analytical velocity field is composed of the following modes:

$$\begin{aligned} \frac{\mathbf{v}}{v_g} &= B_R \begin{bmatrix} \sin \tilde{x} \cos \tilde{y} \\ -\cos \tilde{x} \sin \tilde{y} \\ \sqrt{2} \sin \tilde{x} \sin \tilde{y} \end{bmatrix} + B_1 \sin 2k_z z \begin{bmatrix} -\cos \tilde{x} \sin \tilde{y} \\ \sin \tilde{x} \cos \tilde{y} \\ \sqrt{2} \cos \tilde{x} \cos \tilde{y} \end{bmatrix} \\ &+ B_3 \cos 2k_z z \begin{bmatrix} 0 \\ 0 \\ -\sqrt{2} \cos \tilde{x} \cos \tilde{y} \end{bmatrix} + B_4 \sin 2k_z z \begin{bmatrix} -\sin \tilde{x} \cos \tilde{y} \\ -\cos \tilde{x} \sin \tilde{y} \\ 0 \end{bmatrix}. \end{aligned} \quad (3.70)$$

The amplitudes of the different modes of the numerical simulations and the analytic calculation are plotted over  $\text{Ek}$  in Figure 3.3. The symbols are again data points of the simulations and the lines represent the amplitudes of the analytical result. At  $\text{Rm} = 0.3$  (see left hand side of Fig. 3.3), the amplitudes  $A_R$  and  $A_1$  split in rotationally dependent and constant part. The constant part of both matches quite well with the analytical values  $B_R$  and  $B_1$ . The corresponding amplitudes  $A_3$  and  $A_4$  of the rotationally dependent solutions  $B_3$  and  $B_4$  are quite different and show no monotonous behaviour. Only at  $\text{Ek} \approx 10^{-2}$ , the increase might be nearly proportional to  $\text{Ek}^{-1}$ , but the data coverage in this region is not sufficient for verification.

At  $\text{Rm} = 0.7$  (see right hand side of fig. 3.3), however, the  $\text{Ek}$ -dependencies of the analytical and numerical amplitudes ( $A_3, A_4$ ) and ( $B_3, B_4$ ) coincide quite well. Only the amplitude of the respective dominant mode differs from each other. At  $\text{Rm} = 0.7$  the

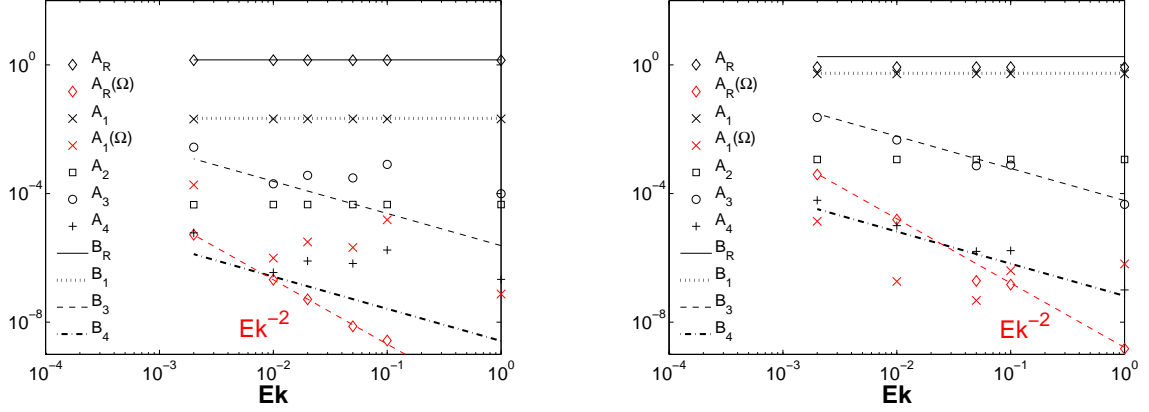


Figure 3.3: Amplitudes of the velocity field at  $Rm = 0.3$  (left) and  $0.7$  (right). The rotational parts of  $A_R$  and  $A_1$  are colored red.

magnetic energy of the corresponding simulation is already significantly higher than the solution of the analytical result (cf. fig. 3.2 (left)). In both cases, the dominant mode is dependent on  $Ek^{-2}$ , which must come from terms, which have been neglected in the analytical approach.

The modes of the mean magnetic field are only dependent on  $z$ . The  $z$ -component is zero.

$$\begin{aligned}
 a_{x,112} &= a_1 + ib_1 \\
 a_{x,118} &= a_1 - ib_1 \\
 a_{x,114} &= -a_2 - ib_2 \\
 a_{x,116} &= -a_2 + ib_2 \\
 a_{y,112} &= -b_1 + ia_1 \\
 a_{y,118} &= -b_1 - ia_1 \\
 a_{y,114} &= -b_2 + ia_2 \\
 a_{y,116} &= -b_2 - ia_2
 \end{aligned} \tag{3.71}$$

with

$$kx_1 = ky_1 = 0 \quad kz_2 = \frac{2\pi}{L} \quad kz_4 = \frac{6\pi}{L} \tag{3.72}$$

$$kz_8 = -\frac{2\pi}{L} \quad kz_6 = -\frac{6\pi}{L} \tag{3.73}$$

$$\tag{3.74}$$

and gives the following magnetic field

$$\mathbf{B}_{num} = C_1 \begin{bmatrix} \cos(k_z z - \arctan(\frac{b_1}{a_1})) \\ \sin(k_z z - \arctan(\frac{b_1}{a_1})) \\ 0 \end{bmatrix} + C_2 \begin{bmatrix} -\cos(3k_z z - \arctan(\frac{a_2}{b_2})) \\ \sin(3k_z z - \arctan(\frac{a_2}{b_2})) \\ 0 \end{bmatrix} \quad (3.75)$$

with  $C_1 = \sqrt{4a_1^2 + 4b_1^2}$  and  $C_2 = \sqrt{4a_2^2 + 4b_2^2}$ . The dimension of the magnetic amplitude is  $\sqrt{\rho\mu_0}v_a$ . With the corresponding dimension  $\sqrt{\rho\mu_0}v_g$ , the equations 3.60 and 3.43 yield the analytical dimensionless magnetic field

$$\begin{aligned} \tilde{\mathbf{B}} &= \frac{\epsilon\hat{B}_1}{\sqrt{\rho\mu_0}v_g} \begin{bmatrix} \cos kz \\ \sin kz \\ 0 \end{bmatrix} + D_1 \begin{bmatrix} -\cos 3kz \\ \sin 3kz \\ 0 \end{bmatrix} + D_2 \begin{bmatrix} \sin 3kz \\ \cos 3kz \\ 0 \end{bmatrix} \\ &= \frac{\epsilon\hat{B}_1}{\sqrt{\rho\mu_0}v_g} \begin{bmatrix} \cos kz \\ \sin kz \\ 0 \end{bmatrix} + D_3 \begin{bmatrix} \sin(3k_z z - \arctan(\frac{D_1}{D_2})) \\ \cos(3k_z z - \arctan(\frac{D_1}{D_2})) \\ 0 \end{bmatrix} \end{aligned} \quad (3.76)$$

with  $D_3 = \sqrt{D_1^2 + D_2^2}$  and

$$\begin{aligned} D_1 &= \frac{1}{64\pi^2} E_{B,1}^{3/2} \text{Rm Re} \\ D_2 &= \frac{1}{512\pi^5} \frac{(\sqrt{2}\pi^2 + \sqrt{2}k^2 a^2 - a\pi k)}{2\pi^2 + a^2 k^2} E_{B,1}^{3/2} \text{Ek}^{-1} \text{Re Rm } ak_z \end{aligned} \quad (3.77)$$

The magnetic energy of the different modes and the total magnetic energy of the numerical simulations are plotted in Figure 3.4 at  $\text{Rm} = 0.3$  and  $0.7$ . At both  $\text{Rm}$ , the main contribution to the total magnetic energy is given by the energy of the dominant mode. The amplitude of the magnetic energy in third order at  $\text{Rm} = 0.3$  is 6 orders of magnitude smaller. Due to this small amplitudes, the development has no smooth increase. The absolute saturated state may not yet be reached within this numerical accuracy. The striking point, however, is that both first and third order show a rotational dependence of  $\sim \text{Ek}^{-2}$ , which is contrary to the analytical result.

According to the assumption of equation 3.39, the phase shift  $\arctan(a_1/b_1)$  in equation 3.75 has to be time dependent  $\partial_t \arctan(a_1/b_1) = \omega_{ph,n}$  and has the dimension  $v_a/a$ . Equation 3.41 then becomes

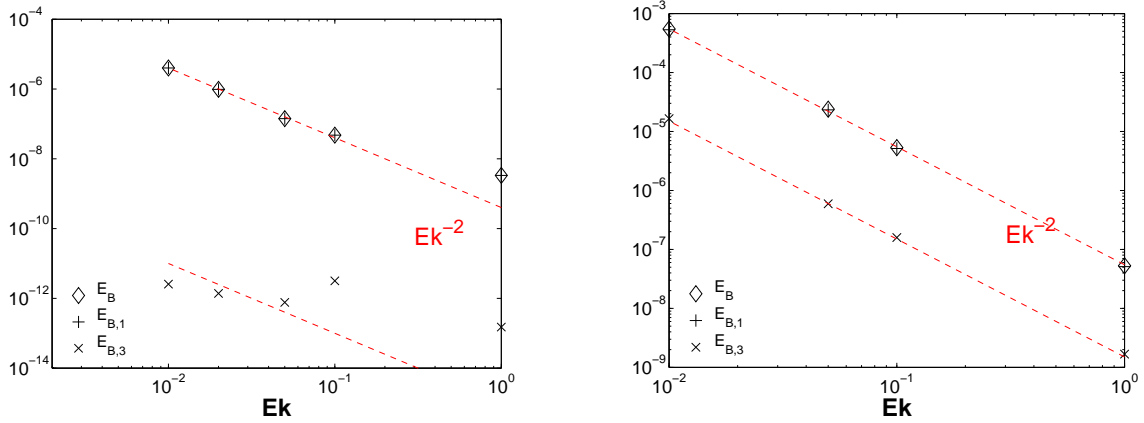


Figure 3.4: Absolute amplitudes of the rotationally dependent part of the magnetic Energy  $|E_B(\text{Ek} = \infty) - E_B(\text{Ek})|$  and the respective parts in first  $|E_{B,1}(\text{Ek} = \infty) - E_{B,1}(\text{Ek})|$  and third order  $|E_{B,3}(\text{Ek} = \infty) - E_{B,3}(\text{Ek})|$  at  $\text{Rm} = 0.3$  (left) and  $0.7$  (right).

$$\omega_{ph} = \epsilon^2 v_{ph,2} k_z \frac{a}{v_g} = \frac{\sqrt{2}}{256\pi^5} (ak_z)^2 E_{B,1} \text{Ek}^{-1} \text{Re} \frac{(\sqrt{2}\pi - ak)}{(2\pi^2 + k^2 a^2)} \quad (3.78)$$

Figure 3.5 shows the drift velocity  $\omega_{ph}$  of the dominant mode. Symbols are again numerical results and the lines represent analytical results. On the left side,  $\omega_{ph}$  is plotted against  $\text{Rm} - \text{Rm}_c$  exemplary for  $\text{Ek} = 5 \times 10^{-2}$  and shows a  $\text{Rm} - \text{Rm}_c / \text{Rm}$  dependency for both results. The deviation of the amplitudes is about a factor of 5. For high  $\text{Rm}$ , the drift velocity tends to decrease again. On the right side,  $\omega_{ph}$  is plotted against  $\text{Ek}$  for  $\text{Rm} = 0.295, 0.3$  and  $0.5$ , which all confirm well the  $\text{Ek}$ -dependency obtained by the analytical calculation. This result is no contradiction to the numerical result that  $E_{B,1}$  is rotational dependent with  $\text{Ek}^{-2}$ . The amplitude of the rotationally dependent part of  $E_{B,1}$  is about 8 orders of magnitude lower than the rotationally independent part. The phase drift of the dominant mode, which was originally a necessary supplement to fulfill the solvability condition, was thereby proven to be a real effect.

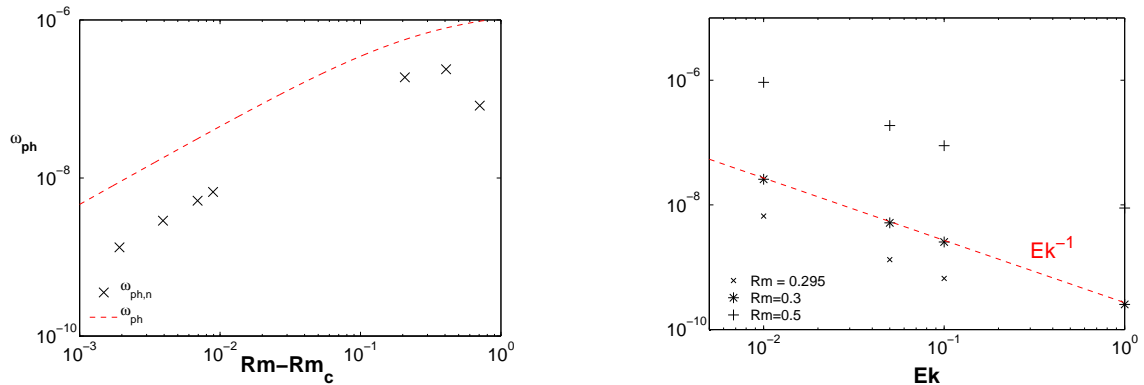


Figure 3.5: Drift velocity  $\omega_{ph}$  plotted over  $\text{Rm}$  at  $\text{Ek} = 5 \times 10^{-2}$  (left) and  $\text{Ek}$  (right).

### 3.2.2 Linearised Navier-Stokes equation

Although the analytical calculation reproduces the saturation level of the magnetic energy up to  $Rm \approx 0.4$  as well as the dependency on  $Ek^{-2}$ , it cannot explain why the magnetic energy is dependent on the rotation rate in the first order of  $Rm - Rm_c$ . Besides, the  $Ek$ -dependency of the perturbed velocity field modes in  $v_2$  is not clear either. With  $Re = 10$ , the ratio of inertial forces to diffusion might be too large so that the numerical model including the advection term is not well approximated by the analytical approach. Therefore, the simulations were repeated with the linearised Navier-Stokes equation in order to test the effect of the advection term on the results and, eventually give possible reasons for the  $Ek$ -dependency to appear in the first order of  $(Rm - Rm_c)$ . Taking the same dimensionless parameters, the Navier-Stokes equation reads

$$\partial_t \mathbf{v} = -\nabla p + \frac{1}{Re} \nabla^2 \mathbf{v} + \mathbf{F} + (\nabla \times \mathbf{B}) \times \mathbf{B} - 2 \frac{1}{Re Ek} (\hat{e}_z \times \mathbf{v}) \quad (3.79)$$

with the same Reynolds number  $Re = v_a a / \nu = 1$  and the Ekman number  $Ek = \nu / \Omega a^2$ . The induction equation does not change and the expressions of the analytical result remain the same.

### Comparison of the numerical and analytical results

The upper left panel of Figure 3.6 shows the saturated magnetic energy plotted over  $Rm$ . Both graphs agree quite well up to  $Rm \approx 0.4$ . The upper right plot shows the absolute difference of the magnetic energy in the non-rotating system compared to the rotating one at different  $Ek$ . The exponent  $Ek^{-2}$  matches the numerical results also very nicely. The corresponding amplitudes of each set of simulations of the upper right panel are plotted against  $(Rm - Rm_c)$  in the lower panel. The amplitudes show a development of  $(Rm - Rm_c)/Rm$  (red dashed line) up to  $Rm \approx 0.31$ , which is about 5% overcritical and a little bit higher than in the non-linear simulations. In this region, the magnetic energy increases with  $Ek$ , whereas for  $Rm > 0.31$  the magnetic energy decreases with  $Ek$ . At high  $Rm$ , however, the amplitude of the rotationally dependent part decreases very quickly. In the end, the rotationally dependent part of  $E_B$  still appears in the first order of  $(Rm - Rm_c)/Rm$ .

In the left panel of Figure 3.7, the drift velocity  $\omega_{ph}$  is plotted against  $Rm - Rm_c$ . Up to  $Rm \approx 0.31$ , it deviates from the analytical prediction by a factor of five. The right panel shows the rotationally dependency of the amplitudes at  $Rm = 0.295 \dots 0.305$ , which are proportional to  $Ek^{-1}$ . At high  $Rm$ , the drift velocity tends to zero.

Figure 3.8 shows the development of the amplitudes of the velocity field of the numerical simulations and the analytical expressions. Without the non-linear term in the Navier-Stokes equation at  $Rm = 0.3$  all numerical amplitudes coincide with the corresponding analytical amplitudes. At both  $Rm$  the amplitudes of the dominant modes  $A_R$  and  $A_1$  have an additional term that is rotationally dependent on  $Ek^{-2}$ .

In Figure 3.9, the magnetic energy of the two modes  $\bar{B}_1$  and  $\bar{B}_3$  is plotted over  $Ek$ . In both cases it increases with  $Ek^{-2}$ , whereas the dominant mode  $\bar{B}_1$  is six orders of magnitude larger than  $\bar{B}_3$  at  $Rm = 0.3$  and only two orders of magnitude at  $Rm = 0.7$ . The dominant mode  $\bar{B}_1$ , in turn, is responsible for the amplitude  $A_R$  and  $A_1$ . They are consistently proportional to  $\hat{B}_1^2$  due to the Lorentz force and therewith  $\sim Ek^{-2}$ , like it is denoted by the red dashed line in Figure 3.8. The question remains as to how the rotational dependence enters the dominant mode in the first place, since  $A_R$  and  $A_1$  define the amplitude of  $F_2$  and therewith the amplitude of the dominant mode.

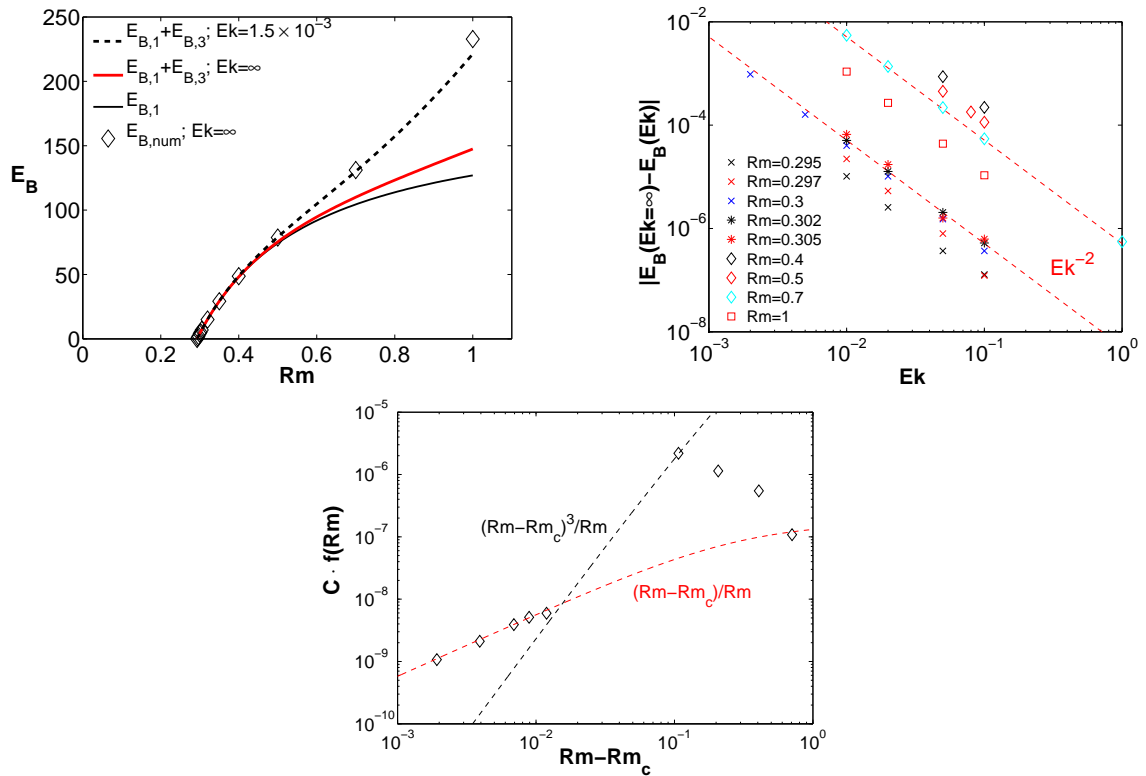
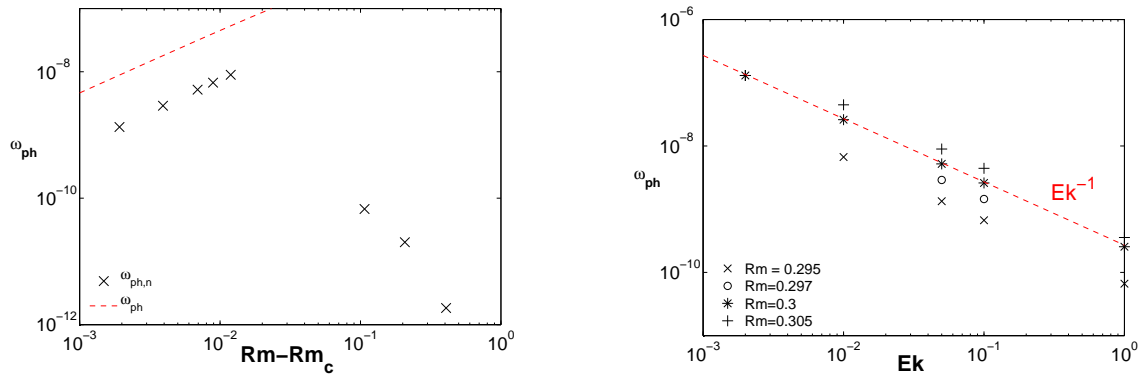
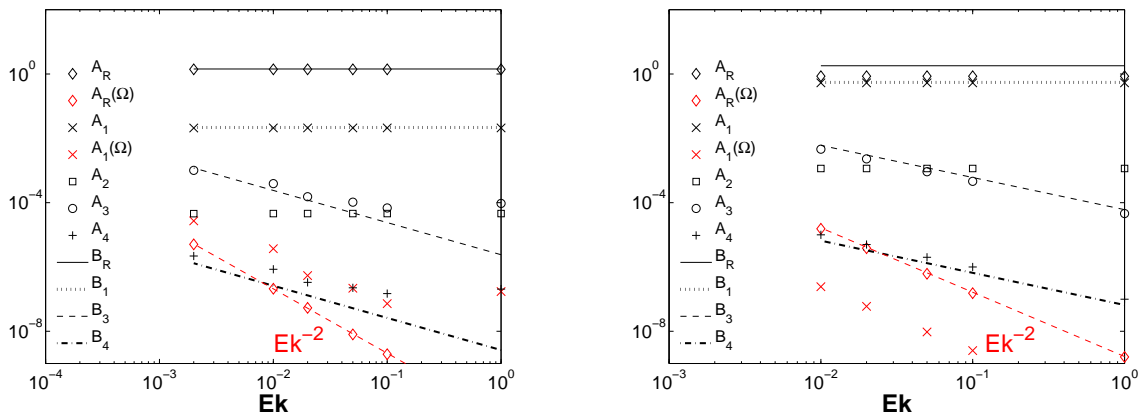
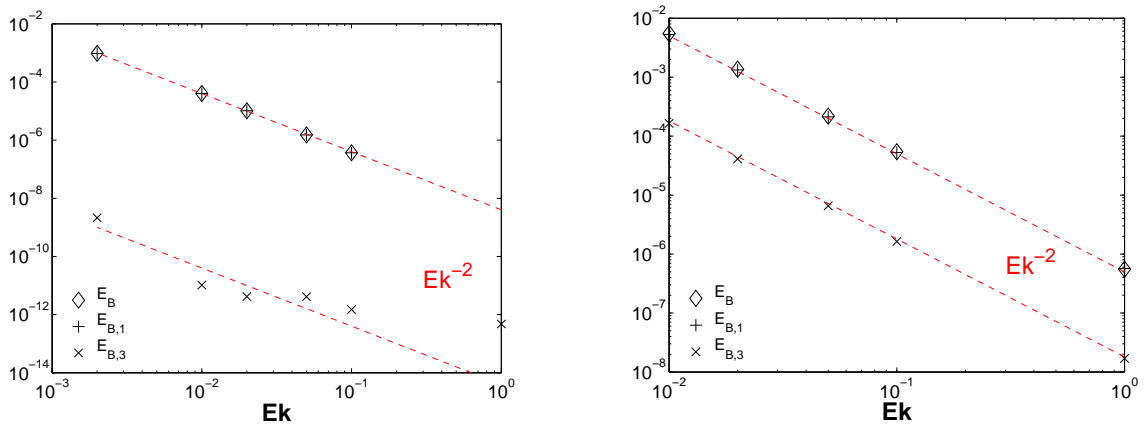


Figure 3.6: In the left panel  $E_{B,num}$  is plotted over  $Rm$  together with the analytical results of the magnetic energy of first order  $E_{B,1}$  (black), the total magnetic energy  $E_B$  without rotation (red) and at  $Ek = 1.5 \times 10^{-3}$ . In the middle figure the absolute amplitude of the rotationally dependent part of the magnetic energy  $|E_B(Ek = \infty) - E_B(Ek)|$  is plotted over  $Ek$ . The red dashed lines indicate a proportionality to  $Ek^{-2}$ . The amplitude of each fit in the middle Figure is plotted over  $Rm$  on the right hand side and shows a proportionality to  $Rm - Rm_c/Rm$  (red dashed). The corresponding analytical expression gives  $\sim (Rm - Rm_c)^3/Rm$  (black dashed).


 Figure 3.7: Drift velocity  $\omega_{ph}$  plotted over  $Rm$  at  $Ek = 5 \times 10^{-2}$  (left) and  $Ek$  (right).

 Figure 3.8: Amplitudes of the velocity field at  $Rm = 0.3$  (left) and  $0.7$  (right). The rotational parts of  $A_R$  and  $A_1$  are colored red.

 Figure 3.9: Absolute amplitudes of the rotationally dependent part of the magnetic Energy  $|E_B(Ek = \infty) - E_B(Ek)|$  and the respective parts in first  $|E_{B,1}(Ek = \infty) - E_{B,1}(Ek)|$  and third order  $|E_{B,3}(Ek = \infty) - E_{B,3}(Ek)|$  at  $Rm = 0.3$  (left) and  $0.7$  (right).

One explanation must be that any other terms, which were neglected in the induction equation, in the Lorentz force or any derivatives in  $z$  in the Navier-Stokes equation must be responsible for a rotationally dependent term in  $A_R$  or  $A_1$ , which might be covered by the  $Ek^{-2}$ -term and becomes invisible in that way.

Since Figure 3.8 is just the result of equation 3.24, at least the Lorentz force term can be tested for correctness. By taking the amplitudes of the  $\Omega$ -dependent parts of  $E_{B,1}$  of the numerical simulation and recalculate those parts of  $A_R$  and  $A_1$  which are proportional to  $\sim Ek^{-2}$  with equation 3.42. Obviously, both amplitudes are equal to  $\epsilon^2\gamma$  except for a factor of  $1/2$ . The recalculation of  $A_R$  and  $A_1$  gives a discrepancy of one order of magnitude to the original obtained amplitudes in the numerical simulation, which makes the Lorentz force term suspicious to be not well approximated.

### 3.2.3 Outlook

Apparently, the magnetic energy is already dependent on  $\Omega$  in the first order of  $\epsilon$ , as it can be seen on the right side of Figure 3.6. However it contradicts the analytical results. Especially the approximated Lorentz force term is not capable of reproducing the amplitudes of the velocity field which are generated by the dominant mode. Since the amplitude of the responsible term is quite low  $\sim 10^{-7}$ , it is possible that terms which were neglected in equation 3.8, 3.14 or 3.24 could be responsible for  $\Omega$  to appear in the first order of the magnetic energy. This means that  $F_2$  has to be rotationally dependent.  $F_2$  in turn is defined by the solvability condition (eq. 3.34). Only the amplitudes of two modes of  $v_2$

$$v_2 = a_R \mathbf{v}_R + a_{v1} \sin 2k_z z \tilde{\mathbf{v}}_0 \quad (3.80)$$

contribute to the amplitude of  $F_2$ , since both amplitudes  $a_R$  and  $a_{v1}$  merge in the amplitude of the first term in equation 3.37, which belongs to the mode  $[\cos k_z z \sin k_z z \ 0]$ . All other terms become zero on average over the  $(x, y)$ -plane or appear in amplitudes of other modes. In order to get the  $\Omega$ -dependency in first order of  $(\text{Rm} - \text{Rm}_c)/\text{Rm}$ ,  $\Omega$  must appear in these two modes  $\mathbf{v}_R$  and  $\tilde{\mathbf{v}}_0$ .

### Expansion of the MHD equation in $a/L$

The only parameter that was left out in the perturbation expansion is  $a/L$ . Starting with equation 3.8, where  $(\mathbf{v} \cdot \nabla) \overline{\mathbf{B}}$  appears in first order in  $a/L$ , which gives

$$\lambda \nabla^2 \mathbf{b} = -(\overline{\mathbf{B}} \cdot \nabla) \mathbf{v} + (\mathbf{v} \cdot \nabla) \overline{\mathbf{B}} \quad (3.81)$$

and  $\mathbf{b}$ , up to second order in  $(a/L)$ , becomes

$$\mathbf{b} \approx \frac{1}{2\lambda} \left(\frac{a}{\pi}\right)^2 [(\overline{\mathbf{B}} \cdot \nabla) \mathbf{v} - (\mathbf{v} \cdot \nabla) \overline{\mathbf{B}}] + \frac{1}{4\lambda} \left(\frac{a}{\pi}\right)^4 (\partial_z^2 \overline{\mathbf{B}} \cdot \nabla) \mathbf{v}. \quad (3.82)$$

The result of the second term, which is in first order of  $\epsilon$ , adds an additional diffusion term  $\sim \partial_z^2 \overline{\mathbf{B}}$  to the original solutions and has already been worked out by Tilgner (2004). The kinematic dynamo onset slightly changes to

$$\text{Rm}_c = \frac{8\pi^2 a k_z}{2\sqrt{2\pi} - a k_z}. \quad (3.83)$$

Considering  $\mathbf{b} = \mathbf{b}_0 + (a/L)\mathbf{b}_1 + (a/L)^2\mathbf{b}_2$  the Lorentz-force term splits up into several parts, whereas the rotation of vector terms including  $\mathbf{b}$  always generates contributions to the order  $(a/L)^{n+1}$  and  $(a/L)^n$ . Only  $(\nabla \times \mathbf{b}) \times \mathbf{b}$  is not considered, because  $|\mathbf{b}| \approx \frac{v_g a}{\lambda} |\overline{\mathbf{B}}|$ , and thus, this term is of higher order in  $Rm$ . The contributions to the Lorentz force  $\mathbf{L}$  are

$$\begin{aligned}
 \nabla \times [(\nabla \times \mathbf{b}_0) \times \overline{\mathbf{B}}] & \quad O(1), a/L, (a/L)^2 \\
 \nabla \times [(\nabla \times \mathbf{b}_1) \times \overline{\mathbf{B}}] & \quad a/L, (a/L)^2, \dots \\
 \nabla \times [(\nabla \times \mathbf{b}_2) \times \overline{\mathbf{B}}] & \quad (a/L)^2, \dots \\
 \nabla \times [(\nabla \times \overline{\mathbf{B}}) \times \mathbf{b}_0] & \quad a/L, (a/L)^2 \\
 \nabla \times [(\nabla \times \overline{\mathbf{B}}) \times \mathbf{b}_1] & \quad (a/L)^2, \dots
 \end{aligned} \tag{3.84}$$

In equation 3.24, terms including derivatives of  $\mathbf{v}_2 = [v_1, v_2, v_3]$  with respect to  $z$  also contributes to orders in  $(a/L)^{n+1}$ . Solely terms with derivatives in  $z$ -direction including  $\Omega$  are unchanged, since  $\Omega$  is supposed to get large and the partial differential equation becomes,

$$\begin{aligned}
 0 &= \partial_x^2 \partial_y v_3 + \partial_y^3 v_3 - \frac{a}{L} \partial_x^2 \partial_z v_2 - \frac{a}{L} \partial_y^2 \partial_z v_2 + 2\partial_z v_1 \Omega / \nu + \mathbf{F}_1 + \mathbf{L}_1 \\
 0 &= \frac{a}{L} \partial_x^2 \partial_z v_1 + \frac{a}{L} \partial_y^2 \partial_z v_1 - \partial_x^3 v_3 - \partial_y^2 \partial_x v_3 + 2\partial_z v_2 \Omega / \nu + \mathbf{F}_2 + \mathbf{L}_2 \\
 0 &= \partial_x^3 v_y + \partial_y^2 \partial_x v_y - \partial_x^2 \partial_y v_x - \partial_y^3 v_x - 2\partial_x v_x \Omega / \nu - 2\partial_y v_y \Omega / \nu + \mathbf{F}_3 + \mathbf{L}_3.
 \end{aligned}$$

The force term  $\mathbf{F}$  only appears in zeroth order of  $a/L$ . The velocity field  $\mathbf{v}_2$  is expanded in orders of  $a/L$ :

$$\mathbf{v}_2 = \mathbf{v}_{2,0} + \frac{a}{L} \mathbf{v}_{2,1} + \left(\frac{a}{L}\right)^2 \mathbf{v}_{2,2} + \dots \tag{3.85}$$

The solution of  $\mathbf{v}_2$  in zeroth order is equal to equation 3.31. In first order of  $a/L$ , the rotationally dependent part of  $\mathbf{v}_{2,0}$  reappears with slightly changed amplitudes

$$\mathbf{v}_{2,1} = \frac{\gamma}{2\pi^2 + a^2 k_z^2} \frac{\sqrt{2}}{8} \left(\frac{a}{\pi}\right)^3 \frac{k_z^3 \Omega}{\nu} \cos 2k_z z \tilde{\mathbf{v}}_{0z} + \nabla \Phi_1 \tag{3.86}$$

with

$$\Phi_1 = \frac{-1}{4\left(\frac{\pi}{a}\right)^4 + 4\left(\frac{\pi}{a}\right)^2 k^2 + k^4} \frac{\sqrt{2}}{64} \left(\frac{a}{\pi}\right)^5 \frac{v_0 \Omega k_z^4 \hat{\mathbf{B}}_1^2}{v^2 \lambda \mu_0 \rho} \sin 2k_z z \cos \frac{2\pi}{a} y \cos \frac{2\pi}{a} x. \quad (3.87)$$

Finally, even in second order, the new terms in the Lorentz force do not generate any new modes in  $\mathbf{v}_2$  and  $\mathbf{v}_{2,2}$  becomes

$$\mathbf{v}_{2,2} = A_{2,R} \mathbf{v}_R + (A_{2,1} \sin 2k_z z + A_{2,2} \Omega \cos 2k_z z) \tilde{\mathbf{v}}_{0z} + \nabla \Phi_2, \quad (3.88)$$

whereas  $\Phi_2$  again has the form

$$\Phi_2 = A_{2,\Phi} \Omega \sin 2k_z z \cos \frac{2\pi}{a} y \cos \frac{2\pi}{a} x. \quad (3.89)$$

The amplitudes  $A_{2,R}$ ,  $A_{2,1}$ ,  $A_{2,2}$  and  $A_{2,\Phi}$  are not important. The results, however, show that none of the additional Lorentz force terms generate a new rotationally dependent mode. By calculating the induction terms of equation 3.32,  $F_2$  still remains rotationally independent. The last terms, that remain are those in equation 3.8 which are non-linear in  $\mathbf{v}$ :  $\{\nabla \times (\mathbf{b} \times \mathbf{v}) - \langle \nabla \times (\mathbf{b} \times \mathbf{v}) \rangle\}$ . These terms combine small-scale magnetic and velocity induction effects. At this point, the analytical possibilities are exhausted.

### Advanced dealiasing and the fluctuative magnetic field

According to the dealiasing of higher wavenumbers, it is possible to cut out modes with admitted wavenumbers but small amplitudes. In this way the velocity field in the numerical simulation can be modified according to the analytical expression in equation 3.69. By taking  $c = d = 0$  the only non-zero amplitudes in equation 3.68 are  $A_R, A_1$  and  $A_4$  of which  $A_4$  is rotationally dependent. Additionally, the fields have a dealiasing in  $k_{x,y} > 2\pi/a$  and  $k_z > 4\pi/d$ . Simulations with this kind of prepared velocity field show a rotational dependence of the magnetic field, which actually only consists of the dominant mode  $\bar{\mathbf{B}}_1$  and the fluctuating part  $\mathbf{b}$ . The fluctuative part of the magnetic field has the following Fourier amplitudes

$$\begin{aligned}
 a_{x,222} &= a_1 + ib_2 \\
 a_{x,282} &= b_1 - ia_2 \\
 a_{x,228} &= a_1 - ib_2 \\
 a_{x,288} &= b_1 + ia_2 \\
 \\ 
 a_{y,222} &= -a_2 - ib_1 \\
 a_{y,282} &= b_2 - ia_1 \\
 a_{y,228} &= -a_2 + ib_1 \\
 a_{y,288} &= b_2 + ia_1 \\
 \\ 
 a_{z,222} &= \sqrt{2}(-b_1 + ia_1) \\
 a_{z,282} &= \sqrt{2}(-a_1 - ib_1) \\
 a_{z,228} &= \sqrt{2}(b_1 + ia_1) \\
 a_{z,288} &= \sqrt{2}(a_1 - ib_1)
 \end{aligned} \tag{3.90}$$

which gives by only considering those amplitudes with index 1

$$\mathbf{b}_{num} = \left[ \begin{array}{l} (4(a_1 + b_1) \cos \tilde{x} \cos \tilde{y} - 4(a_1 - b_1) \sin \tilde{x} \sin \tilde{y}) \cos k_z z \\ -(4(a_1 + b_1) \cos \tilde{x} \cos \tilde{y} + 4(a_1 - b_1) \sin \tilde{x} \sin \tilde{y}) \sin k_z z \\ \sqrt{a_1^2 + a_2^2} \sqrt{2} \cos \tilde{x} \sin \tilde{y} \cos(k_z z + \varphi) + \sqrt{a_1^2 + a_2^2} \sqrt{2} \sin \tilde{x} \cos \tilde{y} \sin(k_z z + \varphi) \end{array} \right]$$

with  $\tilde{x} = 2\pi x/a$  and  $\tilde{y} = 2\pi y/a$ . Contrary to the analytical expression the  $z$ -component has a phase  $\varphi = \arctan((a_1 + b_1)/(b_1 - a_1))$ . Due to this phase shift, the induction term gives

a rotationally dependent contribution to the dominant mode, which can be confirmed by the analytical calculation. With the prepared velocity field and the fluctuative magnetic field the projection of the induction term yield

$$\int \nabla \times (\mathbf{b}_{num} \times \mathbf{v}_{num}) \cdot \bar{\mathbf{B}}_1 dV \sim \Omega \sin \varphi. \quad (3.91)$$

The phase in the  $z$ -component is therefore responsible for the  $\Omega$ -dependency of the magnetic field in first order. Since  $\mathbf{b}$  is deduced from equation 3.8, it is most likely that the nonlinear terms  $\nabla \times (\mathbf{b} \times \mathbf{v})$  and  $\langle \nabla \times (\mathbf{b} \times \mathbf{v}) \rangle$  are responsible for the phase  $\varphi$ . Incorporating this phase shift in the analytical calculations, yields

$$F_2 = \frac{3}{4} \frac{v_0 \hat{B}_1^2}{\lambda \mu_0 \rho} \left( 1 + \frac{\sqrt{2}}{24\pi} \frac{ak_z}{2\pi^2 + a^2 k_z^2} \text{Ek}^{-1} \right) \quad (3.92)$$

and the magnetic energy becomes

$$E_{B,1} = \frac{(\text{Rm} - \text{Rm}_c)}{\text{Rm Re}} \frac{8\pi}{3} 2^{-1/4} \sqrt{\frac{L}{a}} \left( 1 + \frac{\sqrt{2}}{24\pi} \frac{ak_z}{2\pi^2 + a^2 k_z^2} \text{Ek}^{-1} \right)^{-1}. \quad (3.93)$$

This result, however, gives a decrease of the magnetic energy for increasing rotation rates which is in contrast to the numerical results at  $\text{Rm} < 0.4$ . In order to get the proportionality of the analytical result, the force term in second order of  $\epsilon$  should be  $F_2 \sim \hat{B}_1^2 / (1 + \text{Ek}^{-2})$ . Nevertheless the case that the magnetic energy is lowered by increasing the rotation can be observed for  $\text{Rm} > 0.4$ .

### 3.3 Conclusion

The G. O. Roberts flow is a simple, two-dimensional vector field, which is similar to many large-scale helical flows such as for example rotating convective flows generated in celestial bodies. It is therefore a useful flow for the analytical investigation of basic characteristics of dynamos with the help of mean field theory and weakly non-linear theory. In addition, numerical simulations including all non-linear terms were performed in the same parameter regime. This allows for a comparison between numerical and analytical results and thus for testing the applicability of the analytical approximation.

The analytical calculation shows that in the first order of  $Rm - Rm_c$ , the saturation level of the magnetic energy is independent of the rotation. It reproduces the magnetic energy of the simulations without rotation up to  $Rm \approx 0.4$  quite well. At that point, the ratio of the amplitudes in  $\mathbf{v}_2$ , which occur due to the Lorentz force to those generated by the driving forces, is  $\Xi \approx 1/5$ . Assuming that the aspect ratio of the flow columns is of order 10 in the Earth's interior and  $L$  is the Earth's diameter, one obtains a ratio of approximately  $\Xi \approx 10^3$  with  $Re = 10^9$ ,  $Rm = 100$  and magnetic field strength of the dipole of  $\hat{B}_1 \approx 100\mu T$ . The same ratio is expected in experiments, where  $Rm$  is the same, but  $E_B$  is two orders of magnitude higher and  $Re$  is two orders of magnitude lower. With the aspect ratio taken in this study one obtains  $\Xi \approx 0.3$  for both systems, which is almost equal to the ratio in the numerical simulation  $\Xi \approx 0.25$ .

In third order, the magnetic energy is proportional to  $\sim Ek^{-2}$ . The condition for solvability predicts a drift velocity of the dominant mode with a rotational dependence of  $\sim Ek^{-1}$ , which was confirmed by the numerical simulations. For large  $Rm$ , however, the drift velocity tends towards zero. The saturation level of the magnetic energy in the numerical simulations shows quite a robust dependence on  $\sim Ek^{-2}$  up to  $Rm = 1$ , whereas the amplitude of the rotationally dependent part tends towards zero for higher  $Rm$ . The results of Reiners et al. (2009) found an increase of the magnetic flux proportional to the rotational timescale for slowly rotating objects and a regime of fast rotating objects where the magnetic flux is independent of the rotation rate.

In addition, the magnetic energy of the analytical solution is proportional to  $(a/L)^2$ . In rotating plane layer convection, the aspect ratio is dependent on  $\sim Ek^{1/3}$  near the onset of Rayleigh-Bernard convection, so that the transfer of these results to convection-driven systems should be between  $\sim Ek^{-4/3}$  and  $\sim Ek^{-2}$ . At least the latter power law would agree with evolution in slowly rotating stars (Reiners et al. 2009). The only hint for a possible saturation of the magnetic energy is given by the numerical results, where the rotationally dependent part of the magnetic energy tends towards zero for high  $Rm$ .

In global simulations many forces are incorporated in order to make the system most realistic. The saturation level of the magnetic energy in global simulations of planetary

or stellar dynamos in spherical geometry depends on many parameters, so that a clear exponent could not yet be found (Christensen and Aubert 2006). The ratio of the ohmic dissipation to the total dissipation is a crucial factor and defines the state, at which the magnetic energy at least becomes independent of the rotation rate. This state is reached when all the energy is dissipated by ohmic loss (Schrinner 2013).

The model and its geometries are quite different and the only thing they have in common is that their flow exhibits helicity, which plays a major role in the dynamo process with an dominant  $\alpha$ -effect in the dynamo mechanism. An interesting extension of this work would be the evolution of the magnetic energy in a rotating spherical shell with free slip boundaries. The G.O. Roberts flow would be generated by a volume force like it was already applied by Tilgner (1997). The only restriction would be the resolution, which limits the aspect ratio. Thus, values of  $Rm$  which are as low as in these simulations could not be reached. The intermediate regime could be covered with the numerical results of periodic box simulations at lower aspect ratios.

The dynamo generation in rotating Rayleigh-Bénard convection has been investigated by (Tilgner 2012). Rotating convection in a plane layer is more similar to the cartesian geometry of the periodic box, but apart from the vortices of the flow, the dynamo generation here is more related to the Ekman layers that occur at the boundaries and which are sensitive to the rotation rate as well. The magnetic energy develops in two different ways depending on whether a geostrophic or magnetostrophic balance is predominant. In the magnetostrophic balance, the magnetic energy is proportional to  $\sim Ek^{-1/3}$ , whereas it is  $\sim Ek^{-5/6}$  in the geostrophic balance. Since the Lorentz force near the onset is rather weak, the conditions in the geostrophic balance would be more appropriate for a comparison to the periodic box simulations. Reconsidering a dependence of the aspect ratio of the periodic box on  $Ek^{1/3}$ , the exponent of the analytical result and the geostrophic balance are approximately equal to one.

Nevertheless, the order in which  $Ek^{-2}$  appears in the saturated magnetic energy is  $Rm - Rm_c$ . Since the amplitude is quite small, it is obvious that some of the neglected terms must be responsible for the rotation to appear in the first order. Therefore,  $\mathbf{v}_2$  in the Navier-Stokes equation in second order of  $Rm - Rm_c$ , which is responsible for the saturating process, is expanded in orders  $a/L$ . This includes terms with derivatives of  $\mathbf{v}_2$  in  $z$  and the Lorentz force, in which the fluctuative part of the magnetic field  $\mathbf{b}$  has to be extended up to the second order in  $a/L$ . Nevertheless, this step does not change the order, in which the saturated magnetic energy is dependent on the rotation; therefore, the two remaining terms which can be responsible are  $\{\nabla \times (\mathbf{b} \times \mathbf{v}) - \langle \nabla \times (\mathbf{b} \times \mathbf{v}) \rangle\}$ .

Comparing analytical and numerical expressions for the fluctuative magnetic field yield that the  $z$ -component of  $\mathbf{b}$  has a phase shift in  $z$ -direction. By this phase, it is possible to get a rotationally dependent dominant mode. This shows that  $\mathbf{b}$  is responsible for the

deviation of the analytical results from the numerical results. The according modification of the analytical calculation, however, can not reproduce the numerical results. Thus, the amplitude of  $\mathbf{b}$  has to be dependent on  $\Omega$  as well. Due to the non-linear terms, a further investigation of the amplitude of  $\mathbf{b}$ , from which  $F_2$  and  $E_{B,1}$  are deduced, becomes difficult. A positive proof by modified numerical simulations could not be made.

# Bibliography

- D. J. Acheson. *Elementary Fluid Dynamics*. Oxford University Press, 1990.
- R. A. Bayliss, S. B. Forest, M. D. Nornberg, E. J. Spence, and P. W. Terry. Numerical simulations of current generation and dynamo excitation in a mechanically forced turbulent flow. *Phys. Rev. E*, 75:026303, 2007.
- M. Berhanu, G. Verhille, J. Boisson, B. Gallet, C. Gissinger, S. Fauve, N. Mordant, F. Petrelis, M. Bourgoin, P. Odier, J. F. Pinton, N. Plihon, S. Aumaitre, A. Chiffaudel, F. Daviaud, B. Dubrulle, and C. Pirat. Dynamo regimes and transitions in the vks experiment. *European Physical Journal B*, 77(4):459–468, 2010.
- D. Biskamp. *Magnetohydrodynamic Turbulence*. Cambridge University Press, 2003.
- A. Brandenburg. Large-scale dynamos at low magnetic prandtl numbers. *Astrophys. J.*, 697(2):1206–1213, 2009.
- A. Brandenburg and A. Nordlund. Astrophysical turbulence modeling. *Reports on Progress in Physics*, 74(4):046901, 2011.
- A. Brandenburg and K. Subramanian. Astrophysical magnetic fields and nonlinear dynamo theory. *Physics Reports*, 417:1–209, 2005.
- F. H. Busse. A model of the geodynamo. *Geophys J. R. astr. Soc.*, 42:437–459, 1975.
- S. Chandrasekhar. *Hydrodynamic and Hydromagnetic Stability*. Dover Publications, Inc. New York, 1961.
- M Chertkov, G Falkovich, I Kolokolov, and M Vergassola. Small-scale turbulent dynamo. *Phys. Rev. Lett.*, 83(20):4065–4068, 1999.
- U Christensen, P. Olson, and G. A. Glatzmaier. Numerical modelling of the geodynamo: a systematic parameter study. *Geophys J. Int.*, 138:393–409, 1999.

- U. R. Christensen and J. Aubert. Scaling properties of convection-driven dynamos in rotating spherical shells and application to planetary magnetic fields. *Geophys. J. Int.*, 166:97–114, 2006.
- U. R. Christensen, V. Holzwarth, and A. Reiners. Energy flux determines magnetic field strength of planets and stars. *Nature*, 457:167–169, 2009.
- P. A. Davidson. *Turbulence*. Oxford University Press, 2004.
- M. Dudley and R. James. *Proc. R. Soc. Lond. A.*, 425(7):407, 1989.
- S. Fauve and F. Petrelis. Scaling laws of turbulent dynamos. *C. R. Physique*, 8:87–92, 2007.
- K. Finke and A. Tilgner. Simulations of the kinematic dynamo onset of spherical Couette flows with smooth and rough boundaries. *Phys. Rev. E*, 86(1, Part 2):016310, 2012.
- C. A. J. Fletcher. *Computational Techniques for Fluid Dynamics*. Springer-Verlag Berlin Heidelberg New York, 1991.
- A. Gailitis, O. Lielausis, S. Dement'ev, E. Platācis, A. Cifersons, G. Gerbeth, T. Gundrum, F. Stefani, M. Christen, H. Hanel, and G. Will. Detection of a flow induced magnetic field eigenmode in the Riga dynamo facility. *Phys. Rev. Lett.*, 84(19):4365–4368, 2000.
- A. Giesecke, C. Nore, F. Plunian, R. Laguerre, A. Ribeiro, F. Stefani, G. Gerbeth, J. Léorat, and J. L. Guermond. Generation of axisymmetric modes in cylindrical kinematic mean-field dynamos of vks type. *Geophys. Astrophys. Fluid Dyn.*, 104(2-3):249–271, 2010a.
- A. Giesecke, F. Stefani, and G. Gerbeth. Role of soft-iron impellers on the mode selection in the von Karman-sodium dynamo experiment. *Phys. Rev. Lett.*, 104(4):044503, 2010b.
- P. A. Gilman and J. Miller. Dynamically consistent nonlinear dynamos driven by convection in a rotating spherical shell. *Astrophysical Journal Supplement Series*, 46:211–238, 1981.
- G. A. Glatzmaier. Numerical simulations of stellar convective dynamos. i - the model and method. *Journal of Computational Physics*, 55:461–484, 1984.
- G. A. Glatzmaier and P. H. Roberts. A three-dimensional convective dynamo solution with rotating and finitely conducting inner core and mantle. *Nature*, 91:63–75, 1995.
- J. P. Graham, E. G. Blackman, P. D. Mininni, and A. Pouquet. Not much helicity is needed to drive large-scale dynamos. *Phys. Rev. E*, 85(6, Part 2):066406, 2012.

- H. P. Greenspan. *The Theory of Rotating Fluids*. Cambridge University Press, 1968.
- C. Guervilly and P. Cardin. Numerical simulations of dynamos generated in spherical couette flows. *Geophys. Astrophys. Fluid Dynamics*, 104:221–248, 2010.
- R. Hollerbach. Non-axisymmetric instabilities in magnetic spherical couette flow. *Proc. R. Soc. Lond. A*, pages 1–11, 2009.
- R. Hollerbach, M. Junk, and C. Egbers. Non-axisymmetric instabilities in basic spherical couette flow. *Fluid Dynamics Research*, 38:257–273, 2006.
- A. B. Iskakov, A. A. Schekochihin, S. C. Cowley, J. C. McWilliams, and M. R. E. Proctor. Numerical demonstration of fluctuation dynamo at low magnetic prandtl numbers. *Phys. Rev. Lett.*, 98(20):208501, 2007.
- F. Krause and K.-H. Rädler. *Mean-Field Magnetohydrodynamics and Dynamo Theory*. Akademie-Verlag Berlin, 1980.
- S. Lorenzani. *Fluid instabilities in precessing ellipsoidal shells*. PhD thesis, Mathematisch-Naturwissenschaftlichen Fakultäten der Georg-August-Universität zu Göttingen, 2001.
- L. M. Malyskin and S. Boldyrev. Magnetic dynamo action at low magnetic prandtl numbers. *Phys. Rev. Lett.*, 105(21):215002, 2010.
- A. Mangeney and F. Praderie. The influence of convection and rotation on x-ray-emission in main-sequence stars. *Astron. Astrophys.*, 130:143, 1984.
- R. T. Merrill, M. W. McElhinny, and P.L. McFadden. *The Magnetic Field of the Earth*. Academic Press, 1996.
- P. D. Mininni. Inverse cascades and alpha effect at a low magnetic prandtl number. *Phys. Rev. E*, 76(2, Part 2):026316, 2007.
- H. K. Moffatt. *Magnetic Field Generation in Electrically Conducting Fluids*. Cambridge University Press, 1978.
- H. K. Moffatt and M. R. E. Proctor. The role of the helicity spectrum function in turbulent dynamo theory. *Geophysical and Astrophysical Fluid Dynamics*, 21(3-4):265–283, 1982.
- R. Monchaux, M. Berhanu, M. Bourgoin, M. Moulin, Ph. Odier, J. F. Pinton, R. Volk, S. Fauve, N. Mordant, F. Petrelis, A. Chiffaudel, F. Daviaud, B. Dubrulle, C. Gasquet, L. Marie, and F. Ravelet. Generation of a magnetic field by dynamo action in a turbulent flow of liquid sodium. *Phys. Rev. Lett.*, 98(4):044502, 2007.

- J. Morin, J. F. Donati, P. Petit, X. Delfosse, T. Forveille, L. Albert, M. Auriere, R. Cabanac, B. Dintrans, R. Fares, T. Gastine, M. M. Jardine, F. Lignieres, F. Paletou, J. C. Ramirez Velez, and S. Theado. Large-scale magnetic topologies of mid m dwarfs. *Mon. Not. R. Astron. Soc.*, 390(2):567–581, 2008.
- U. Muller and R. Stieglitz. The karlsruhe dynamo experiment. *Nonlinear Processes in Geophysics*, 9(3-4):165–170, 2002.
- H.-C. Nataf, T. Alboussiere, D. Brito, P. Cardin, N. Gagniere, D. Jault, and D. Schmitt. Rapidly rotating spherical couette flow in a dipolar magnetic field: An experimental study of the mean axisymmetric flow. *Physics of the Earth and Planetary Interiors*, 170:60–72, 2008.
- M. D. Nornberg, E. J. Spence, R. D. Kendrick, C. M. Jacobson, and C. B. Forest. Measurements of the magnetic field induced by a turbulent flow of a liquid metal. *Physics of Plasmas*, 13:055901, 2006.
- R. W. Noyes, L. W. Hartmann, S. L. Baliunas, D. K. Duncan, and A. H Vaughn. Rotation, convection, and magnetic activity in lower main-sequence stars. *Astrophys. J.*, 279:763–777, 1984.
- A. Pinter, B. Dubrulle, and F. Daviaud. Kinematic dynamo simulations of von karman flows: application to the vks experiment. *European Physical Journal B*, 74(2):165–176, 2010.
- N. Pizzolato, A. Maggio, G. Micela, S. Sciortino, and P. Ventura. The stellar activity-rotation relationship revisited: Dependence of saturated and non-saturated x-ray emission regimes on stellar mass for late-type dwarfs. *Astron. Astrophys.*, 397(1):147–157, 2003.
- Yu. B. Ponomarenko. Theory of the hydromagnetic generator. *J. Appl. Mech. Tech. Phys.*, 14:775–778, 1973.
- Y. Ponty and F. Plunian. Transition from large-scale to small-scale dynamo. *Phys. Rev. Lett.*, 106(15):154502, 2011.
- Y. Ponty, P. D. Mininni, D. C. Montgomery, Pinton J.-F., H. Politano, and A. Pouquet. Numerical study of dynamo action at low magnetic prandtl numbers. *Phys. Rev. Lett.*, 94:164502, 2005.
- Y. Ponty, P. D. Mininni, J-F Pinton, H. Politano, and A. Pouquet. Dynamo action at low magnetic prandtl numbers: mean flow versus fully turbulent motions. *New Journal of Physics*, 9:296, 2007.

- 
- W. H. Press, S. A. Teukolsky, W. T. Vetterling, and B. F. Flannery. *Numerical Recipes*. Cambridge University Press, 1986.
- A. Reiners, G. Basri, and M. Browning. Evidence for magnetic flux saturation in rapidly rotating stars. *Astrophys. J.*, 692(1):538–545, 2009.
- K. Reuter, F. Jenko, A. Tilgner, and C. B. Forest. Wave-driven dynamo action in spherical magnetohydrodynamic systems. *Phys. Rev. E*, 80:056304, 2009.
- K. Reuter, F. Jenko, and C. B. Forest. Turbulent magnetohydrodynamic dynamo action in a spherically bounded von karman flow at small magnetic prandtl numbers. *New Journal of Physics*, 113:073019, 2011.
- M. Rieutord, S. A. Triana, D. S. Zimmerman, and D. P. Lathrop. Excitation of inertial modes in an experimental spherical couette flow. *Phys. Rev. E*, 86(2, Part 2):026304, 2012.
- G. O. Roberts. Dynamo action of fluid motions with 2-dimensional periodicity. *Phil. Trans. R. Soc. A*, 271(1216):411–454, 1972.
- A. A. Schekochihin, S. C. Cowley, J. L. Maron, and J. C. McWilliams. Critical magnetic prandtl number for small-scale dynamo. *Phys. Rev. Lett.*, 92(5):054502, 2004a.
- A. A. Schekochihin, S. C. Cowley, S. F. Taylor, J. L. Maron, and J. C. McWilliams. Simulations of the small-scale turbulent dynamo. *Astrophys. J.*, 612(1, Part 1):276–307, 2004b.
- A. A. Schekochihin, A. B. Iskakov, S. C. Cowley, J. C. McWilliams, M. R. E. Proctor, and T. A. Yousef. Fluctuation dynamo and turbulent induction at low magnetic prandtl numbers. *New Journal of Physics*, 9:300, 2007.
- M. Schinner. Rotational threshold in global numerical dynamo simulations. *Mon. Not. R. Astron. Soc.*, 431:L78–L82, 2013.
- M. Schinner, L. Petitdemange, and E. Dormy. Dipole collapse and dynamo waves in global direct numerical simulations. *Astrophys. J.*, 752(2):121, 2012.
- M. Steenbeck, F. Krause, and K.-H. Rädler. A calculation of the mean electromotive force in an electrically conducting fluid in turbulent motion under the influence of coriolis forces. *Zeitschrift Naturforschung Teil A*, 21:369–376, 1966.
- A. Tilgner. A kinematic dynamo with a small scale velocity field. *Physics Letters A*, 226:75–79, 1997.

- A. Tilgner. Spectral methods for the simulation of incompressible flows in spherical shells. *Int. J. Numer. Mech. Fluids*, 30:713–724, 1999.
- A. Tilgner. Small scale kinematic dynamos: Beyond the alpha-effect. *Geophys. Astrophys. Fluid Dynamics*, 98:225–234, 2004.
- A. Tilgner. Transitions in rapidly rotating convection driven dynamos. *Phys. Rev. Lett.*, 109(24):248501, 2012.
- A. Tilgner and F. H. Busse. Saturation mechanism in a model of the karlsruhe dynamo. *Chossat P., Ambruster D., Oprea I. eds*, page 109, 2001.
- N. Weiss. Dynamos in planets, stars and galaxies. *Astrophysics & Geophysics*, 43: 3.9–3.14, 2002.
- D. S. Zimmerman. *Turbulent shear flow in a rapidly rotating spherical annulus*. PhD thesis, Faculty of the Graduate School of the University of Maryland, College Park, 2010.

# A List of Figures

2.1	Scheme of the spherical Couette system with streamlines of the axisymmetric poloidal flow (left) and a contour plot of the axisymmetric toroidal flow (right) in a meridional cut. . . . .	12
2.2	Radial dependence of the amplitude of the driving force . . . . .	17
2.3	Snapshots of the kinetic energy spectrum plotted against spherical harmonic degree $m$ (left) and isosurface of 3% of the maximum local kinetic energy (right) at $\overline{\text{Re}} = 133$ . . . . .	24
2.4	Temporally and spatially averaged spectra of $E_{kin}$ plotted against $m$ (left) and $l$ (right) at $\overline{\text{Re}} = 300$ (black) and 970 (red). . . . .	25
2.5	Snapshots of $v_r$ (top), $v_\theta$ (middle) and $v_\phi$ (bottom) in a meridional cut at $\text{Re} = 1.25 \times 10^3$ (left), $2.5 \times 10^3$ (middle) and $10^4$ (right). . . . .	26
2.6	Boundary layer thickness $d_B$ plotted against $\text{Re}^{-1/2}$ (left) and $E_{kin}$ plotted against $\text{Re}^{-1}$ . The vertical dashed lines indicates the transitions at $\text{Re}_h$ and $\text{Re}_s$ . . . . .	27
2.7	Dimensionless torque plotted against $\text{Re}$ . . . . .	27
2.8	Snapshots of the isosurface of 1% of the maximum kinetic helicity at $\overline{\text{Re}} = 132$ (left) and 970 (right). Blue indicates negative and red positive helicity. The respective maximal/minimal values are $\pm 3.5$ and $\pm 10.0$ . . . . .	29
2.9	Snapshots of the kinetic energy spectrum plotted against the spherical harmonic degree $m$ (left) and isosurface of 3% of the maximum local kinetic energy (right) at $\overline{\text{Re}} = 130$ . . . . .	30
2.10	Kinetic energy bifurcation diagram (left) and the dimensionless torque at the inner boundary (right) of the $m = 2$ and $m = 3$ instability. . . . .	30
2.11	Dynamo onset in the $(\overline{\text{Re}}, \overline{\text{Rm}})$ -plane (upper panel) and in the $(\overline{\text{Re}}, \text{Pm})$ -plane (lower panel). Failed dynamos are indicated by red dots and acting dynamos by blue asterisks. The thick dashed line marks $\overline{\text{Rm}}_c$ for $m = 2$ and the blue thick solid line for $m = 3$ . The straight lines are $\text{Pm} = 1$ (upper panel) and $\overline{\text{Rm}} = 800$ (lower panel). Vertical dashed lines mark the transitions $\text{Re}_h$ and $\text{Re}_s$ . . . . .	31

2.12	Time evolution of $v_r$ at a fixed point in the equatorial plane (left) and the torque (right) at $\overline{Re} = 114$ (red), 133 (black) and 162 (blue). The amplitudes are arbitrary since the focus is on the time dependence . . . . .	33
2.13	Kinetic energy spectra (black) and magnetic energy spectra (red) plotted against $m$ (left) and according time evolution of the magnetic energy (right) at $\overline{Re} = 133$ (top) and 162 (bottom). . . . .	33
2.14	Growth rates $s$ plotted against phase velocity $\tilde{\omega}$ for different Rm (left). The velocity fields are generated with hydrodynamic simulations at the corresponding Re. The right panel shows the time evolution of the magnetic energy in the full simulation and in the corresponding frozen flux simulation. . . . .	34
2.15	Snapshots of $B_r$ (top), $B_\theta$ (middle) and $B_\phi$ (bottom) in a meridional cut during one frozen flux simulation from one maximum (left) to the minimum (middle) to the next maximum (right). . . . .	36
2.16	Snapshots of isosurfaces of 3% of the maximum local kinetic energy (red) and 10% of the maximum local magnetic energy (blue) at $\overline{Re} = 114$ (left), 133 (right) and 162 (bottom). . . . .	37
2.17	Kinetic (black) and magnetic (red) energy spectra plotted against spherical harmonic degree $m$ at $\overline{Re} = 133$ (left) and the corresponding time evolution of the magnetic energy (right). . . . .	38
2.18	Snapshot of the isosurface of 3% of the maximum local kinetic energy (red) and 10% of the maximum local magnetic energy (blue) during a simulation with a dominant $m = 3$ instability. . . . .	38
2.19	Time evolution of the non-axisymmetric toroidal kinetic energy (left) and the magnetic energy (right) at $\overline{Re} = 210$ . . . . .	39
2.20	Spectral distribution of kinetic and magnetic energy in homogeneous isotropic turbulence at large (left) and low Pm (right) (Schekochihin et al. 2004b). . . . .	40
2.21	Temporally and spatially averaged turbulent rate of strain plotted against $m$ (left) and $l$ (right) at $\overline{Re} = 300$ (black) and 970 (red). . . . .	41
2.22	Temporally and spatially averaged Magnetic energy spectra plotted against $m$ (left) and $l$ (right) at $\overline{Re} = 300$ (black) and 970 (red). . . . .	42
2.23	Temporally and spatially averaged toroidal (red) and poloidal (black) magnetic (left) and kinetic (right) energy spectra plotted against $l$ at $\overline{Re} = 970$ . . . . .	43
2.24	Temporally and spatially averaged magnetic energy (red) and turbulent rate of strain (black) spectra at $\overline{Re} = 300$ (top left), 400 (top right), 600 (bottom left) and 970 (bottom right). . . . .	44
2.25	Snapshots of the kinetic energy spectrum plotted against $m$ (left) and isosurface of 20% of the maximum local kinetic energy at $\overline{Re} = 106$ (right). . . . .	46

2.26	Temporally and spatially averaged kinetic energy spectrum plotted against $m$ (left) and $l$ (right) at $\overline{\text{Re}} = 320$ (black) and 1100 (red). . . . .	47
2.27	Boundary layer thickness of the volume force + and the no-slip $\times$ simulations plotted against $\text{Re}^{-1/2}$ (left). Kinetic energy plotted against $\overline{\text{Re}}^{-1}$ (right). The red dashed lines represent the respective power laws of $\text{Re}^{-1/2}$ (left) and $\overline{\text{Re}}^{1/2}$ (right) . . . . .	48
2.28	Inner sphere's rotation rate $\Omega'_i$ (left) and energy dissipation $\epsilon$ plotted against $\overline{\text{Re}}$ . The red dashed lines show the respective proportionalities of $\overline{\text{Re}}^{1/6}$ and $\overline{\text{Re}}^{-1/4}$ . . . . .	48
2.29	Snapshots of the three components $r$ (top), $\theta$ (middle) and $\phi$ (bottom) of velocity field at $\text{Re} = 10^2$ (left), $4.5 \times 10^2$ (middle) and $2.5 \times 10^3$ (right). . . . .	49
2.30	Temporally and zonally averaged components of the radial (top), meridional (middle) and azimuthal (bottom) component of the velocity field with smooth (left) and rough boundaries (right). . . . .	50
2.31	Snapshots of the isosurface of 10% of the maximum kinetic helicity at $\overline{\text{Re}} = 106$ (left) and 1100 (right). Blue indicates negative helicity and red positive. The respective maximum and minimum values are ( $\pm 1.58$ ) and $(-45.57/37.17)$ . . . . .	51
2.32	Dynamo onset in the $(\overline{\text{Re}}, \overline{\text{Rm}})$ -plane (top) and in the $(\overline{\text{Re}}, \text{Pm})$ -plane (bottom). Failed dynamos are indicated red and working dynamos blue. The thick dashed line marks $\overline{\text{Rm}}_c$ and the vertical dashed lines denote the transitions $\overline{\text{Re}}_h$ and $\overline{\text{Re}}_s$ . The straight lines are $\text{Pm} = 1$ (top) and $\overline{\text{Rm}} = 600$ (bottom). . . . .	52
2.33	Snapshots of the magnetic (red) and kinetic (black) energy spectrum (left) and isosurfaces of 20% of the total kinetic energy (red) and 20% of the total magnetic energy (blue) (right) at $\overline{\text{Re}} = 106$ . . . . .	53
2.34	Temporally and spatially averaged turbulent rate of strain (black) and magnetic energy spectra (red) plotted against $l$ at $\overline{\text{Re}} = 218$ (top left), 525 (top right), 825 (bottom left) and 1100 (bottom right). . . . .	54
2.35	Toroidal (red) and poloidal (black) magnetic (left) and kinetic (right) energy spectra plotted against $l$ at $\overline{\text{Re}} = 970$ . . . . .	55
2.36	Kinematic dynamo onset with smooth and rough boundaries and the results of Guervilly and Cardin (2010). Vertical dashed lines denote the transitions $\text{Re}_h$ and $\text{Re}_s$ . . . . .	56

3.1	Left: Sketch of a convectional driven flow structure in a fast rotating spherical shell which forms a vortex columnar structure, so-called Busse-Columns (by Busse (1975)). Right: G. O. Roberts flow in a periodic box of width $a$ and height $L$ . The flow in the $x, y$ -plane is indicated by arrows and the $z$ -component by the underlying contour plot. Red denotes up and yellow down streaming flow (Roberts 1972). . . . .	62
3.2	In the left panel $E_{B,num}$ is plotted over $Rm$ together with the analytical results of the magnetic energy of first order $E_{B,1}$ (black), the total magnetic energy $E_B$ without rotation (red) and at $Ek = 1.5 \times 10^{-3}$ . In the middle figure the absolute amplitude of the rotationally dependent part of the magnetic energy $ E_B(Ek = \infty) - E_B(Ek) $ is plotted over $Ek$ . The red dashed lines indicate a proportionality to $Ek^{-2}$ . The amplitude of each fit in the middle Figure is plotted over $Rm$ on the right hand side and shows a proportionality to $Rm - Rm_c/Rm$ (red dashed). The corresponding analytical expression gives $\sim (Rm - Rm_c)^3/Rm$ (black dashed). . . . .	80
3.3	Amplitudes of the velocity field at $Rm = 0.3$ (left) and $0.7$ (right). The rotational parts of $A_R$ and $A_1$ are colored red. . . . .	84
3.4	Absolute amplitudes of the rotationally dependent part of the magnetic Energy $ E_B(Ek = \infty) - E_B(Ek) $ and the respective parts in first $ E_{B,1}(Ek = \infty) - E_{B,1}(Ek) $ and third order $ E_{B,3}(Ek = \infty) - E_{B,3}(Ek) $ at $Rm = 0.3$ (left) and $0.7$ (right). . . . .	86
3.5	Drift velocity $\omega_{ph}$ plotted over $Rm$ at $Ek = 5 \times 10^{-2}$ (left) and $Ek$ (right). .	86
3.6	In the left panel $E_{B,num}$ is plotted over $Rm$ together with the analytical results of the magnetic energy of first order $E_{B,1}$ (black), the total magnetic energy $E_B$ without rotation (red) and at $Ek = 1.5 \times 10^{-3}$ . In the middle figure the absolute amplitude of the rotationally dependent part of the magnetic energy $ E_B(Ek = \infty) - E_B(Ek) $ is plotted over $Ek$ . The red dashed lines indicate a proportionality to $Ek^{-2}$ . The amplitude of each fit in the middle Figure is plotted over $Rm$ on the right hand side and shows a proportionality to $Rm - Rm_c/Rm$ (red dashed). The corresponding analytical expression gives $\sim (Rm - Rm_c)^3/Rm$ (black dashed). . . . .	88
3.7	Drift velocity $\omega_{ph}$ plotted over $Rm$ at $Ek = 5 \times 10^{-2}$ (left) and $Ek$ (right). .	89
3.8	Amplitudes of the velocity field at $Rm = 0.3$ (left) and $0.7$ (right). The rotational parts of $A_R$ and $A_1$ are colored red. . . . .	89
3.9	Absolute amplitudes of the rotationally dependent part of the magnetic Energy $ E_B(Ek = \infty) - E_B(Ek) $ and the respective parts in first $ E_{B,1}(Ek = \infty) - E_{B,1}(Ek) $ and third order $ E_{B,3}(Ek = \infty) - E_{B,3}(Ek) $ at $Rm = 0.3$ (left) and $0.7$ (right). . . . .	89

## Scientific contributions

Finke K., Tilgner A., 2012, Simulations of the kinematic dynamo onset of spherical Couette flows with smooth and rough boundaries, *Phys. Rev. E.*, 86, 016310

## Acknowledgements

I wish to thank various people for their contribution to this project:

At first, I would like to express my gratitude to Prof. Dr. Andreas Tilgner for valuable and constructive suggestions during the development of this work. I would like to thank my second supervisor Prof. Dr. Ulrich R. Christensen for reviewing this thesis.

Moreover, I am very grateful to Ulrich Einecke for his support with respect to any computer system problems.

Furthermore, I would like to express my special thanks to Thomas Gastine, Julien Morin, A. P. Staro and Xing Wei for very helpful discussions.

I also want to thank all of the people who worked at the Institute of Geophysics for creating such a nice and supportive working environment during my time there.

At last, but certainly not least, I wish to thank everybody, who helped me to revise this work for the final version, which are: Denise Müller, Ludger Inhester, Erik Bernitt, Julia Elena Thiel, Nils Brüggemann, Nico Reinke, Thomas Linger.

# Lebenslauf

## **Persönliche Daten:**

Name: Konstantin Finke  
Anschrift: Rote Straße 16, 37073 Göttingen  
Geburtsdatum und - Ort: 30.12.1983, Delmenhorst  
Staatsangehörigkeit: Deutsch  
Familienstand: ledig

## **Schulische Ausbildung**

1990 - 1994 Grundschule in Delmenhorst  
1994 - 1997 Orientierungsstufe in Delmenhorst  
1997 - 2003 Max-Planck-Gymnasium, Delmenhorst  
Allgemeine Hochschulreife  
  
2003 - April 2004 Grundwehrdienst

## **Studium**

2004-2009 Studium der Physik an der Universität Bremen, Diplom  
Juli 2006 Diplomvorprüfung  
  
Oktober 2008 - Juli 2009 Diplomarbeit:  
Nichtlineare Dynamik starrer Körper  
  
Seit November 2009 Promotion in Physik an der  
Georg-August-Universität Göttingen  
Graduate student in der Max-Planck Solar System School